ALMA MATER STUDIORUM
UNIVERSITÀ DI BOLOGNA

DOTTORATO DI RICERCA IN

NANOSCIENZE PER LA MEDICINA E PER L'AMBIENTE

Ciclo 37

Settore Concorsuale: 02/B1 - FISICA SPERIMENTALE DELLA MATERIA

Settore Scientifico Disciplinare: FIS/03 - FISICA DELLA MATERIA

PHOTOELECTROCHEMICAL BIOMASS VALORISATION FOR RENEWABLE ENERGY CONVERSION

Presentata da: Irene Carrai

Coordinatore Dottorato
Matteo Calvaresi

Supervisore
Luca Pasquini

Co-supervisore
Raffaello Mazzaro

Esame finale anno 2025

Abstract

Natural Photosynthesis has become a guiding model for developing sustainable solutions aiding in the transition from fossil fuels to renewable energy sources. For over a century, scientists have sought to mimic plants by creating devices capable of capturing energy and storing it in chemical bonds. Among the approaches explored to date, splitting water into molecular hydrogen and oxygen offers a promising breakthrough for clean energy production. However, the slow kinetics of the oxygen evolution reaction (OER) consistently hampers the efficiency of this process, limiting its competitiveness against widely available fossil-based technologies. To overcome this limitation, the focus of the scientific community is shifting towards alternative oxidation reactions, characterised by lower energy requirements and inexpensive starting compounds. In this thesis, the conversion of biomass derivatives to useful chemicals is investigated. Given the promising theoretical solar-to-hydrogen conversion efficiency (STH) and the ability to separate between the anodic and cathodic compartments, a photoelectrochemical (PEC) cell is employed to perform the reactions. The photoanode is selected, evaluating the material's stability, performance, and sustainability along with the specific selectivity towards the desired products. The following anodic reactions were explored: i) Titanium doped hematite (Ti:Fe_2O_3) photoanodes modified with cobalt- or nickel-based co-catalysts, for the conversion of 5-hydroxymethylfurfural (HMF) into 2,5- furan dicarboxylic acid (FDCA); ii) bismuth vanadate ($BiVO_4$) photoanodes for glycerol oxidation reaction (GOR).

Ti:Fe_2O_3 photoanodes were used to oxidize the biomass derivative HMF to FDCA, a valuable building-block chemical for the synthesis of the PET-alternative, polyethylene furanoate (PEF). The oxidation process was initially conducted at pH 9, with the addition of a (2,2,6,6-Tetramethylpiperidin-1-yl) oxyl (TEMPO) mediator to accelerate the process. To improve selectivity over OER, cobalt-based co-catalysts, such as Cobalt Iron Oxide ($CoFeO_x$) and Cobalt Phosphate (CoPi), were deposited, and the photoanode modified with CoPi exhibited the highest efficiency and selectivity for FDCA production. The source of this enhancement was correlated to the co-catalyst's influence on charge carrier dynamics, which suppressed recombination processes and enabled high selectivity for TEMPO oxidation over OER.

To improve sustainability and streamline the synthesis, we aimed to eliminate the use of TEMPO by depositing nickel-based electrocatalysts onto the electrode surface. The $Ni(OH)_2$-electrodeposited (Ti:Fe_2O_3-Ni) and the NiMo-sputtered (Ti:Fe_2O_3-NiMo) Ti:Fe_2O_3 photoanodes were tested under more alkaline conditions (pH 13), achieving partial photoelectrochemical conversion of HMF to FDCA. This result highlights the positive impact of Ni-based co-catalysts in improving selectivity for the oxidation of the organic substrate, without requiring additional oxidants.

On the other hand, glycerol oxidation was studied using nanoporous $BiVO_4$ photoanodes under acidic conditions, in a flow PEC cell. This time, no co-catalysts or electron mediator were required, as glycerol proved to be an effective hole scavenger for this photoanode. Instead of prioritising PEC conversion efficiency, the study focused on assessing the long-term stability of the semiconductor through extended chronopotentiometry, performed with either constant or modulated current over time. Ultimately, current modulation led to a more stable and enhanced photocurrent response, while significantly reducing photo-corrosion.

Overall, a comprehensive understanding of the optimal conditions for both reaction and photoanode stability is crucial for maximizing process performance. This knowledge can also pave the way for successfully coupling valuable cathodic reaction, such as the hydrogen evolution reaction (HER) or CO_2 reduction, thereby greatly enhancing the overall functionality and effectiveness of the PEC device.

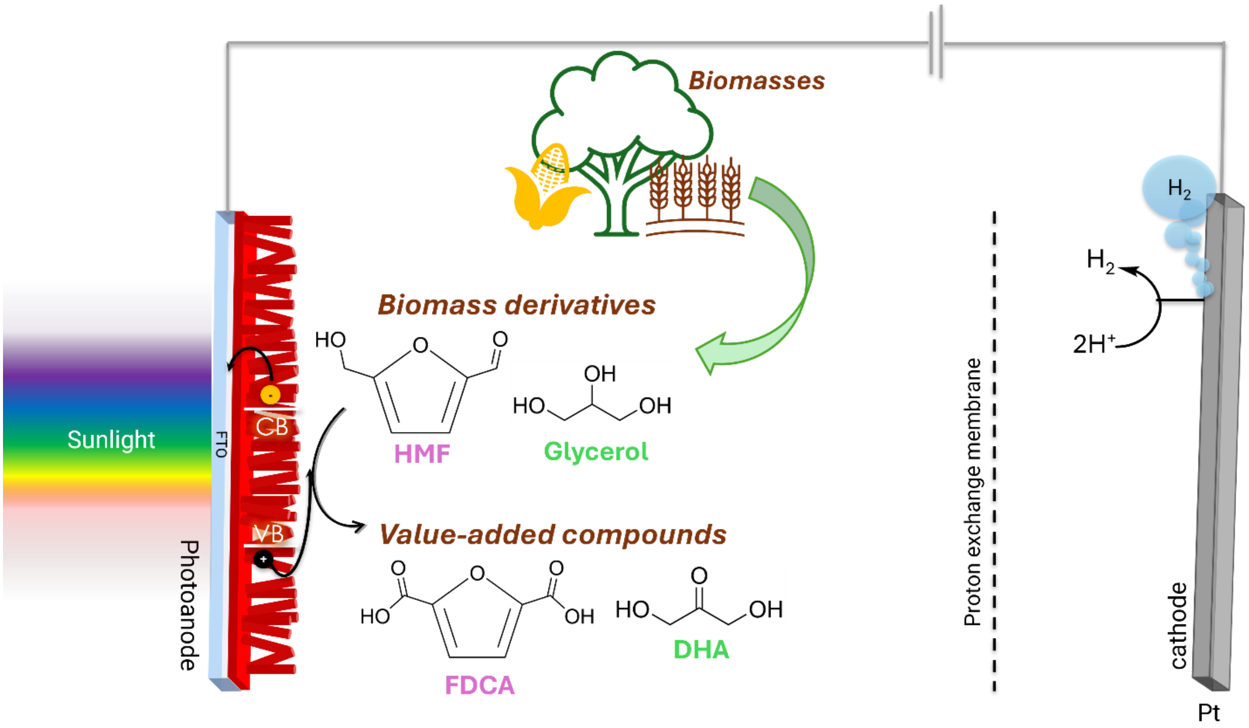

Figure 0 *Schematic representation of the PEC cell, in which the photoelectrochemical oxidation of either HMF or glycerol is performed at the anodic compartment leading to FDCA and DHA, respectively.*

Table of Contents

1. Introduction **1**

Overview of the thesis **4**

2. Semiconducting photoelectrode materials[14] **5**

2.1 Charge carrier densities under equilibrium conditions *5*

2.2 Origin of the Space Charge Layer *6*

2.3 The Semiconductor-Liquid Junction *6*

2.4 Charge carrier densities under quasi-equilibrium conditions *9*

2.5 Semiconducting materials for biomass valorisation within a PEC cell *12*
  2.5.1 Metal Oxides Semiconductors (MOS) 12

3. From raw materials: Biomass as an alternative carbon source **15**

4. Biomass valorisation to building block chemicals: HMF, "the sleeping giant" **17**

4.1 HMF oxidation to FDCA *18*

4.2 HMF photoelectrochemical conversion to FDCA *19*

5. Biomass valorisation to building block chemicals: the "sweet taste" of glycerol [138] **22**

5.1 Glycerol from biodiesel synthesis *22*

6. Characterization techniques **24**

6.1 PEC measurements *24*

6.2 Electrochemical Impedance Spectroscopy (EIS)[120] *26*

6.3 Intensity Modulated Photocurrent Spectroscopy (IMPS) *29*
  6.3.1 The rate constant model in IMPS 31
  6.3.2 Lasso-Distribution of Relaxation Times (L-DRT) for IMPS data fitting[127] 33

6.4 X-ray Absorption Spectroscopy (XAS) *35*
  6.4.1 Operando X-ray Absorption Spectroscopy 36

6.5 X-ray Photoelectron Spectroscopy (XPS) *38*

6.6 Spectro-photometry *41*

6.7 Spectro-fluorimetry[133] *42*

6.8 High-Performance Liquid Chromatography (HPLC) *44*

7. Preparation of photoanodic materials for solar energy conversion **46**

7.1 $BiVO_4$ photoanodes *46*

7.2 Ti:Fe_2O_3 photoanodes *46*
  7.2.1. Co-catalysts modification 50

8. TEMPO-mediated HMF photoelectrochemical oxidation to FDCA with Ti:Fe_2O_3 photoanodes modified with Co-based co-catalysts **53**

8.1 PEC-OER characteristics of co-catalyst-modified Ti:Fe_2O_3 photoanodes *53*

8.2 TEMPO-mediated photoelectrochemical HMF conversion *55*

8.3 Optimization of FDCA production *58*

8.4 Mechanistic description of charge transfer kinetics *60*

9. Direct HMF photoelectrochemical oxidation to FDCA with Ti:Fe_2O_3 photoanodes modified with Ni-based co-catalysts **67**

9.1 PEC characterization *69*

9.2 HMF PEC conversion *71*

9.3 X-ray spectro-electrochemical analysis *76*

9.4 Spectro-photometric characterization during HMF PEC conversion *80*
9.4.1 Stability tests 81
9.4.2 Fitting equation 82

10. Boosting stability of nanoporous $BiVO_4$ photoanodes for PEC glycerol oxidation through current modulation **84**

10.1 Oxygen Evolution Reaction (OER) *85*

10.2 Glycerol Oxidation Reaction (GOR) *87*

Conclusions **93**

Bibliography **94**

Acknowledgements **102**

1. Introduction

Since the XX century, many scientists started to investigate Natural Photosynthesis, trying to reproduce the way in which plants harvest the energy from the Sun and store it in the form of chemical bonds[1]. The conversion of sunlight into energy vectors is considered one of the few sustainable solutions to the worldwide climate crisis, helping in the transition from fossil fuels to renewable energy sources. Among all the methods investigated so far, the solar splitting of water into molecular hydrogen, H_2, and oxygen, O_2, stands out as particularly promising[2]. By harnessing solar energy, it is possible to convert a very cheap starting compound, H_2O, into H_2, a carbon-free energy carrier. Hydrogen can be stored and used as a source of energy, or it can be converted into carbon-based fuels, such as methanol, dimethyl ether[3]. Those processes provide large amounts of energy without generating CO_2 emissions and thus making hydrogen a globally trusted solution to address climate challenges.

Nowadays, solar water splitting can be performed according to three different configurations. i) The photocatalytic (PC) water splitting, where the semiconductor, suspended in an aqueous solution, absorbs sunlight, and drives both the oxidative and the reductive semi-reactions, producing H_2 and O_2 at the same time (Figure. 1a)[4–6]. This approach is usually characterized by a low solar-to-hydrogen (STH) conversion efficiency, due to the limited absorption capability of the semiconductor (for TiO_2 or $SrTiO_3$ is usually lower than 400 nm) and the challenges in separating the products from the reaction mixture. ii) The photovoltaic assisted electrolysis (PV-E) is instead composed of a photovoltaic cell that converts sunlight into electrical energy, which is then used by the electrolyser to perform water electrolysis (Figure. 1b)[7]. This is, so far, the way in which water splitting is performed in the large scale: the highest values of the STH efficiency can be reached, and an easy implementation is required for the process scale-up. However, the huge costs of the components make the carbon-based hydrogen production methods still more competitive for industrial applications. iii) photoelectrochemical (PEC) water splitting is another promising approach that can lead to high theoretical STH efficiency. The device requires a simple fabrication, and the two half-reactions takes place in separate compartments, preventing the formation of the explosive H_2/O_2 mixture, unlike in PC and PV-E devices (Figure. 1c)[8–11]. In this setup, selecting the appropriate semiconducting material is crucial to maximize the efficiency. The photoelectrodes must absorb across a wide region of the solar spectrum and possess good charge separation and transport properties, to efficiently catalyse the two redox semi-reactions. Over the years, single junctions' materials as well as more complex nanostructured heterojunctions have been explored and, to improve their performance, co-catalysts modifications have also been implemented. However, unassisted PEC solar water splitting is difficult to achieve and, even with the addition of an external electrical supply, the experimentally obtained STH efficiency remains low. Thus, this technology is still not competitive with the fossil-based methods widely available on the market, nor with PV-E, which remains the most favourable option for commercial solar water splitting[12]. Nevertheless, the development of tandem PEC devices offers the potential for significant advancements in this technology[13]. By combing two semiconductors that absorb complementary regions of the solar spectrum, both light-harvesting efficiency and H_2/O_2 production can be maximized, without the need of an external energy supply[8,9].

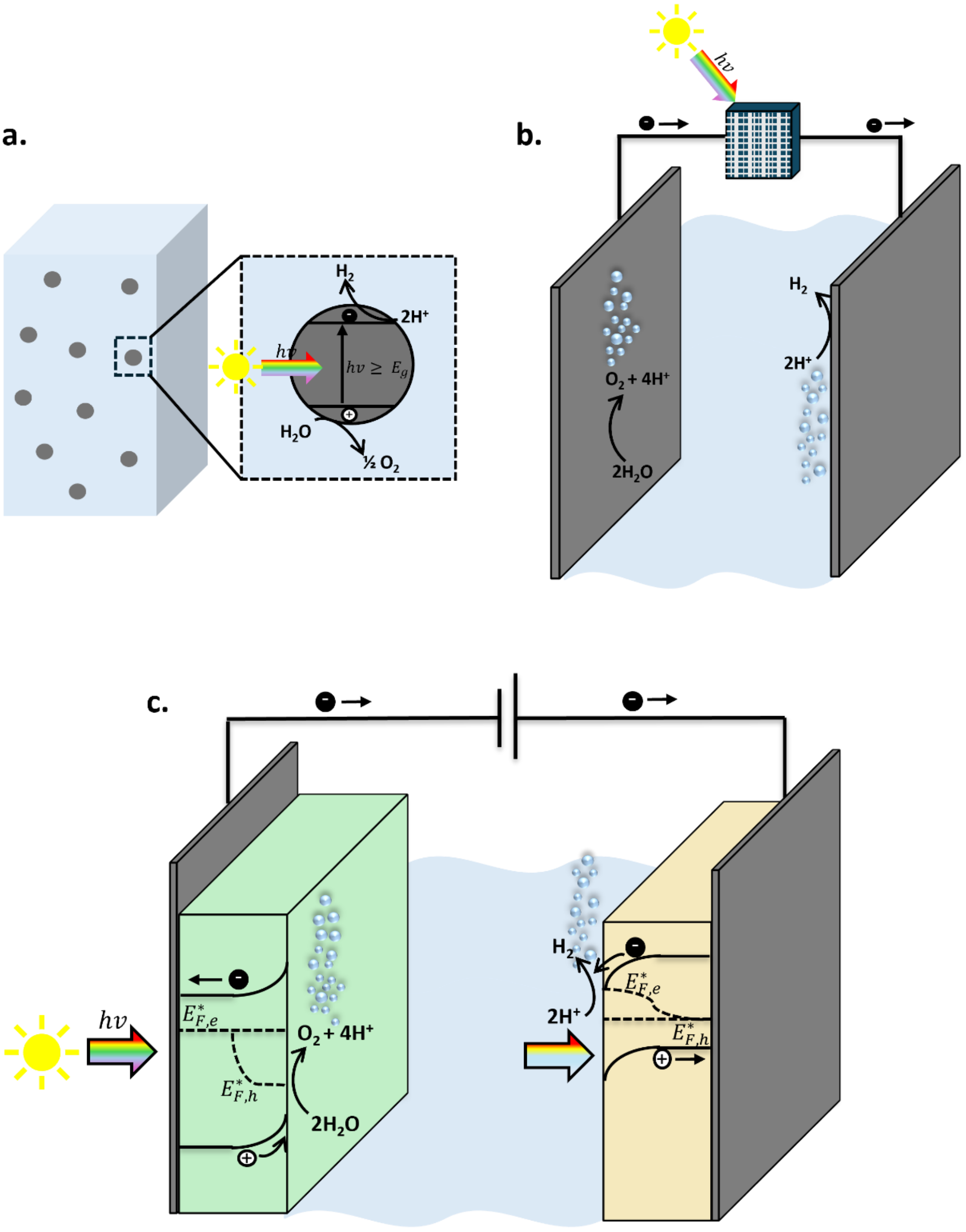

Figure 1 *Schematic of the three possible configurations for solar water splitting:* ***(a)*** *photo catalysis (PC),* ***(b)*** *photovoltaic-assisted electrolysis (PV-E) and* ***(c)*** *Photoelectrochemical (PEC) water splitting.*

A common drawback that unifies the above-mentioned configurations is the oxygen evolution reaction (OER) performed at the anode. Differently than the cathodic Hydrogen Evolution Reaction (HER), OER has a very slow kinetic, involving multiple proton-coupled electron transfer steps which make it complex and challenging to optimize.

In acidic media, the water splitting reaction can be written as follows:

$$4H^+ + 4e^- \leftrightarrows 2H_2 \quad E^0_{red} = +\,0.000\,V\ vs\ NHE \qquad (1.1)$$

$$2H_2O \leftrightarrows O_2 +\ 4H^+ + 4e^- \quad E^0_{ox} = -1.229\,V\ vs\ NHE \qquad (1.2)$$

Whereas, in alkaline media is:

$$4H_2O + 4e^- \leftrightarrows 2H_2 + 4OH^- \quad E^0_{red} = -0.828\,V\ vs\ NHE \qquad (1.3)$$

$$4OH^- \leftrightarrows O_2 + 4e^- + 2H_2O \quad E^0_{ox} = -0.401\,V\ vs\ NHE \qquad (1.4)$$

The Gibbs free energy change ΔG for the overall water splitting reaction is given by:

$$\Delta G = -nF\Delta E \ (1.5)$$

At standard temperatures (298 K) and concentrations (1mol/L, 1 bar), the electrochemical cell voltage ΔE of -1.229V vs NHE corresponds to a ΔG change of +273 $kJ \cdot mol^{-1}$, showing a thermodynamically uphill reaction[14]. The thermodynamic activation energy combined with the substantial overpotentials from sluggish kinetics raise the overall energy requirement, making the reaction more challenging to drive. In addition, the low economic value of the final product, O_2, further decreases the appealing of whole process.

For these reasons, the oxidation of more valuable compounds started to be investigated[15–18]. To replace the cheap and environmentally benign OER, the new anodic reaction must involve abundant, low cost and non-toxic feedstocks and the oxidized product must have an added value compared to the starting materials. Up to now, two possible routes have been investigated: i) the up cycling of plastic waste, such as polyester microfibers or polyethylene terephthalate (PET) to commodity chemicals, like acetate, terephthalic acid and formate[19–22] or ii) the oxidation of biomass derivatives, e.g. glycerol or furfural, to value-added compounds, such as dihydroxyacetone (DHA), glyceric acid (GLA) or 2,5- furan dicarboxylic acid (FDCA)[23–28] All the above-mentioned reactions typically require lower activation energies than OER, occurring at less anodic potential. However, as many intermediates can be generated from the same starting compound, a deep understanding of the underlying reaction mechanism is necessary. This knowledge can also help in both selecting and fine-tuning the material for the desired reaction pathways and outcomes.

Overview of the thesis

In this thesis, the photoelectrochemical oxidation of biomass-derivatives such as glycerol and 5-hydroxymethil furfural (HMF), was performed at the anodic compartment of a PEC cell. The photoanodic material was a Metal Oxide Semiconductor (MOS), chosen considering its photoelectrochemical and photophysical properties as well as the experimental conditions required to perform the reaction. When needed, the photoanode's surface was modified with co-catalysts and an electron mediator was introduced in the electrolyte. A comprehensive evaluation of the products and by-products formation was performed by means of spectrophotometric, fluorometric and HPLC analysis. To achieve more insights into the oxidation mechanism, several techniques were applied such as Intensity Modulated Photocurrent Spectroscopy (IMPS), Electrochemical Impedance Spectroscopy (EIS) and operando X-ray Absorption electrochemical Spectroscopy (XAS).

Before delving into the core experimental results and discussion, a thorough overview of the key tools required to understand the processes within a PEC cell is presented. The significance of these anodic reactions is highlighted, emphasizing their long-term impact. The investigation begins with the synthetic routes of starting compounds such as glycerol and HMF, examining both raw materials and their processing. Established and cutting-edge technologies for glycerol and HMF oxidation are then explored, showcasing recent advances in the PEC field. The selection of the semiconductor is justified, considering its photophysical and photoelectrochemical properties, structure, and morphology.

2. Semiconducting photoelectrode materials[14]

To fully grasp the specifics of these valuable anodic reactions, it is first essential to understand the underlying processes within a PEC cell. This involves examining the mechanisms at play when a semiconductor is put in contact with an electrolyte solution and the effects of applying an external bias and illumination. Modelling the system can also help in understanding the thermodynamic and kinetic criteria that guide the selection of photoelectrodes for targeted anodic or cathodic reactions.

2.1 Charge carrier densities under equilibrium conditions

The degree of doping of a semiconductor allows for the distinction between intrinsic (no donors) n-type (high number of electron donors), and p-type (high number of electron acceptors) semiconductors. Under equilibrium conditions, i.e. no illumination and no net current flow, the position of the Fermi level (E_F) with respect to the conduction band minimum (E_C) and valance band maximum (E_V) is depicted as follows:

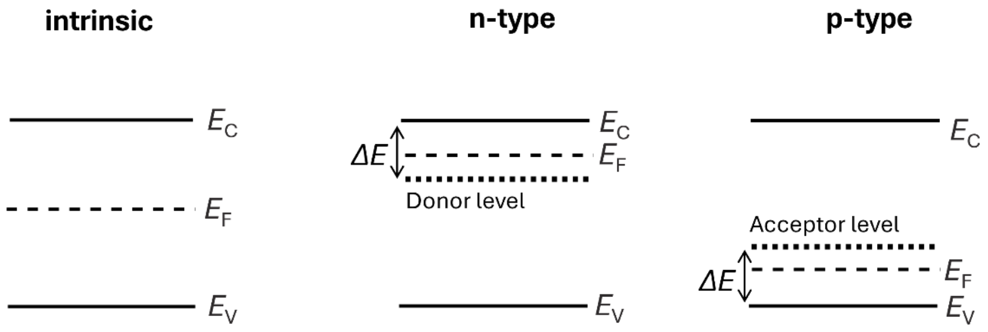

***Figure 2.1** Positions of the conduction band minimum (E_C), valence band maximum (E_V) and Fermi level (E_F) for intrinsic, n-type and p-type semiconductors. Depending on the energy shift (ΔE) with respect to E_C or E_V, the corresponding donor and acceptor levels will be defined as shallow ($\Delta E \sim 3k_BT$) or deep ($\Delta E < 3k_BT$) energy levels.*

The Fermi level (E_F) can thus be defined as the chemical potential of the semiconductor's major carrier, i.e. electrons for n-type and holes for p-type semiconductors. Knowing the value of E_F, the concentration of free electrons (n_0) and holes (p_0) at the equilibrium can be determined, according to:

$$n_0 = N_C \, exp\left(\frac{E_F - E_C}{kT}\right) \quad N_C = 2 \cdot \sqrt[3]{\frac{2\pi m_e^* kT}{h^2}} \quad (2.1)$$

$$p_0 = N_V \, exp\left(\frac{E_V - E_F}{kT}\right) \quad N_V = 2 \cdot \sqrt[3]{\frac{2\pi m_h^* kT}{h^2}} \quad (2.2)$$

where N_C and N_V are the effective density of states of electrons in the conduction band (CB) and holes in the valence band (VB), respectively.

Doping in semiconductors involves integrating foreign anions and cations with suitable ionic charge and radii into the material's lattice stoichiometry. This process is commonly employed to enhance material conductivity, which is given by: $\sigma = ne\mu_e + pe\mu_h$. Indeed, by increasing the concentration of electrons, n, or holes, p, it is possible to compensate for the low electron mobility, μ_e, or hole mobility μ_h, respectively. In metal oxides semiconductors (MOS), shallow donors and acceptors are typically introduced to address the low intrinsic mobility of their charge carrier. Other properties can be improved with doping such as optical absorption, especially in wide band gap semiconductors, diffusion length of minority carriers, and catalytic activity at the surface.

Intrinsic defects, i.e. vacancies, interstitial and substituents, can also influence semiconductor's performance, producing similar effects to those of external dopants. These defects may arise from internal defect-chemical reactions or changes in lattice stoichiometry, such as oxygen exchange with the gas phase. Understanding the interplay between dopants and defect concentrations is crucial for the effective design of photoelectrode materials.

2.2 Origin of the Space Charge Layer

The Space Charge Layer (SCL), or built-in electric field, is a distinctive feature of semiconducting materials. Its formation is traditionally explained by considering a semiconductor put into contact with a metal or another semiconductor[29]. If the two materials have different Fermi levels, charge is transferred from one side to the other until an equilibrium is reached. The potential distribution and width of the SCL, also known as depletion layer, are determined by the amount of charge transferred to the surface and the density of shallow donors in the material. The total charge in the depletion layer is balanced by a sheet of opposite charges, mainly due to the ions present in the electrolytic solution approaching the material's surface. In metals, SCL is extremely thin (~1 Å) and quickly neutralized due to the high density of free charge carriers. Instead, in semiconductors the space charge plays a much more significant role greatly influencing their behaviour and interactions with gases, liquids, and other conductive or semiconductive materials. A typical value of semiconductors' space charge capacitance (C_{SC}) goes from 10 to 1000 nF/cm^2.

2.3 The Semiconductor-Liquid Junction

When a semiconductor is immersed in an aqueous solution, hydroxide and proton ions continuously absorb and desorb from the surface and a dynamic equilibrium is established:

$$M - OH \overset{k_a}{\leftrightarrow} MO^- + H^+_{aq} \ (2.3)$$

$$M - OH + H^+_{aq} \overset{k_b}{\leftrightarrow} M - OH_2^+ \ (2.4)$$

The shifting of this equilibrium will depend on the pH of the solution and on the specific Brønsted acidity of the surface. Reactions (2.3) and (2.4) are valid only for amphoteric surfaces, such as hydroxylated semiconductor surfaces, which is typical of MOS photoelectrodes.

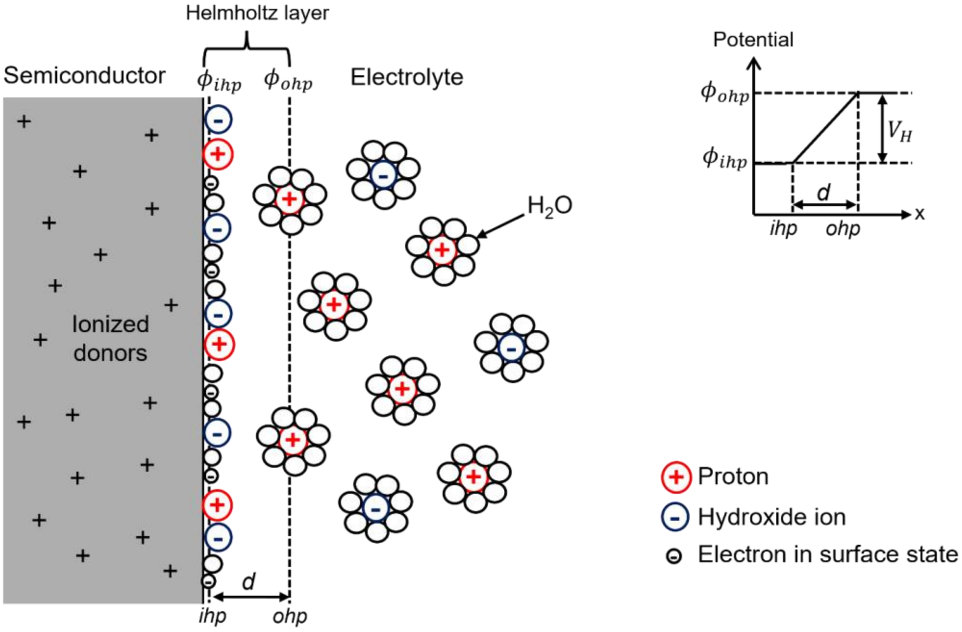

Figure 2.2 *Schematic representation of the semiconductor/electrolyte interface and the Helmholtz layer. The inner Helmholtz plane (ihp) is composed of* H^+ *and* OH^- *specifically absorbed onto the semiconductor's surface, while the outer Helmholtz plane (ohp) defines the closest distance the ions from solution can approach. The distance d is only few Ångstroms because of the solvation sphere of water molecules surrounding each ion. Image adapted from reference* [30] *of Van de Krol et al.*

Figure 2.2 schematizes all the charges present at the semiconductor/electrolyte interface. Electrons and holes are trapped in surface states, and specifically absorbed ions from solution are also identified. To counterbalance, ionized donors or acceptors from the solid as well as oppositely charged ions from solution approach the interface. Because of the large dipole moment of water, each ion in the electrolyte is surrounded by a solvation sphere of water molecules, which prevents them for approaching the interface closer than few angstroms. This defines the Helmholtz layer, i.e., the region between the specifically absorbed ions (inner Helmholtz plane, *ihp*) and the nearest ions in solution (outer Helmholtz plane, *ohp*). The potential drop across this layer is highly dependent on the kinetic of interfacial electron transfer and is given by:

$$V_H = \frac{Q_S \cdot d}{\varepsilon_r \varepsilon_0} \quad (2.5)$$

where d is the effective thickness of the Helmholtz layer, Q_S is the surface charge density of the electrode and $\varepsilon_r \varepsilon_0$ are the dielectric constants of the interfacial solvent and vacuum, respectively. With this understanding, we can now define the band diagram of a complete PEC cell under equilibrium conditions (Figure 2.3). The y axis represents the energy of an electron at point x, where the energy of an electron in vacuum at infinite distance (E_{vacuum}) is put as the reference. E_{vacuum} bends within the space charge region of the semiconductor, in response to the electric field. When it goes through the electrolyte it returns to be flat, since no electric field is assumed to be present, as the electrolyte is sufficiently concentrated to avoid Ohmic losses. The term $e\phi_R^*$ defines the energy of a redox couple in the electrolyte with respect to the vacuum level, whose precise determination is not so trivial. The values of electron affinity (X) and ionization energies (IE) are intrinsic to the material, whereas the semiconductor's work function (ϕ_s) varies with the distance from the surface. As previously mentioned, on the cathodic side, the high concentration of free electrons leads to a very thin and negligible SCL at the metal counter electrode. In contrast, the Helmholtz layer at the metal/electrolyte interface exhibits a structure similar to that of semiconductors, with a comparable capacitance (C_H) in the range of $10 - 20\ \mu F/cm^2$.

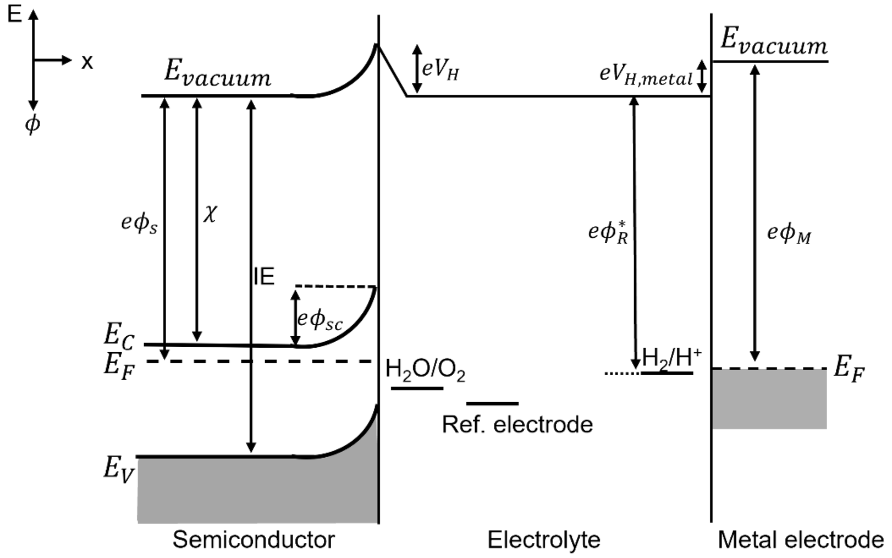

Figure 2.3 *Energy diagram of a PEC cell composed of an n-type semiconductor as the working electrode and a metal as the counter electrode. Image adapted from reference* [30] *of Van de Krol et al.*

The band energy diagram of a PEC cell allows to predict whether certain oxidation and reduction reactions are thermodynamically possible. It also summarizes some key parameters of the semiconducting material such as the band edge positions, the amount of band bending and the difference between E_F and E_C, which can also be calculated using *Equation 2.1* for the free electron's concentration in the bulk (n_0).

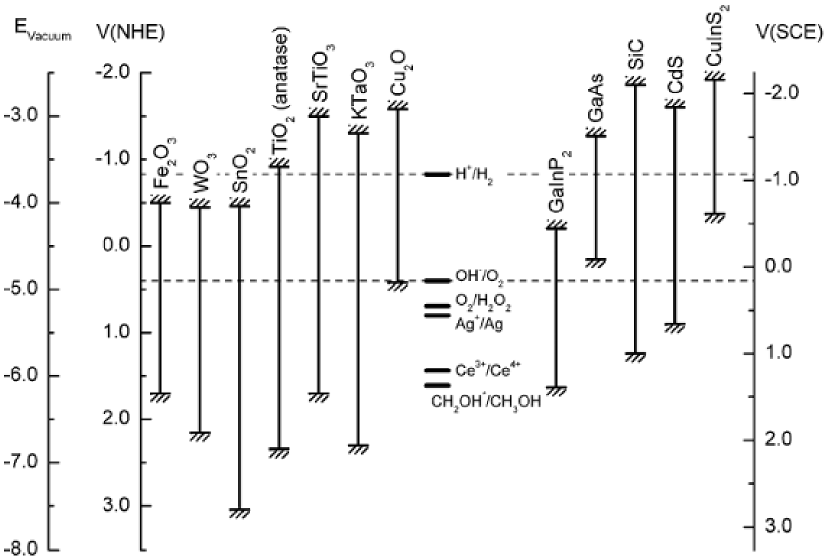

Figure 2.4 *Band edge positions for selected semiconductors at pH 14 together with some important redox potentials. Image adapted from reference* [30] *of Van de Krol et al.*

However, the actual reduction power of electrons in n-type semiconductors, is often lower than the semiconductor's CB band edge. The same applies for the oxidation power of holes in p-type semiconductors. This is due to energy losses occurring while travelling the SCL and/or when leaving the semiconductor's major carrier band to reach the Fermi level of the metal counter electrode.

2.4 Charge carrier densities under quasi-equilibrium conditions

When an external bias is applied between the working and the reference electrode, the potential is distributed across the Helmholtz and the Space Charge layer of the semiconductor. These components act as two capacitances in series:

$$\frac{1}{C_{tot}} = \frac{1}{C_{SC}} + \frac{1}{C_H} \quad (2.6)$$

Both layers have the same charge (C) accumulated within the *ihp* and, since $C = Q/V$, the potential distribution is expressed by:

$$\frac{\Delta V_{SC}}{\Delta V_H} = \frac{C_H}{C_{SC}} \quad (2.7)$$

Given that $C_H \gg C_{SC}$ (see above), changes in the applied bias primarily affect the SCL of the semiconductor rather than V_H. When a positive bias is applied to an n-type semiconductor, the band bending deepens. If the bias is sufficiently negative, the band bending can be reduced to 0, a situation referred to as the "flatband potential" (ϕ_{FB}). The position of the band edges of a semiconductor with respect to the redox potentials of electrolytic species is commonly reported using the corresponding flatband values. Ideally, applying a potential equal to ϕ_{FB}, should initiate the oxidation of the electrolyte species, signalled by a photocurrent onset. However, experimentally, the required potential is often more positive than ϕ_{FB}. Indeed, although the reaction is thermodynamically feasible, the electron transfer is often affected by kinetic constraints and is more accurately described as a quantum-mechanical tunnelling process. Gerischer first explained this phenomenon in the 1960s[31] through an electrochemical interpretation of Marcus theory[32,33], which later earned the Nobel Prize in Chemistry in 1992. The basic concept behind this theory is to consider fluctuating energy levels in the electrolyte and their probability distribution, which defines the likelihood of a reduced or oxidized species attaining a certain energy. Consequently, interfacial electron transfer occurs only when the fluctuating energy level of this redox species matches that of the electron or hole in the semiconductor. The kinetic of this process depends on the carrier concentration in the semiconductor, the density of states of the electrolyte species, and a quantum-mechanical tunnelling coefficient. The transfer can be kinetically hindered by some limitations including charge carrier recombination in the space charge layer, hole trapping at surface defects, and holes accumulation at the interface.

Under operating conditions, the PEC cell is subjected to both an applied bias and illumination (Figure 2.5). By shining light, electron-hole pairs are generated, increasing the Fermi level and reducing band bending, similarly as applying an external bias. As a result, more holes (or electrons) accumulate at the interface, and once band alignment is achieved, these carriers can be transferred. In this non-equilibrium state, a single Fermi level is no longer sufficient to describe the system. If the system is close to equilibrium, known as quasi-equilibrium, two distinct chemical potentials can be defined: the quasi-Fermi level of the electrons ($E^*_{F,e}$) and the quasi-Fermi level of the holes ($E^*_{F,h}$).

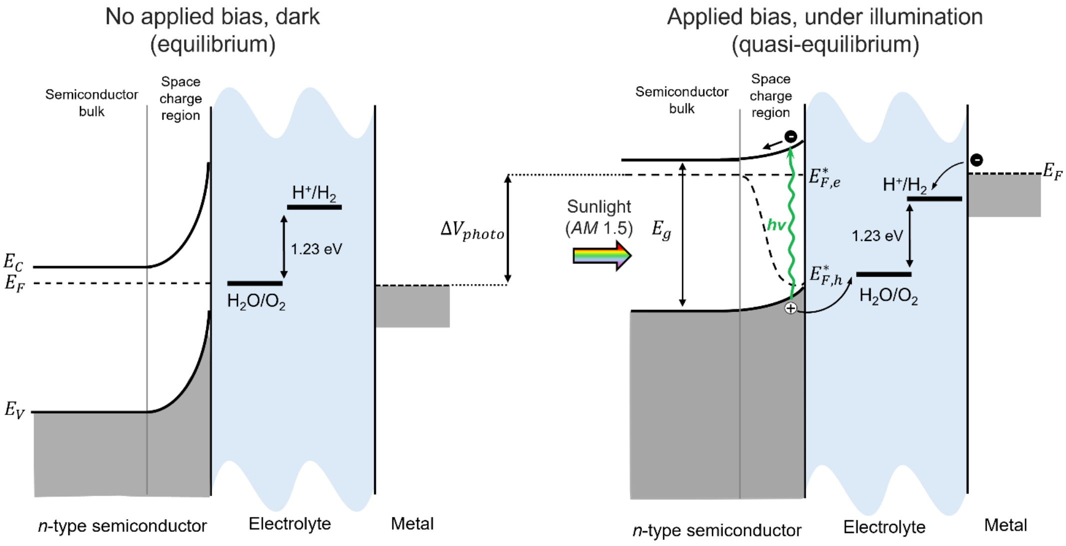

Figure 2.5 *Band diagram of a PEC cell featuring an n-type semiconducting photoanode electrically connected to a metal counter electrode. On the left side, the system is shown under equilibrium conditions, with no applied bias and illumination. The thermodynamic energy required to drive water splitting is indicated. On the right side, the system is exposed to both applied bias and illumination. The photovoltage, represented as* ΔV_{photo}*, is also illustrated.*

Similarly to E_F under equilibrium condition, also $E^*_{F,e}$ and $E^*_{F,h}$values can be employed to directly measure the number of electrons and holes in quasi-equilibrium conditions, n and p respectively, according to:

$$n = n_0 + \Delta n = \ N_C\ exp\left(\frac{E^*_{F,e} - E_C}{kT}\right) \quad (2.8)$$

$$p = p_0 + \Delta p = \ N_V\ exp\left(\frac{E_V - E^*_{F,h}}{kT}\right) \quad (2.9)$$

With a n-type semiconductor the electrons are the majority carriers, and we can approximate n ∼ n_0. So, $E^*_{F,e}$ equalizes the equilibrium Fermi level, i.e. $E^*_{F,e} \sim E_F$. This does not apply for the holes, i.e. the minority carrier, whose quasi-Fermi level ($E^*_{F,h}$) start separating from the bulk Fermi level in the SCL of the material. For p-type semiconductors, will be the vice versa.

Both for p-type and n-type semiconductors, the difference between $E^*_{F,e}$ and $E^*_{F,h}$, i.e. the quasi-Fermi level splitting (QFLS), defines the photovoltage (ΔV_{photo}).Unlike equilibrium condition, where the built-in electric field within the space charge region sweeps opposite charges to opposite regions of the semiconductor, under quasi-equilibrium conditions, the photovoltage is the driving force responsible for this charge movement. Hence, in n-type semiconductors, the gradient generated by $E^*_{F,h}$ will drive the diffusion of electrons and holes across the material.

The photovoltage can be measured by the voltage difference between dark and illuminated conditions at open circuit (ΔOCP). Ideally, this value should match the semiconductor's band gap. However, surface imperfections often disrupt band alignment, reducing photovoltage and causing *Fermi level pinning*. This pinning can also occur in the dark when the electrode is dominated by densely populated surface states. In such cases, the Fermi level stabilizes between these energy levels, and any applied potential leads to charge redistribution within these states, causing minimal shifts in the Fermi level and resulting in pinning. The nature of these surface states varies with the type of semiconductor. In covalent semiconductors, *Schockley states* arise from surface dandling bonds and act as electron donors or acceptors. In ionic semiconductors, *Tamn states* form due to the coordination of unsaturated surface ions or the adsorption of ions from the solution, influencing surface behaviour. Additionally, in transition-metal oxide semiconductors, which feature localized electronic states, mid-gap polarons can form upon illumination.

The formation of these states leads to deviations between the optical band gap and the effective electronic band gap, impacting charge transfer reactions. Understanding these effects is crucial for improving the design and efficiency of PEC devices.

It is important to underline that the above description of the PEC system under quasi-equilibrium conditions was based on the Gartner model. This model assumes that recombination occurs only outside the depletion layer, while charge separation takes place exclusively within the space charge layer. This approximation is valid when the charge diffusion length in the bulk of the material is relatively short.

2.5 Semiconducting materials for biomass valorisation within a PEC cell

A good semiconductor must not only efficiently absorb visible light but also have band edge positions suitably aligned to favour the desired oxidation reaction. In this way, high photocurrent values can be reached at low potentials, while avoiding competing oxidative pathways. To this aim, an optimal charge transfer must be provided while minimising recombination, both in the bulk and at the interface. Other critical factors to consider are the working conditions, such as the electrolyte and pH, and the material's resistance to photo-corrosion, to ensure an optimal performance and lifetime. Ideally, a semiconductor material must balance the need for a high band gap to achieve a high photovoltage, and a low band gap to generate a high photocurrent. To meet these conflicting requirements, tandem PEC devices or multijunction systems are often employed enabling the attainment of both high photovoltage and photocurrent. Additionally, kinetic limitations can be addressed by customizing the work function of the semiconductor—such as by altering the metal in MOS or modifying the redox probe in the electrolyte. Another effective strategy is the deposition of co-catalysts on the electrode surface. Techniques like electrodeposition or magnetron sputtering can be used to deposit various co-catalysts, such as cobalt-based or nickel-based oxides, providing a specific interface selectivity toward the targeted oxidizing (or reducing) species.

Every time a reaction is performed at the interface, the photovoltage of the semiconductor should match the operating voltage of the PEC device, E_{OP}, which is given by:

$$E_{OP} = E_{rev} + \eta_{ox} + \eta_{red} + \eta_{\Omega} + \eta_{other} \quad (2.10)$$

where E_{rev} is the reversible thermodynamic potential for a specific reaction (e.g. $1.23\ V\ vs\ RHE$ for water splitting), η_{ox} and η_{red} are the overpotentials (kinetic limitations) for the anodic and cathodic reaction, respectively. Additionally, η_{Ω} must be considered which is the ohmic overpotential due to the electrolyte resistance (R_{sol}) as well as other sources of overpotentials (η_{other}) such as surface states limiting the photovoltage, reaction overpotential (e.g. if the chemical reaction is too slow compared to electron transfer), diffusion overpotential (e.g. convection, migration, mass transport), ohmic losses (wires, contact, bubbles).

2.5.1 Metal Oxides Semiconductors (MOS)

Being extensively studied to perform OER, MOS are showing promising results as photoanodes for alternative oxidation reactions. These materials have a good stability, cost effectiveness and light-harvesting properties in the visible spectral range[34,35]. Unlike conventional semiconductors, characterized by covalent bonding between identical atoms, such as silicon and germanium, MOS exhibit highly polar or ionic chemical bonds, due to significantly higher electronegativity of oxygen compared to metals. By analysing the electronic structure of these material, using specialized software, researchers can gain crucial insights into the nature of optical transition (direct versus indirect), charge carrier mobility and the density of states (DOS), which indicate the number of allowed electronic states per unit of energy interval. Extensive research on MOS for PEC water splitting has provided valuable information on the structural, morphological and photoelectrochemical properties of these materials, aiding in the exploration of novel anodic reactions. In this thesis, we will focus on two of the most widely used MOS as photoanodic materials to perform organic oxidation reactions within a PEC cell.

2.5.1.1 Bismuth vanadate photoanodes ($BiVO_4$)

Among all the semiconductors investigated so far, n-type bismuth vanadate ($BiVO_4$) is considered one of the best candidates to perform oxidative reactions in a PEC cell[36–38]. This photoanode boasts several advantages, including a conduction band (CB) edge close to the thermodynamic hydrogen evolution potential[39], non-toxicity, low cost, and good chemical stability[40]. Additionally, $BiVO_4$'s relatively narrow band gap of 2.4 eV to 2.6 eV and good absorption properties[41–43], make it suitable for combining with other semiconducting materials forming n-n heterojunctions, like $BiVO_4/WO_3$[44–50], or tandem PEC devices[51].

However, its poor electronic properties and surface catalytic activities, often lead to bulk and interfacial recombination phenomena, reducing its performance. To avoid that, high-surface area nanoporous $BiVO_4$ electrodes were developed by Choi et al.[52], efficiently suppressing bulk carrier recombination and thereby improving electron-hole separation efficiency. Crystal facet engineering was also employed by others[53–56], as different facets of $BiVO_4$ exhibit varying charge separation and transfer capabilities. A recent approach, the so-called vacancy defects engineering, optimizes the number of vacancy defects within the semiconductor's electronic structure to improve conductivity, mobility and the overall photocatalytic activity[57,58]. In this thesis, nanoporous $BiVO_4$ photoanodes were synthesized following the procedure of Choi et al.[52]. More details about the synthetic procedure are available in *Chapter 7, Section 7.1*.

In addition to kinetic limitations, $BiVO_4$ photoanode is highly susceptible to both chemical and photochemical corrosion, significantly undermining its competitiveness with other semiconductors and its long-term reliability. Toma et al.[59] showed that chemical degradation occurs uniformly at the solid/liquid interfaces, leading to the gradual dissolution of $BiVO_4$ thin films over time. This process can be severely accelerated by factors such as illumination, elevated pH levels, and the application of anodic bias. Upon photoexcitation, the accumulation of holes at the semiconductor surface destabilizes the lattice, further intensifying the dissolution process. The application of protective surface layers, such as co-catalysts, is a common strategy to mitigate corrosion while also enhancing kinetic stability, therefore improving the material's long-term durability[60–66]. In addition to that, bismuth is a critical raw material due to the limited availability in the Earth's crust and the high supply risk indicator. So, despite the promising results achieved as photoanode in a PEC cell, these limitations restrict the applicability of $BiVO_4$, prompting the exploration of alternative metal oxides.

2.5.1.2 Titanium doped hematite photoanodes (Ti: Fe_2O_3)

Hematite (α-Fe_2O_3) is an inexpensive and non-toxic semiconductor made from earth-abundant elements. It has a broad light-harvesting spectrum (of about 2.1 eV) and exhibits excellent stability in basic solutions, with virtually no risk of photo-corrosion[67]. Although these characteristics would make it a suitable alternative to $BiVO_4$ when working in basic environments, poor hole diffusion and charge injection properties characterise this photoanode, significantly reducing the faradic efficiency for the desired anodic reaction. To mitigate such unfavourable properties, doping and surface heterostructuring are commonly employed: the first improves hole transfer at the interface, while the latter enhances charge injection capabilities through the synthesis of porous or nanorod hematite photoanodes[68].

In this work, titanium-doped hematite photoanodes were utilized to drive oxidative reactions in the anodic compartment of a PEC cell. Further information on the synthesis is provided in *Chapter 7, Section 7.2*. According to previous work[69], the incorporation of Ti(IV) into the hematite matrix results in the formation of ilmenite ($FeTiO_3$) near-surface layers, which markedly enhance PEC performance. Ilmenite phase effectively passivates deep surface traps, which normally act as recombination centres and cause Fermi-level pinning in unmodified hematite. Additionally, it increases the concentration of oxygen vacancies, which function as donor states close to the conduction band edge. As a result, $Fe_2O_3/FeTiO_3$ interface is characterized by a strong depletion field, enhancing charge separation and hole injection into the electrolyte. Accordingly, a substantial improvement in PEC kinetics is achieved, leading to a 6-fold increase in photocurrent density compared to unmodified hematite. Based on this research, despite the band edges misalignment between hematite and ilmenite, the thin and discontinuous $FeTiO_3$ layer may provide sufficient coupling between surface-trapped holes and the electrolyte, allowing charge transfer to occur.

3. From raw materials: Biomass as an alternative carbon source

With the rise of global energy consumption and the intensification of climate crisis, finding alternative carbon sources to reduce reliance on petroleum has become increasingly urgent. Biomasses emerge as promising candidates due to their potential for improved sustainability and biodegradability. Coming from living organisms, such as animals and plants, they are usually categorized in three generations.

The first includes crops, such as corn and sugarcane, from which biodiesel and bioethanol can be produced. Their edible nature and limited production capacity relegate them as transitional solutions for meeting global fuel and chemical demands.

Second-generation feedstocks, such as lignocellulose, offer better long-term prospects. Lignocellulose is a low cost, non-edible biomass, derived from wood residues, straw, and crop stover. As the major component of plants, the estimated annual production of lignocellulose is around 2 x 10^{11} metric tons[70,71]. It consists of three primary components: cellulose, hemicellulose and lignin, which can potentially be converted into valuable building-block chemicals.

i) **Cellulose** (30-50 wt % of lignocellulose) is the most abundant polysaccharide on Earth, composed of D-glucose units connected by β-1,4-glycosidic linkages. Its extensive hydrogen bonding makes hydrolysis challenging[72], typically requiring acidic or enzymatic catalysts to release glucose units[73,74].

ii) **Hemicellulose** comprises 20-35 wt % of lignocellulose. Including various carbohydrates in its structure, such as xylose, arabinose and mannose[75], the depolymerization of hemicellulose can lead to useful building-blocks for the synthesis of functional sugar additives or for pharmaceutical applications. The dehydration of C5 sugars may also produce furfural compounds, commercially used in solvents, resins, and fuel additives[76–78].

iii) **Lignin:** constituting 15-20 wt % of lignocellulose, lignin is a precious natural source of aromatic compounds, consisting of highly cross-linked phenolic units[79]. To obtain them, a selective cleavage of C-O-C ether bonds is essential during depolymerization[80]. Traditional methods involve energy-intensive physical processes (e.g., ball milling, ultrasonication, plasma irradiation and microwave heating) and catalytic technologies, generating significant chemical waste. For a more sustainable production, a photo-electro-biochemical system has been recently developed[81].

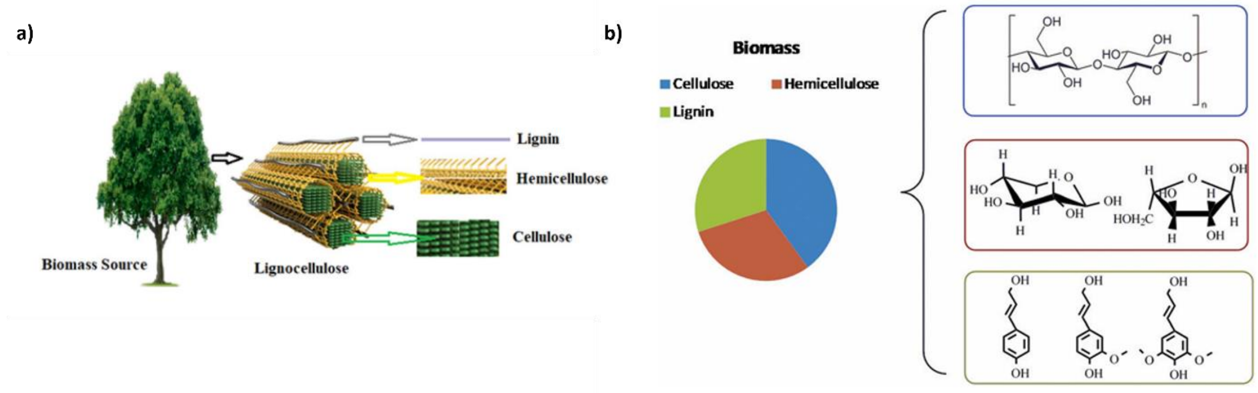

Figure 3.1 (a) *Schematic illustration of lignocellulose obtained from biomass source and its components. Figure adapted from reference*[82]. ***(b)*** *Pie chart of the three components of lignocellulose and illustration of their chemical structure. Figure adapted from reference*[83].

Considering the complex structure of lignocellulose, advanced technologies are necessary during the isolation and purification steps of depolymerization.

Algae are the third generation of biomasses. Thanks to their microbe's lipid content, they possess the right amount of carbon to produce all the types of biofuels, such as ethanol, butanol, biodiesel, propanol and gasoline. The interest in this source of bio-based hydrocarbons is increasing worldwide, driven by the algae's rapid growth in non-arable environments and their unique ability to capture CO_2[84].

4. Biomass valorisation to building block chemicals: HMF, “the sleeping giant”

One of the most appealing chemicals deriving from biomasses is 2,5-hydroxymethylfurfural (HMF). HMF is currently produced from edible biomass, lignocellulose and food waste. Notably, the latter approach is very promising, considering the massive annual dissipation of solid waste as well as its high carbon footprint[85].

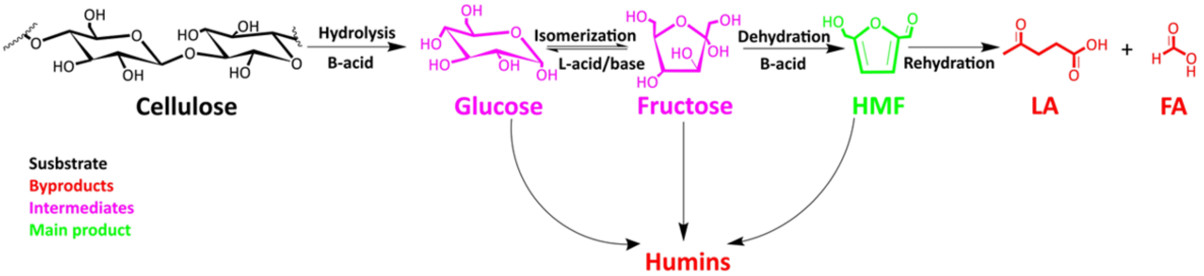

Figure 4.1 *Reaction mechanism of catalytic cellulose transformation into HMF. Image adapted from reference*[86].

As depicted in Figure 4.1, HMF is usually synthesized according to three consecutive steps:

1) Hydrolysis of glucan to glucose, catalysed by Brønsted acid;
2) Isomerization to fructose with Lewis acid as the catalyst;
3) Dehydration of fructose to HMF, catalysed by Brønsted acid.

The process is not so trivial, and side-reaction can take place. HMF can indeed undergo rehydration leading to levulinic acid (LA) or formic acid (FA), and/or cross-polymerization yielding to humins[86,87]. The one-pot synthesis from raw biomasses would be the best way to produce HMF, providing the lowest energy consumption and CO_2 emissions.

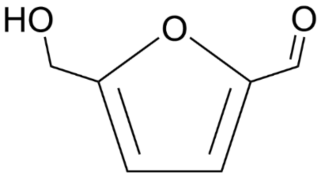

Figure 4.2 *chemical structure of 2,5-hydroxymethylfurfural (HMF).*

HMF is often referred to as a "sleeping giant" because of its huge potential to serve as a versatile platform chemical. As illustrated in Figure 4.2, its unique structure provides exceptional chemical flexibility, enabling the synthesis of a wide range of valuable compounds. For example, the hydroxyl and aldehyde groups at the 2 and 5 positions, can undergo oxidation to carboxylic acids or reduction to diols, which are crucial for polymer synthesis. These functional groups make HMF a key precursor in developing sustainable biopolymers, which could potentially replace petroleum-derived plastics.

The furanic ring in HMF structure also makes it a building block for pharmaceutically active molecules, further broadening its industrial relevance. Moreover, its unsaturated aromatic structure allows for the conversion into fuel molecules such as 2,5-dimethylfuran (DMF) through hydrogenation. DMF is considered a high-energy-density biofuel, comparable to gasoline.

Despite these varied and promising applications in biopolymers, pharmaceuticals, and biofuels, HMF full commercial potential remains largely dormant due to challenges in cost-effective, large-scale production. In addition, the limited stability of HMF, even for short-period storage, requires high purity maintenance to avoid oligomer or dimer formation[88].

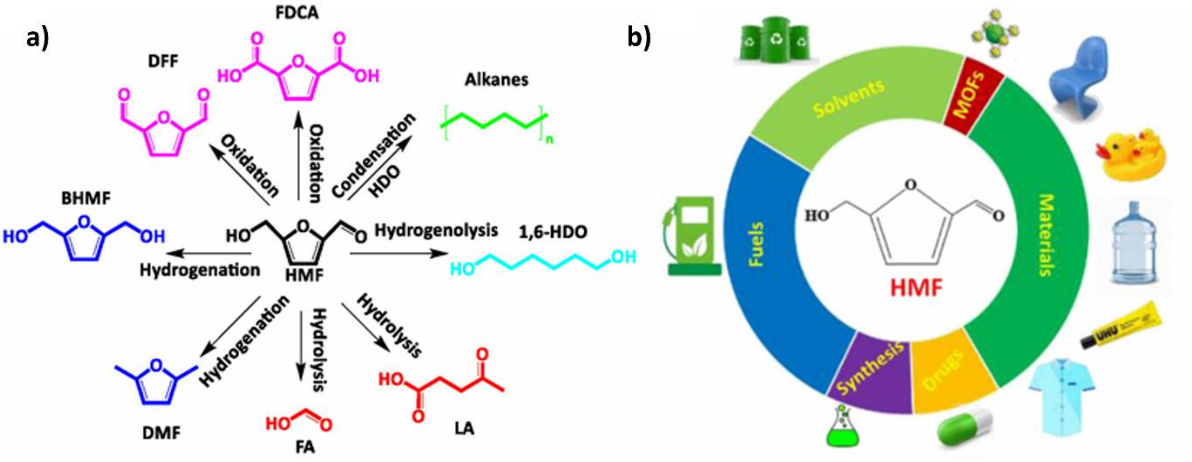

Figure 4.3 ***(a)*** *catalytic transformations of HMF into its derivatives,* ***(b)*** *main domains of practical applications of HMF and its derivatives. Figure adapted from reference*[86].

4.1 HMF oxidation to FDCA

Among the various pathways involving HMF as the starting compound, its oxidation to 2,5-furan dicarboxylic acid (FDCA) is the most extensively studied. FDCA is a valuable building block chemical for synthesizing polyethylene furanoate (PEF), a biopolymer with mechanical and chemical properties comparable to those of polyethylene terephthalate (PET), which in turn is derived from the fossil-based monomer terephthalic acid (TPA). The superior sustainability of FDCA compared to TPA is driving many companies to shift from PET to PEF production. A recent Life Cycle Assessment (LCA) shows that producing FDCA emits 1.6 kg of CO_2 per kg, while TPA production emits 1.8 kg of CO_2 per equivalent (i.e. 1 moles of charge). Additionally, FDCA has a fossil depletion value of 0.44 kg oil equivalent, compared to 1.17 kg for TPA[89].

Industrially, HMF is converted to FDCA through heterogeneous metal-based catalysis, which offers high productivity and efficient catalyst recovery. This process can be carried out under non-alkaline conditions, reducing by-product formation and facilitating catalyst recycling. However, given the increasing interest for PEF commercialization, the development of more sustainable methods for FDCA production is becoming increasingly urgent. In this regard, the homogeneous catalytic oxidation of HMF to FDCA is not so favourable, being energy and time consuming, with additional steps for catalyst recovery and regeneration. Therefore, alternative heterogeneous catalytic processes are being explored[89].

Biotechnological approaches involving cells and enzymes show good results in mild conditions but face challenges with FDCA isolation and purification, limiting their scalability[90,91].

Electrochemical and photocatalytic systems offer promising, green routes for HMF oxidation to FDCA. Electrochemical methods can integrate additional semi-reactions, such as H_2 production or CO_2 reduction, enhancing economic viability[92–94]. Photoelectrochemical (PEC) devices, which use sunlight to drive the oxidation of HMF to FDCA, further improve sustainability by potentially eliminating the need for external bias. Despite positive lab-scale results, challenges related to high costs and catalyst recovery may arise as these technologies move toward large-scale production.

In the following paragraph, the state-of-the-art for the HMF PEC conversion to FDCA is presented, highlighting the most appealing results both in terms of sustainability and Faradic efficiency (FE).

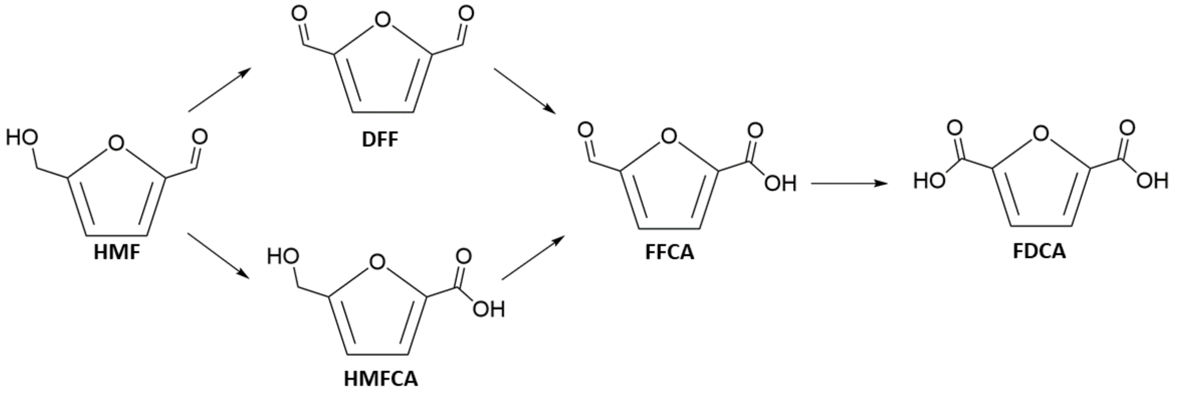

Figure 4.4 *HMF oxidation to FDCA is a stepwise synthesis which can follow two different oxidation pathways through 2,5- diformylfuran (DFF) or 5-hydroximethyl-2-furancarboxylic acid (HMFCA), leading to 5-formyl-2-furancarboxylic acid FFCA and eventually to FDCA.*

4.2 HMF photoelectrochemical conversion to FDCA

In a seminal paper, Choi et al.[95] demonstrated extremely efficient electrochemical HMF conversion to FDCA in basic conditions (borate buffer, pH 9.2), with almost unitary yield and Faradaic efficiency. The authors achieved comparable results with a $BiVO_4$ photoanode, with a reduction of ~700 mV in the potential necessary to initiate HMF oxidation. More recently, $BiVO_4$ photoanodes were modified with cobalt phosphate complexes, referred as CoPi, to improve the selectivity with respect to the competitive OER, pointing out the importance of the catalyst surface chemistry to tune the charge transfer pathways[96]. However, $BiVO_4$ suffered from limited stability to photo-corrosion and the photocurrent response with the addition of a CoPi overlayer drops to values as low as 0.2 mA cm $^{-2}$. Hematite photoanodes (α-Fe_2O_3) were also reported to efficiently promote HMF oxidation, highlighting a pH-dependent mechanism. The best results were achieved at pH > 12.5 (99.2% HMF conversion to FDCA, with a yield of > 90%)[97], despite the instability of HMF in such highly alkaline conditions[98]. In the above-mentioned results, 2,2,6,6-tetramethylpiperidine 1-oxyl (TEMPO) was always employed as redox mediator to improve selectivity towards HMF oxidation. The presence of the radical proved to be essential to scavenge photogenerated holes at the electrode's surface, accelerating their transfer to the organic species in the electrolyte[99]. At the same time, hole scavenging by TEMPO limited the formation of oxygen reactive species like OH radicals, formed upon monoelectronic water oxidation, which may trigger uncontrollable oxidation reactions. However, the elevated market price (5-10 $/g) and its potential degradation under reaction conditions, make the use of TEMPO problematic. In addition, once the reaction is complete, a further step must be introduced in the process scale-up to separate the scavenger from the reaction mixture.

Direct HMF oxidation in absence of TEMPO was also investigated by employing $BiVO_4$ photoanodes as well as WO_3 at different pH regimes, with the latter displaying high conversion rate, but very limited yield (<1%) for FDCA production[100]. *Table 4.1* summarizes the state-of-the-art of HMF photoelectrochemical conversion to FDCA:

Ref.	Photoanode	pH	Time (h)	HMF charge equivalent (%)	HMF (mM)	TEMPO (mM)	FE (%)	HMF Conversion (%)	FDCA yield (%)
[95]	$BiVO_4$	9.2	-	~100	5	7.5	93	> 99	> 99
[100]	WO_3	4	64	~100	5	-	-	90	0.5
[96]	$BiVO_4$/CoPi	9.2	2.7	~100	1	5	~90	98.8	88.0
[101]	Ti/TiO_2NT-1h-500-Pt	5	3	-	0.5	-	-	59	-
[97]	Fe_2O_3	12.5	5.5	~110	10	13	92.6	99.2	90.7
[97]	Fe_2O_3	12.5	20	-	10	6.5	-	42	23.4
[97]	Fe_2O_3	9	20	~370	10	13	12.6	47.3	1.6

According to *Table 4.1*, basic aqueous solutions and TEMPO mediator are essentials for a selective and efficient HMF oxidation to FDCA, with the best result achieved by Choi et al.[95] with $BiVO_4$ photoanode at pH 9.

It is known that the oxidation of aldehyde to carboxylic acid mediated by TEMPO takes place via the formation of a diol that is favoured in basic aqueous environment, according to the mechanism outlined in Figure 4.5. Therefore, the conversion of DFF, featuring two aldehyde groups, to FFCA is expected to be fast in the presence of TEMPO and in basic aqueous media. On the other hand, the conversion of FFCA to FDCA is supposed to be slower than the previous one (rate-determining step), because of the presence of only one aldehyde and of the negative charge of the deprotonated carboxylic group, which hinders the approach of the base OH^-.

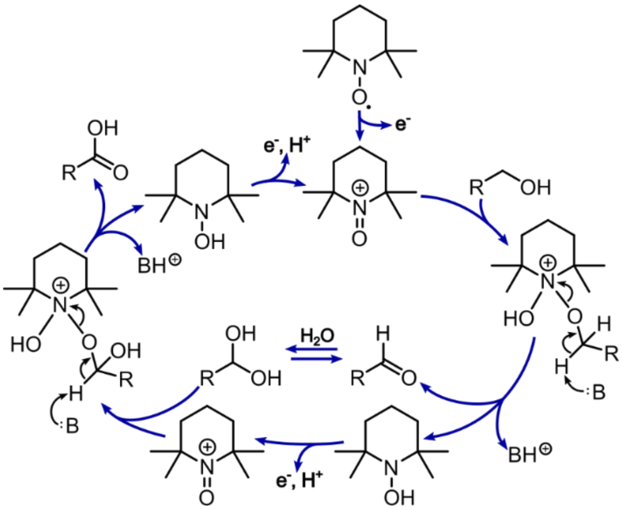

***Figure 4.5** Mechanism of the TEMPO-mediated oxidation of alcohols. Image adaptde from reference*[102].

An important parameter to consider is the pH level of the electrolyte. When highly alkaline solutions are employed, HMF is not stable and two possible pathways can be followed by the compound: i) it can degrade to humins: oligomers very difficult to detect with the common product analysis techniques, such as HPLC or NMR[98] or ii) it can undergo the Cannizzaro reaction, converting into DHMF or HMFCA which can still electrochemically oxidise to the desired product, FDCA. Depending on the base and substrate concentrations, as well as on the reaction temperatures, HMF will preferentially decompose according to one of these two routes[103,104]. The adjustment of these parameters is therefore essential to achieve a good yield for FDCA, even when highly alkaline solutions are employed. Local pH fluctuations can further decrease conversion efficiency, compromising the stability and performance of the photoanode. To mitigate this effect, buffer solutions are frequently used, and fresh ion exchange membranes are typically integrated into the system.

In this work, Ti:Fe_2O_3 photoanodes were employed for the PEC oxidation of HMF in basic aqueous environments. *Chapters 8* and *9* outline our efforts to optimize the synthesis process and develop effective methods for studying the reaction kinetics.

5. Biomass valorisation to building block chemicals: the "sweet taste" of glycerol [138]

Glycerol is a colourless, odourless, viscous liquid obtained from both natural and fossil feedstocks. The name glycerol derives from the greek word *"glykis"* which stands for "*sweet*" and highlights the peculiar, sweet taste of this molecule. Its structure is characterised by three hydrophilic hydroxyl groups which allow for the formation of both intra- and inter- molecular hydrogen bonds and provide hygroscopicity and solubility in water. The molecule is very stable under normal storage conditions and has no negative environmental effects.

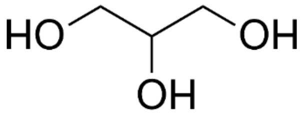

Figure 5.1 *Chemical structure of 1,2,3- propantriol (glycerol).*

There are thousands of applications in which glycerol is involved both as raw material and as an additive. Thanks to its no-toxicity and overall safety, it can be employed as solvent, sweetener and preservative in food and beverages, as emollient and humectant in cosmetics and even in personal care products. It is also used as starting material for the synthesis of trinitroglycerin, alkyd resins and polyurethanes. Glycerol is the oldest organic molecule isolated by humans, dating back to soap production around 2800 BC, and it encountered a massive request during World Wars I and II. At that time, a huge production of glycerol was necessary to meet the wartime demand of trinitroglycerin, from which dynamite was produced. Since the supply of glycerol from soap making was clearly insufficient, fossil oils started to be involved in the massive synthesis of this molecule, using high yield reactors. Nowadays, these plants are closing, as glycerol is widely available as a by-product of biodiesel production. This oversupply has driven down glycerol prices, making it a crucial platform for the synthesis of chemicals and fuels.

5.1 Glycerol from biodiesel synthesis

Biodiesel production starts from vegetable oil, animal fat, used cooked oil or yellow grease. The process involves a transesterification reaction, in the presence of a short-chain alcohol (usually methanol) and a catalyst, like sodium hydroxide (NaOH) or potassium hydroxide (KOH) and provides glycerol as the main by-product (Figure 5.2). Approximately, from 45.3 kg of fat or oil and 4.53 kg of methanol, 45.3 kg of biodiesel and 4.53 kg of glycerol can be obtained[105]. Glycerol refining is then performed by electrodialysis and nanofiltration, resulting in a colourless liquid with a high degree of purity. This approach requires high investments and operating costs, due to the employment of homogeneous catalysts and the formation of soap (from KOH). Novel methods have also been developed based on solid heterogeneous catalysts, such as Zn-Al oxides[106], or single-step synthesis via reactive or catalytic distillation[107,108].

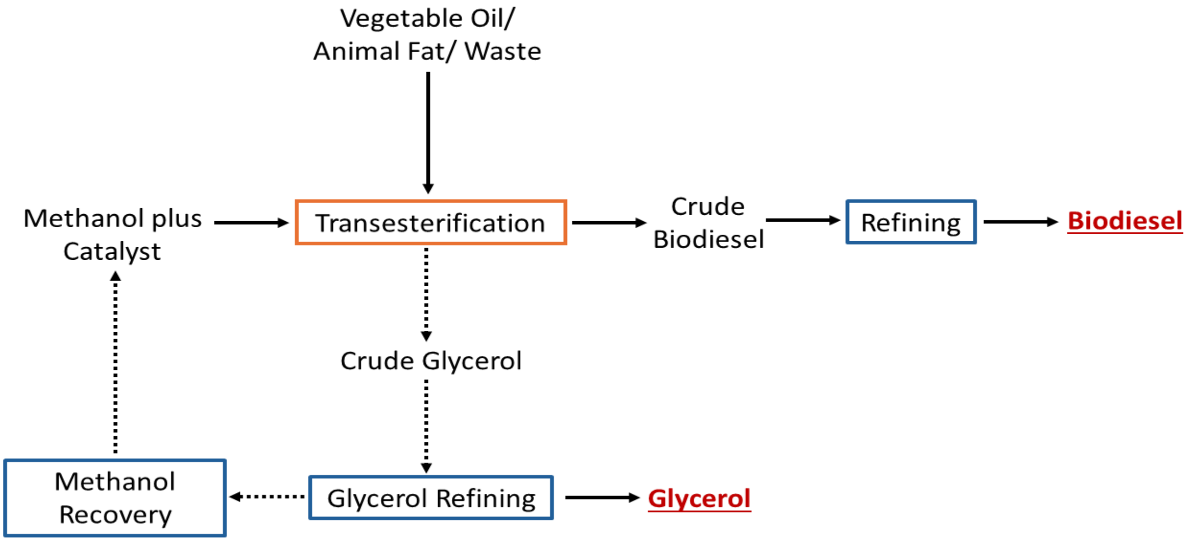

Figure 5.2 *Schematic of biodiesel production path and glycerol by-product formation through transesterification reaction*[105].

The large amount of glycerol generated during biodiesel synthesis greatly enhances the economic viability of the process. Beyond the direct applications of this organic substrate, glycerol oxidation products—such as glyceraldehyde (GLAD), dihydroxyacetone (DHA), glyceric acid (GLA), and lactic acid (LA)—are highly valuable, especially in the pharmaceutical and cosmetics fields. A key challenge in Glycerol Oxidation Reaction (GOR) is achieving selectivity for one specific intermediate, making the optimization of the synthetic process a critical factor to consider[109,110].

DHA is the glycerol's most valuable oxidative intermediate with the largest market demand, being the only FDA-approved ingredient for sunless tanning and hair colouring[111,112]. Currently, its production relies on complex and time-consuming microbial fermentation. Alternatively, thermal or electrochemical oxidations are performed using expensive noble catalysts (Au, Ag, Pt and Pd) and external oxidants, often resulting in low production rates and poor selectivity for DHA[113]. Recently, a PEC system employing porous nanoarray $BiVO_4$ photoanodes achieved remarkable selectivity for DHA at pH 2, producing 20 mmol of DHA per square metre of illuminated surface in just one hour without the need for additional oxidants[114]. The PEC approach utilises renewable energy sources and allows for precise control of reaction conditions providing a greener, more efficient alternative with the potential to greatly enhance product selectivity[24,115–119]. In *Chapter 10*, $BiVO_4$ photoanodes were synthesised and tested to perform GOR within a flow PEC cell. Rather than focusing on improving photoconversion efficiency, we aimed to enhance the material's long-term stability to effectively exploit this photoanode in such a favourable anodic reaction.

6. Characterization techniques

6.1 PEC measurements

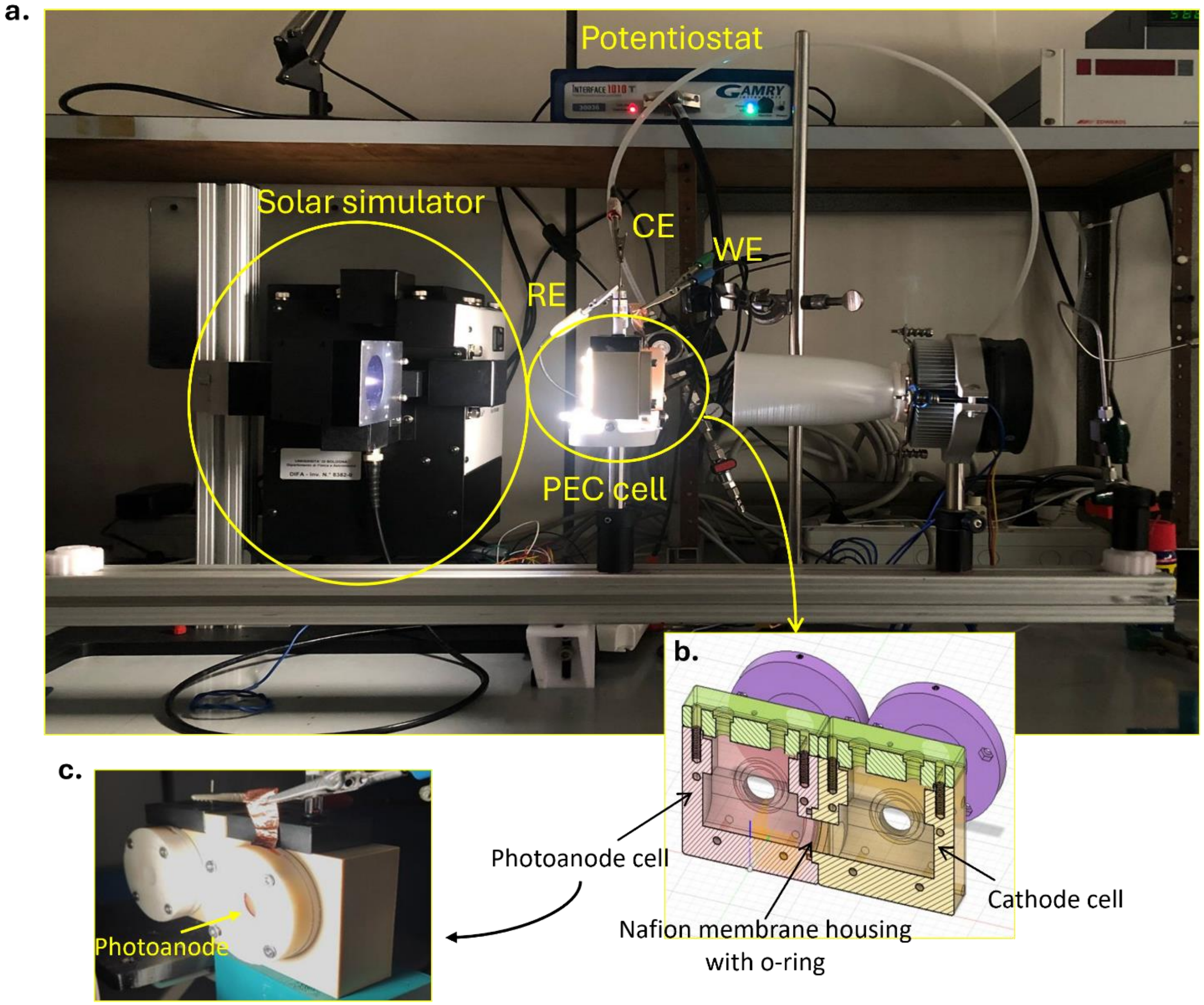

Figure 6.1 *Experimental setup for PEC measurements* ***(a)*** *The solar simulator, PEC cell, and potentiostat are displayed. RE, CE, and WE indicate the leads for the reference, counter, and working electrodes, respectively;* ***(b)*** *detailed view of a two-compartment PEC cell;* ***(c)*** *picture highlighting the illumination spot on the photoanode*

.

Figure 6.1 depicts the experimental setup used for PEC experiments. The potentiostat, either a Gamry Interface 1010E or VersaSTAT 3F, functions as the central control unit, applying potential to the counter electrode, which in turn polarizes the working electrode. This configuration allows for continuous monitoring of the potential difference between the working and reference electrodes, while simultaneously measuring the resulting current. For the experiments, a custom-built PEEK cell was employed under a three-electrodes configuration (Figure 6.1a). The working electrode—specifically, a metal oxide semiconductor (MOS)—was the photoactive material positioned at the anodic compartment of the PEC cell. An AM 1.5G illumination (100 mW cm^{-2}) was provided to the backside of the photoanode by a solar simulator. In addition to the working electrode, a platinum (Pt) wire was used as the counter electrode, while the reference electrode was selected according to the electrolyte's pH: Ag/AgCl for pH 9 and pH 2, Hg/HgO for pH 13. For a two-compartment setup, a Nafion membrane (N-117, 0.007-inch thickness) was placed between the compartments of the cell (Figure 6.1b). In certain cases, the experiments were conducted under flow conditions as specified.

In the Cyclic Voltammetry (CV) and Linear Sweep Voltammetry (LSV), the potential of the working electrode is linearly swept over a defined range at a constant scan rate (mV/s) and the resulting current is measured. This produces a (photo)current-voltage plot, which provides key insights into the specific (photo)electrochemical behaviour of the working electrode, revealing the redox processes occurring on its surface. In Chopped LSV, the light is periodically switched on and off during the potential sweep through external modulation (Figure 6.2). This allows the simultaneous collection of both light and dark responses of the photoanode on the same plot, reducing noise and enhancing the signal-to-noise ratio.

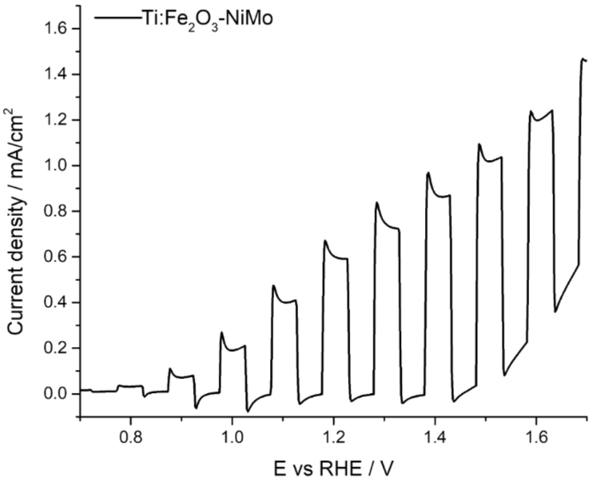

Figure 6.2 *Examples of a chopped LSV acquired at pH 13 by using a Ti:Fe_2O_3 photoanode modified with a NiMo co-catalyst overlayer.*

For PEC conversion experiments, either chrono-amperometry (CA) or chrono-coulometry (CC) were conducted, by applying a constant potential over time. Alternatively, for chrono-potentiometric (CP) measurements, a constant current was applied over time. In all cases, the total charge measured was used to calculate the Faradaic Efficiency (FE), providing quantitative information on the species involved in the redox process. FE was determined as follows:

$$FE(\%) = \frac{nmol}{\frac{Q}{nF}} \cdot 100 \quad (6.1)$$

where $nmol$ is the number of moles of product experimentally measured, Q is the cumulative charge passed through the PEC cell, F is Faraday constant (96.485 C mol^{-1}) and n is number of electrons exchanged during the oxidative step.

Although the potential of the working electrode was measured against the reference electrode, all results are reported against the reversible hydrogen electrode (RHE). This standardization facilitates comparison with H_2O/O_2 redox levels and other studies using different electrolytes and pH values. The conversion is done using the Nernst equation:

$$E\ (vs\ RHE) = E\ (vs\ Hg/HgO) + E_{\frac{Hg}{HgO}} + 0.059 \cdot pH \quad (6.2)$$

where $E_{Hg/HgO}\ (reference) = 0.140V\ vs\ NHE\ at\ 25°C$

When Ag/AgCl is used as the reference electrode:

$$E\ (vs\ RHE) = E\ (vs\ Ag/AgCl) + E_{\frac{Ag}{AgCl}} + 0.059 \cdot pH \quad (6.3)$$

where $E_{Ag/AgCl}\ (reference) = 0.197\ V\ vs\ NHE\ at\ 25°$

6.2 Electrochemical Impedance Spectroscopy (EIS)[120]

During an EIS experiment the impedance of an electrochemical system is measured upon application of a small-amplitude stimulus (voltage or current) to the system. The resulting response (current or voltage, respectively) is analysed over a wide range of frequencies. The application of a small-amplitude perturbation is necessary to guarantee linearity between the input and the measured output signals. Such excitation is provided with a sinusoidal perturbation signal, usually superimposed with a direct current (*dc*) signal, such as the open circuit potential (OCP) where no current flows.

Modern electrochemical analysers are characterized by a potentiostat-galvanostat and a Frequency Response Analyser (FRA). The first applies a *dc* voltage (or current, in the case of galvanostat), while the second ensures the sinusoidal perturbation signal to the cell and analyses its response into its real and imaginary components. Figure 6.3 illustrates a conventional potentiostatic EIS setup.

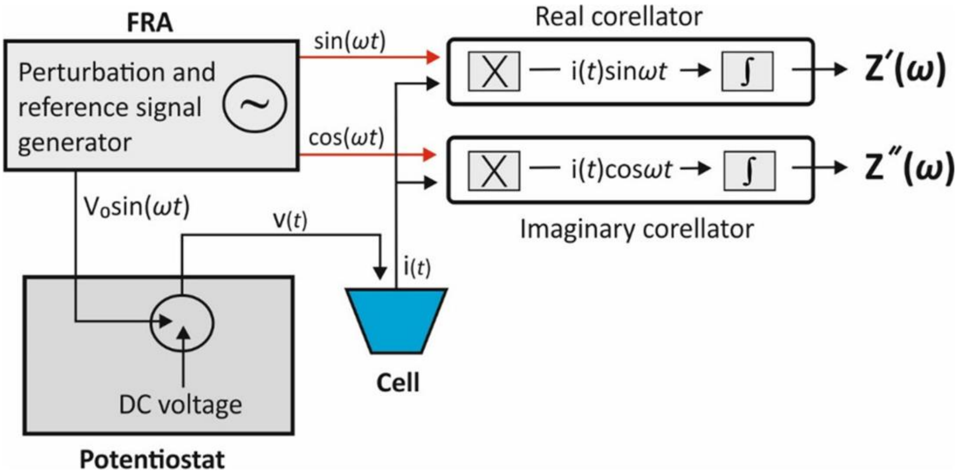

Figure 6.3 *Simplified experimental setup for potentiostatic EIS and working principle of a frequency response analyser. "X"stands for multipliers and "∫" for integrators. Image adapted from reference*[120].

FRA generates a sinusoidal voltage excitation signal at a specific frequency, $V_0 sin(\omega t)$, which is superimposed over a dc voltage signal and applied to the cell via the potentiostat. At the same time, two synchronous reference signals, one that is in-phase $[sin\ (\omega t)]$ and a second one that is out-of-phase by 90° $[cos(\omega t)]$ with the sinusoidal voltage perturbation are generated. The sinusoidal response of the cell, $i(t)$, is analysed by correlating it with these reference signals, isolating the fundamental components and calculating both the real and imaginary parts of the impedance. This process is repeated at various frequencies set by the user and in the end the impedance spectrum is constructed. While many applications only require frequencies ranging from 1mHz to 100kHz, studies involving solid electrolytes need measurements at higher frequencies (until 1MHz) to fully describe their impedimetric behaviour.

The impedance data can be plotted in different formats and the most used ones are the Nyquist and Bode plots. In the Nyquist plots, $-Z'' = f(Z')$, the imaginary part of the impedance, $-Z''$, is plotted versus the real part of the impedance, Z', at each excitation frequency. One significant drawback of this visualization method is the absence of direct frequency-impedance matching. Instead, Bode plots show two curves: the $log|Z| = f(log\ f)$ and the $-phase = f(log\ f)$, thereby providing an easy matching of the excitation frequency with the module of impedance and the phase values.

The data can be simulated to match an equivalent electrical circuit, providing insight into the various electrochemical processes involved. The modelling may depend on various factors, such as the experimental setup (2,3 or 4 electrodes configurations), the presence of a redox species, the morphology of the working electrode (whether it is porous or not), the presence of mass transport phenomena or inductive behaviours. For example, in a 3-electrode, 4-terminal setup, the voltage is applied between the working and reference electrodes and, when a small amplitude voltage perturbation is applied, the impedance to current flow is influenced by three main factors:

- The ohmic resistance of the electrolyte between the reference and the working electrode, also known as uncompensated resistance (R_u). Its value depends on the distance between the two electrodes and practically is also influenced by the resistance from the connection cables and the working electrode itself.
- The charging/discharging of the electric double layer which, under alternating current (ac) conditions, behaves like a capacitor at the electrode/electrolyte interface and is represented as C_{dl}.
- The polarization resistance (R_p), which is defined as the slope of voltage-current curve ($R_p = \Delta V/\Delta I$) during steady state measurements.

When a redox species is also present in the electrolyte, the impedance is measured through the so-called Faradaic EIS measurement, in which the small sinusoidal voltage perturbation applied on top of a dc potential, matches the standard potential (E^0) of the redox reaction. In this scenario, the total current passing through the R_u is split into two components: the current related to the charging/discharging of the electrical double layer (i_c) and the current related to the faradic process (i_F). The faradic process is represented by the impedance Z_F in the equivalent circuit, which in turns is divided in two components:

$$Z_F = R_{ct} + Z_W \quad (6.4)$$

- R_{ct} is the charge-transfer resistance, related to the kinetics of the electrochemical reaction, assuming no absorption of the redox species in the electrode's surface. Its magnitude depends on the electron transfer rate, the number of electrons exchanged, temperature, electrode surface area and the concentration of the redox species.
- Z_W is the Warburg impedance and represents the resistance due to mass transport of the redox species to the electrode surface, considering semi-infinite linear diffusion. It is represented by a $R_W - C_W$ circuit in series, where both R_W and C_W are frequency dependent.

The equivalent electrical circuit involving the charge-transfer resistance (R_{ct}) and Warburg impedance (Z_W) is commonly known as Randles circuit.

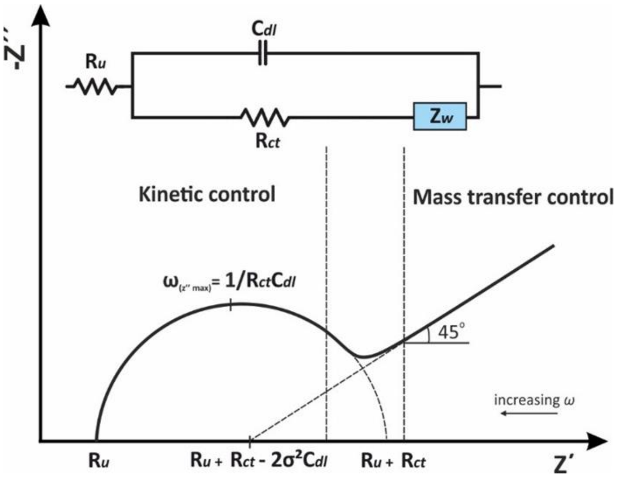

Figure 6.4 *Randles equivalent electrical circuit over a wide frequency range. Image adapted from reference*[120].

In real electrochemical systems, the Nyquist plot of a faradic impedance spectrum is typically characterised by both a semicircle and a straight line across a wide range of frequency (Figure 6.4). The semicircle, located at higher frequencies, represents R_{ct} and indicates that the electrochemical process is mostly regulated by the charge transfer kinetics at the interface. Instead, the straight line occurring at lower frequencies is related to Z_W and indicated that in this region the mass transport phenomena dominate. The exact shape and the extent of these features within the Nyquist plot may vary depending on the values of C_{dl}, R_{ct} and Z_W.

The modelling systems described above are examples of ideal behaviours which can be obtained experimentally only when dealing with perfectly flat electrode, such as the liquid Hg drop electrode. With common solid electrodes the impedimetric profiles of Nyquist plot are always far from ideal. In these cases, the impedance data can be sufficiently modelled by replacing the ideal capacitor (C_{dl}) with the so-called Constant Phase Element (CPE). The impedance of CPE is described by the following equation:

$$Z_{CPE} = \frac{1}{Y_0(j\omega)^n} \quad (6.5)$$

where Y_0 in $F \cdot s^{n-1}$ is the parameter containing the capacitance information, and n is the constant ranging from 0 to 1. The exponent n defines the deviation from the ideal behaviour and is related to the angle θ by $\theta = 90°(1-n)$, where θ is the phase deviation from the ideal case ($\varphi = 90°$).

When modelling the electrochemical system according to the impedimetric profiles, it is essential to keep the circuit as simple as possible to successfully correlate the elements with electrochemical processes.

In this thesis, the electrochemical impedance response of illuminated Ti:Fe_2O_3 photoanodes (*Chapter 8, Section 8.4*) was provided by applying a 10 mV sinusoidal perturbation in the 2×10^4 -5×10^{-2} Hz, by using an EcoChemie FRA2 frequency response analyser. The current/voltage characteristic of each photoanode was sampled at 20 mV intervals from the OCP to the limiting photocurrent plateau. Fitting of EIS data in terms of electric equivalents was achieved with Zview with typical relative errors < 10%.

6.3 Intensity Modulated Photocurrent Spectroscopy (IMPS)

IMPS technique relies on the application of a small perturbation of light intensity $\varphi_{inc}(\omega)$ from which the modulated photocurrent response $I_{ph}(\omega)$ is measured over a wide range of frequencies ω. The response function $Y(\omega)$ has the form of an admittance and is calculated as:

$$Y(\omega) = \frac{I_{ph}(\omega)}{\varphi_{inc}(\omega)} \quad (6.6)$$

Similarly to EIS measurements, a direct current (dc) light bias is applied to maintain the system close to real working conditions and the amplitude of the sinusoidal light perturbation is kept small (usually lower than 10% of the intensity of the applied dc photovoltage), to ensure linearity between input, light stimulus, and output, photocurrent, signals.

Figure 6.5 illustrates the typical IMPS setup. A light-emitting diode (LED) is the light source, modulated by a LED driver (Thorlabs DC2100). A beam splitter directs part of the light to the sample, and the other to a calibrated silicon photodiode (Hamamatsu). For the experiments described in this thesis, the sample was a semiconducting photoanode placed within a PEC cell connected to a PGSTAT204 electrochemical workstation. Thanks to this arrangement, IMPS allows to simultaneously measure the incident light intensity, and the photocurrent generated out of the sample. This is essential for normalizing the photocurrent data and obtaining the transfer function described in *Equation 6.6*.

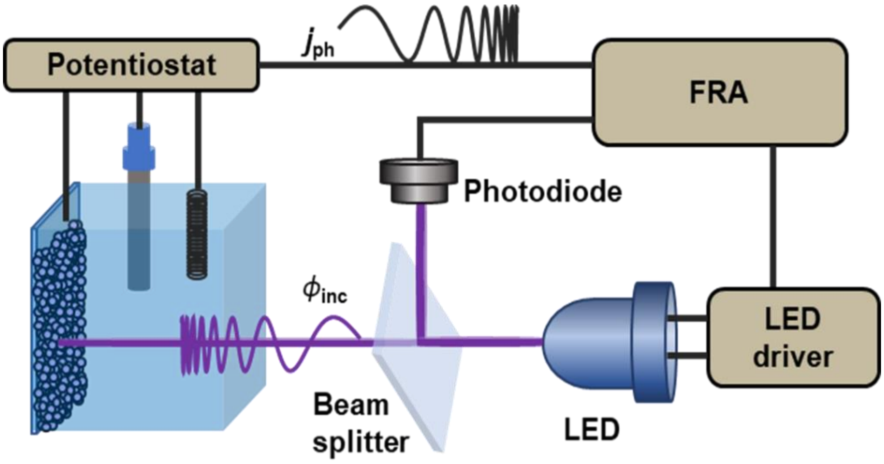

Figure 6.5 *Schematic of a typical Intensity Modulated Photocurrent Spectroscopy (IMPS) setup.*

The incident light intensity is modulated at specific frequencies, ranging from few Hz to several MHz. In our setup, the modulation was achieved thanks to a frequency response analyser (FRA), which was part of the PGSTAT204 electrochemical workstation. FRA generates alternating current (ac) signals at different frequencies which are superimposed with a dc potential signal from an operational amplifier. This combined signal is then sent to the LED driver where it is converted into the current that powers the monochromatic LED. For small variations, the LED light intensity remains directly proportional to the current, and thus to the ac potential generated by the FRA. As the light is modulated, the resulting photocurrent in the material oscillates at the same frequency.

The light intensity detected by the silicon photodiode is converted into a current, which is calibrated according to its responsivity, dependent on the specific wavelength used in the experiment. This current is then amplified by a current amplifier to produce a voltage signal. Similarly, the current generated at the photoelectrode is measured at the counter electrode and converted into a voltage signal, based on the current range selected during measurements. Both light intensity and photocurrent signals are then fed back as voltage inputs to the FRA for data analysis. The FRA measures the amplitudes of the two sinusoidal ac signals, determines their phase shift, and calculates the quantity $Y(\omega)$ using *Equation 6.6* for each frequency in the experiment.

$Y(\omega)$ is a complex number with both real and imaginary components, which are used to create a Nyquist plot, that is a common representation of IMPS spectra. The Nyquist plots offer insights into the charge carrier dynamics and recombination processes occurring at the electrode/electrolyte interface. Having valuable tools to analyse those plots is essential to get information about charge carrier lifetime, mobility and recombination mechanisms. In this way, the performance and efficiency of the semiconductor can be evaluated, aiding in the optimization and design of its functionalities.

6.3.1 The rate constant model in IMPS

The theoretical foundation for IMPS was developed by Peters and coworkers in the late 1980s-1990s[121,122]. Their calculations are based on the solution of kinetic equations describing systems involved in single or multistep processes. However, those equations require certain assumptions, such as the specific reaction mechanism, which can be challenging to accurately determine. Therefore, the model of the system was simplified to the most basic scenario, where only two kinetic processes can occur: the transfer of holes from the semiconductor surface to the electrolyte (k^{trans}) and the recombination of these holes at the surface with bulk electrons (k^{rec})[123,124]. This simplified model, known as the Rate Constant Model (RCM), makes it more difficult to identify multistep and parallel processes occurring in more complex system, such as nanostructured heterojunctions.

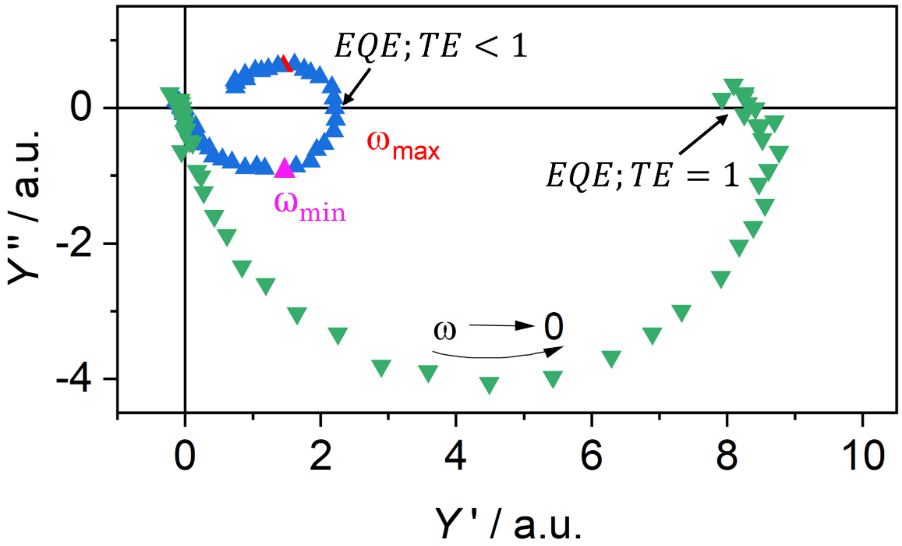

Figure 6.6 *IMPS spectra at different applied potentials. The blue curve represents the behaviour at low potentials, where the External Quantum Efficiency (EQE) decreases due to low transport efficiency (TE). In contrast, the green curve illustrates the behaviour at higher potentials, where surface recombination is minimal, and TE is assumed to be 1, indicating optimal charge transport.* Y'' *is the axis of the imaginary component, while* Y' *is the axis of the real component.*

Typical Nyquist plots at different applied potentials are illustrated in Figure 6.6. These plots are generally described by a high-frequency region and a low-frequency region. At the lowest frequency (right-end side of the plot), the photocurrent aligns in phase with the modulation of the incident light, causing the spectrum to intercept the real axis where $Y'' = 0$. This intercept corresponds to the steady-state photocurrent under the given experimental conditions. As the frequency increases, the photocurrent begins to lag the modulation of the incident light, driven by a competition between charge transfer and recombination processes at the surface. This dynamic gives rise to the "recombination semicircle" in the first quadrant (upper-right portion of Figure 6.6), clearly observed in the blue Nyquist plot obtained at low potential. The point where the imaginary component (Y'') reaches its maximum value, denoted by ω_{max} (red dot in Figure 6.6), serves as a key parameter. It provides critical information about the kinetics of charge transfer and recombination, as expressed in *Equation 6.7*:

$$\omega_{max} = k^{trans} + k^{rec} \quad (6.7)$$

As the spectrum crosses the real axis again, Y becomes proportional to the number of charge available for transfer into the solution. At the very high-frequency limit, the system transitions to a state where no photocurrent is produced, and the plot eventually converges to the origin ($Y'' = 0, Y' = 0$).

At ω_{min} (pink dot in Figure 6.6) the system reaches the maximum phase lag between the modulated light input and the photocurrent response. This is the most negative point of the imaginary axis and corresponds to the characteristic time constant (τ_{cell}) of the PEC system: $\tau_{cell} = (2\pi\omega_{min})^{-1}$. A shift in ω_{min}over time can indicate performance degradation in the PEC cell. The time constant τ_{cell} can be also related to the impedance of the cell, by using *Equation 6.8*:

$$\tau_{cell} = \mathrm{R}\frac{C_{SC}C_H}{C_{SC} + C_H} \quad (6.8)$$

where R is the total series resistance comprising the electrolyte, the semiconductor bulk and the ohmic contacts, C_{SC} is the capacitance of SCL and C_H is the Helmholtz capacitance[121].

The fourth quadrant semicircle (the bottom-right portion of the Nyquist plots in Figure 6.6) is typically referred to as the “generation semicircle”. It represents generation-limited processes, providing insights into the system's response speed to incident light modulation. This semicircle is likely distinct from the recombination semicircle in the first quadrant and from other low-frequency semicircles associated with interfacial kinetics.

In addition, the size of the recombination semicircle in the first quadrant gives information about the Transfer Efficiency (TE) of the system, which is also related to the transfer and recombination rates by *Equation 6.9*[125]:

$$TE = \frac{k^{trans}}{k^{trans}+k^{rec}} \quad (6.9)$$

By combining *Equations 6.7* and *6.9*, k^{trans} and k^{rec} can be determined.

Summarizing Figure 6.6, the presence of a positive semicircle in the blue plot suggests that, at low potential, recombination prevails over hole scavenging at the surface, leading to TE < 1. Conversely, if the positive semicircle is absent (green plot, high potential), charge transfer is significantly faster than surface recombination (TE =1), and the External Quantum Efficiency (EQE, see *Equation 6.11* for the definition) is primarily determined by the rate at which holes are transferred to the electrolyte. Another interpretation of IMPS spectra was proposed by Gutiérrez et al.[126], who normalized the IMPS transfer function, $Y(\omega)$, by dividing the photocurrent ($I_{ph}(\omega)$) for the electronic charge (e) and the incident light intensity ($\varphi_{inc}(\omega)$) by hc/λ, where λ is the wavelength of the incident photons. The resulting equation is:

$$Y(\omega) = \frac{I_{ph}(\omega)}{\varphi_{inc}(\omega)} \cdot \frac{hc}{\lambda e} \; (6.10)$$

In this way, $Y(\omega)$ represents the ratio between the number of photogenerated charge carriers and the number of incident photons, effectively describing the efficiency of the photoelectrode.

Using this approach, the intercept of Y with the real axis is equal to $LHE \times CSE$, where LHE (Light Harvesting Efficiency) is the fraction of light absorbed by the material at each wavelength, and CSE (Charge Separation Efficiency) represents the amount of photogenerated holes available for the oxidation reaction in the electrolyte, providing insights into the material transport properties. The intercept with the real axis at the lowest frequency corresponds to the External Quantum Efficiency (EQE), which represents the overall efficiency of the system and is given by:

$$EQE = LHE \times CSE \times TE \; (6.11)$$

EQE is also interpreted as the ratio of the number of holes transferred to the electrolyte to the number of absorbed photons, offering valuable information about bulk transport and surface recombination processes in the photoanode.

Overall, these kinetic analyses assumes that maxima and intercept values can be easily extracted from the IMPS spectrum, but this is not always straightforward. For accurate interpretation, the IMPS spectrum must display well-defined generation and recombination semicircles with clearly separated characteristic times (or frequencies), ensuring that $\tau_{cell} \ll 1/\omega_{max}$.[121] However, achieving this condition in real systems is challenging. For example, when the rate constant of the cell, τ_{cell}, is close to the charge separation time constant, the two semicircles can overlap and merge into a single, distorted semicircle in the complex plane. A more effective approach for deconvolving generation and recombination processes with similar characteristic times involve applying the Lasso-Distribution of Relaxation Times (L-DRT) algorithm, which will be explained in the next paragraph.

6.3.2 Lasso-Distribution of Relaxation Times (L-DRT) for IMPS data fitting[127]

The Distribution of Relaxation Times is a technique applied to EIS or IMPS measurements for an accurate interpretation of impedance or admittance data obtained from a complex (photo)electrochemical system. It deconvolves the frequency-resolved response of the system and reveals the characteristic timescale of each process.

As explained above, the RCM model assumes a uniform distribution of photogenerated minority charge carriers across the semiconductor's surface, where they can either be transferred to the electrolyte at a rate constant k^{trans} or recombine with majority carriers from the bulk at a rate constant k^{rec}. However, in most realistic scenarios, i.e., nanostructured heterojunctions, catalytic or porous layers, the photoelectrode surface is not homogeneous, and the minority carriers distribute across various accumulation sites[122,123]. Each accumulation site n is characterised by a fraction of holes (p_n) relative to the total hole flux towards the surface (I_{flux}), with distinct rate constants k_n^{trans} and k_n^{rec} and resulting in $\sum_n p_n = 1$. No redistribution between different accumulation sites is accounted during the experiment. Consequently, numerous processes with distinct, and sometimes closely related, characteristic times can occur at the interface. The DRT approach accommodates this complexity, offering a more effective description of charge carrier dynamics at the electrode/electrolyte interface.

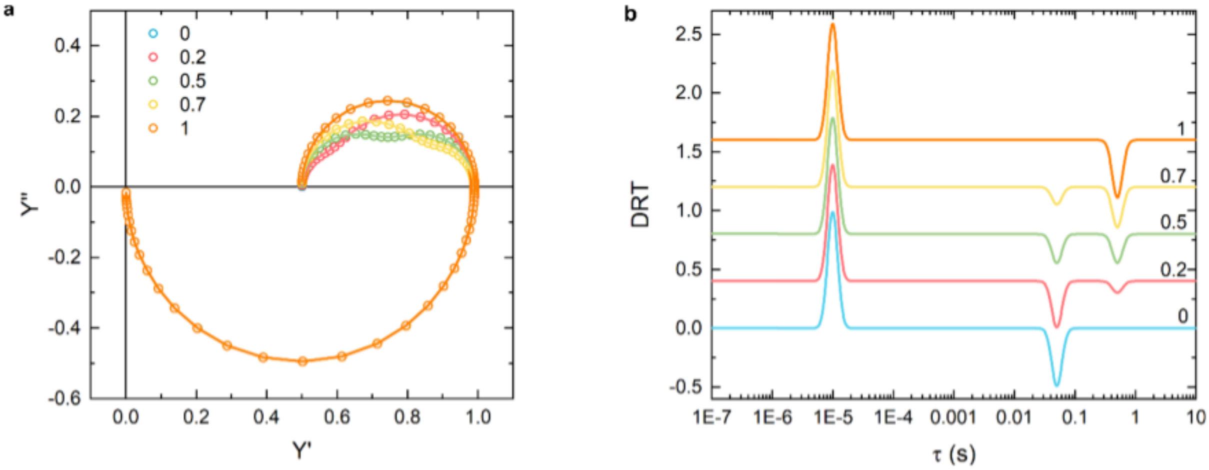

Figure 6.7 (a) *IMPS spectra generated using $\tau_{cell} = 10^{-5}s$, with the corresponding fitting curve. Each color corresponds to a specific operating voltage.* ***(b)*** *GL-DRT curves (in this case positive peaks are normalized to 1). Image adapted from reference* [127].

Figure 6.7 shows the results for the application of a L-DRT algorithm to a Nyquist plot of a more complicated PEC system. The Nyquist plot exhibits a negative semicircle at high frequencies and a distorted semicircle at low frequencies. Upon application of the L-DRT algorithm, the information contained within these semicircles is resolved and the various processes happening at the electrode/electrolyte interface are discerned and assigned to a specific characteristic time.

As a result, a single positive peak is obtained at short times (high frequencies), typically associated with charge separation phenomena, while multiple negative peaks appear at longer times (low frequencies) generally related to recombination phenomena. Notably, these negative peaks, which were previously represented by the distorted semicircle in the Nyquist plot, are now clearly distinguished at each characteristic time after deconvolution.

The area under these peaks, $g(\tau_n)$, is used to calculate critical physical quantities, such as the Gartner current ($I_{Gartner}$)[128] and the recombination current (I_{rec}) which together relate to the photocurrent measured in the external circuit (I_{ph})[121,122,129] as:

$$I_{ph} = I_{Gartner} - I_{rec} \quad (6.12)$$

$I_{Gartner}$ describes the flux of holes moving toward the surface, while I_{rec} corresponds to the current generated by the recombination of bulk electrons with holes trapped at the surface. These two currents have opposite signs due to the movement of both electrons and holes toward the surface.

From L-DRT analysis and under certain approximations, it is also possible to calculate the rate constants k_{LD}^{trans} and k_{LD}^{rec}, which describe the overall dynamic behaviour of the PEC system at the electrode/electrolyte interface. Unlike the RCM model, the calculation of these parameters is independent of the shape of the Nyquist plot, providing a more reliable and quantitative description of charge carrier dynamics at the interface.

6.4 X-ray Absorption Spectroscopy (XAS)

X-ray Absorption Spectroscopy (XAS) is a powerful technique used to measure the absorption of incident X-rays by matter, including atoms, molecules, and condensed systems, as a function of energy or wavelength (Figure 6.8a). In XAS spectra, absorption intensity increases sharply at a specific incident energy, known as the absorption edge or simply the edge. This edge represents the minimum energy required to ionize a core electron in atoms and molecules or to excite a core electron into unoccupied states just above the Fermi level in solids. The XAS spectrum extends beyond the absorption edge to higher energies, providing valuable insights into the electronic and atomic structures of materials.

As shown in Figure 6.8b, XAS can be categorized based on their energy range relative to the absorption edge. The X-ray Absorption Near Edge Structure (XANES) comprises X-ray energies close to the absorption edge (~100 eV around the edge) and is characterized by sharp resonance peaks. This region is sensitive to local atomic states and symmetry and provides insights into the oxidation state and local geometry of the analysed element. The Extended X-ray Absorption Fine Structure (EXAFS) is located after the XANES region and extends up to ~1000 eV or greater than the absorption edge. It appears as gentle oscillations and it is caused by scattering of the ejected electrons by neighbouring atoms. Therefore, EXAFS region reveals information about the local structure surrounding the element, including the number of neighbouring atoms, their chemical identity, and their spatial arrangement around the absorber. The term X-ray Absorption Fine Structure (XAFS) encompasses both XANES and EXAFS, and from these spectra, researchers can extract detailed information about the electronic and atomic arrangements within solids[130].

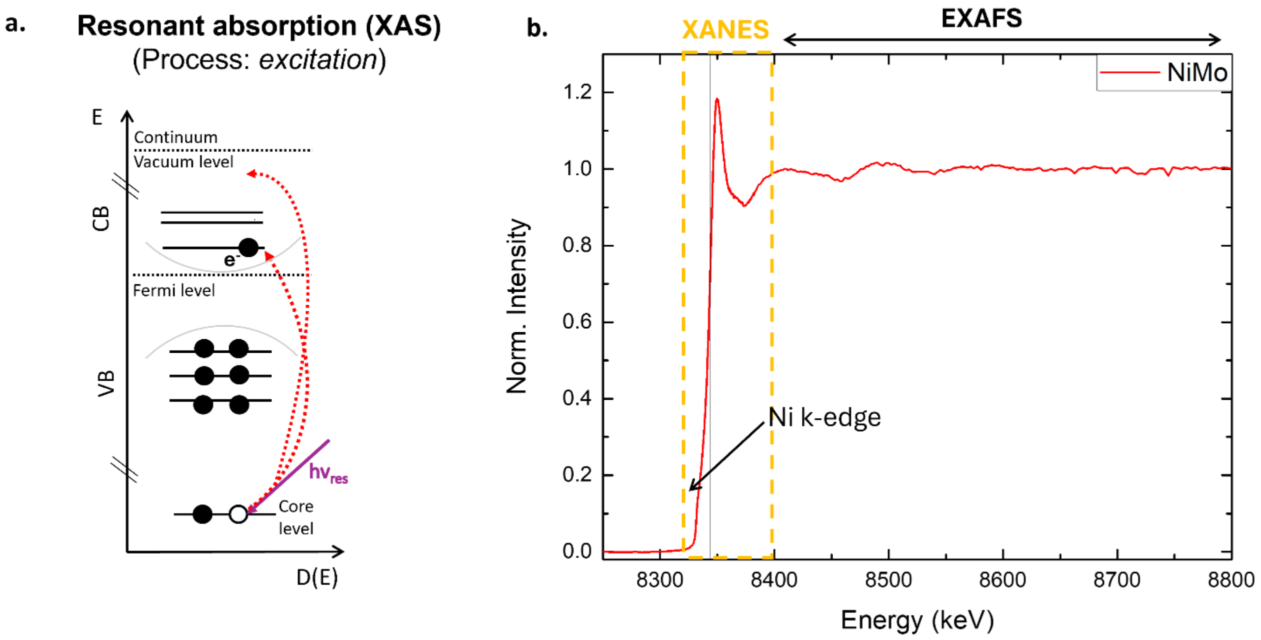

Figure 6.8 ***(a)*** *Core electron transitions induced by X-ray interaction, leading to resonance absorption in X-ray Absorption Spectroscopy (XAS).* ***(b)*** *Ni K-edge spectrum from NiMo co-catalyst deposited on FTO substrate. Image acquired at the LISA BM-08 beamline at ESRF in Grenoble.*

6.4.1 Operando X-ray Absorption Spectroscopy

In *Chapter 9*, operando X-ray absorption measurements were conducted using a custom-developed experimental setup fully integrated with the beamline. The operando technique allows to track the real-time evolution of the XAS spectrum under varying potentials and/or illumination conditions. This enabled a detailed element-specific analysis of the charge transfer and recombination processes occurring at the interface.

Figure 6.9 shows the experimental setup. The applied potential and current of the cell are monitored using a potentiostat, which feeds the data directly into the beamline's acquisition system to ensure precise synchronization between electrochemical and fluorescence measurements. Additionally, a pulseless 3D-printed peristaltic pump controls the electrolyte flow, improving mass transport and facilitating the removal of gaseous products from the electrode surface. The custom-designed 3D-printed cell (Figure 6.9b and c) minimizes the electrolyte thickness in front of the sample (~100 µm), reducing X-ray signal attenuation. This setup is compatible with both vacuum and helium atmospheres within the main chamber.

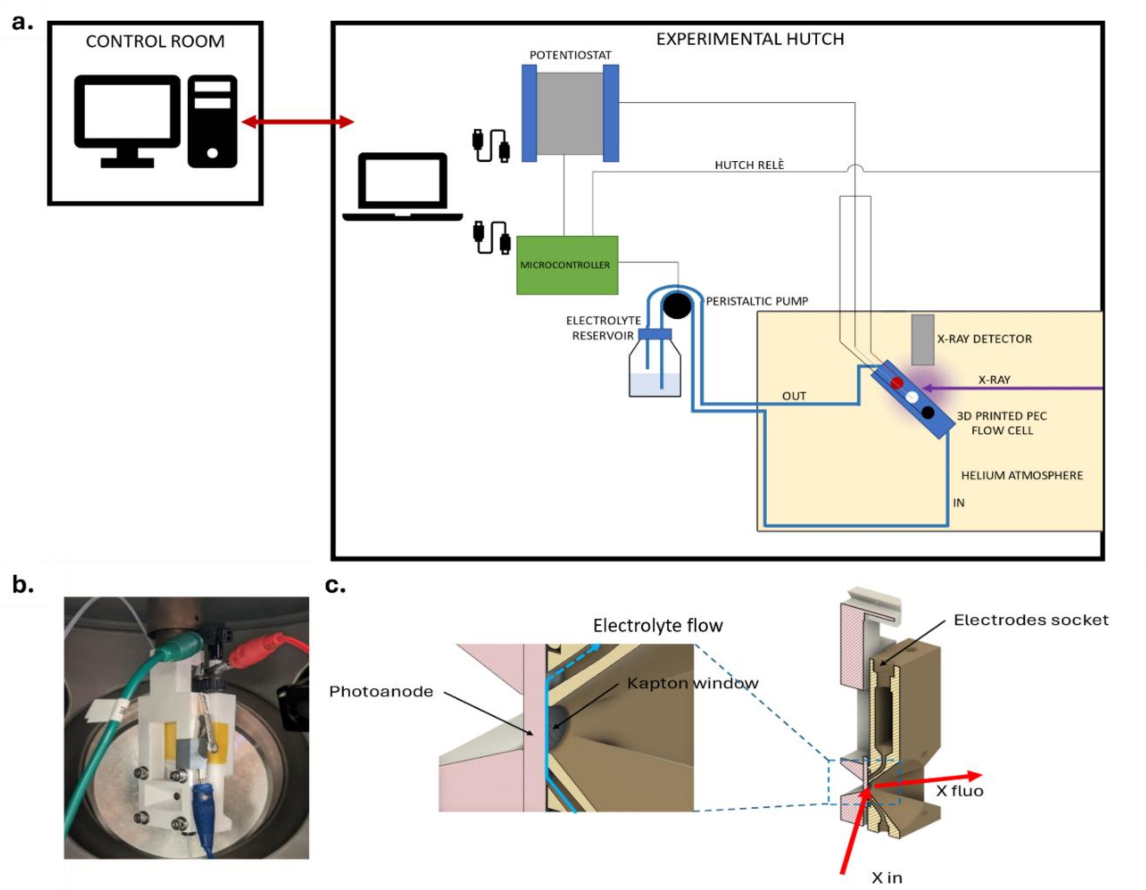

Figure 6.9 *Experimental setup developed for operando X-ray absorption measurements integrated with LISA beamline at ESRF, Grenoble.* ***(a)*** *Scheme of the experimental setup with all the main components: potentiostat, microcontroller for pulseless peristaltic pump, electrolyte reservoir and 3D printed cell.* ***(b)*** *Picture of the cell in the vacuum chamber,* ***(c)*** *Design of the cell left with cross-section of the cell.*

Fixed-Energy X-ray Absorption Voltammetry (FEXRAV) experiments were conducted to monitor the K-edge chemical shift of the target element in operando as a function of the applied potential[131]. The variation of the element-specific K fluorescence I_f, which is normalized to the incident photon flux and proportional to the X-ray absorption coefficient μ, was recorded while sweeping the potential. Measurements were taken at a fixed photon energy corresponding to the point of maximum derivative of the X-ray absorption coefficient with respect to energy. This approach optimizes sensitivity to chemical shifts that cause red- or blue-shifts in the X-ray absorption edge. Additionally, the negative derivative of I_f with respect to energy E, $-dI_f/dE$, or time $-dI_f/dt$ for a constant potential sweeping rate, was reported, providing an element-selective analogue of the current observed in cyclic voltammetry. More details on the experimental results can be found in *Chapter 9, Section 9.3*. These experiments were performed in the absence of light stimuli to prevent interference from photoinduced carriers, ensuring accurate assessment of the elemental state as a function of the applied potential. XANES spectra were also recorded at fixed potentials.

6.5 X-ray Photoelectron Spectroscopy (XPS)

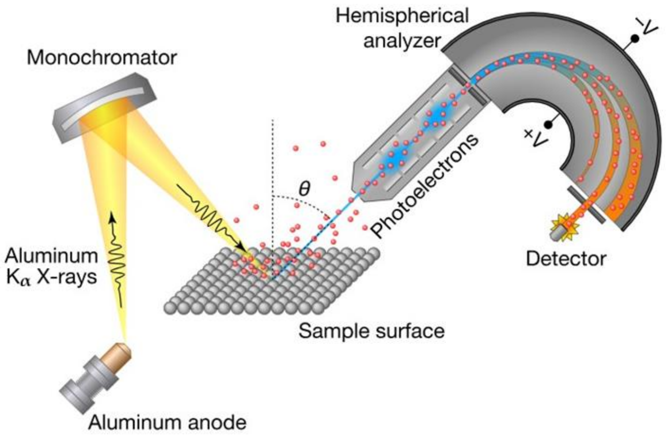

Figure 6.10 *Schematic representation of a typical X-ray photoelectron spectroscopy (XPS) setup.*

X-ray Photoelectron Spectroscopy (XPS) is a surface-sensitive, chemical specific, and quantitative technique used to investigate the chemical and physical properties of the materials. As shown in Figure 6.10, Aluminium K_α X-rays generated from an aluminium anode are directed through a monochromator onto the sample surface. The incident X-rays induce the emission of photoelectrons from the core levels of the sample. These core electrons, are shielded from the nuclear magnetic field, causing the breakdown of local symmetry and the loss of degeneracy. Consequently, electrons within the same orbital (j) occupy different energy levels, defined by $j = l + s$, and upon interaction with the X-ray radiation are ejected from the sample at different kinetic energies (KE). The photoemitted electrons are then collected at a specific angle (θ) and analysed by the Hemispherical Energy Analyser (HEA). To mitigate the multiplexing effect caused by the continuous emission of electrons from various energy levels, a passing energy (PE) is set at the beginning of the measurement and HEA applies a retarding potential (RP) that slows down incoming electrons, ensuring they reach the detector at different times. During the measurement, the software automatically calculates the retarding potential to be applied according to: $RP = KE - PE$ (6.13). This process allows for the filtering and separation of emitted particles. The retarding potential is also maintained along the semicircular trajectory just before the detector (Figure 6.10), ensuring precise energy analysis. The detector in XPS is typically a multichannel amplifier that counts the number of electrons arriving per second and converts it into a current. The current intensity, I_{el}, is influenced by several factors, including the number of incident photons, the cross-section and the sample's density, i.e., the density of scattering elements per unit volume. The surface sensitivity in XPS is described by the following relationship:

$$I_{el} \propto e^{-\frac{d}{\lambda}} \quad (6.14)$$

where λ is the electron's mean free path and d is the distance of the electron from the sample's surface. This *Equation 6.14*, analogous to the Lambert Beer law (*Equation 6.20*), indicates that I_{el} decreases exponentially with the electron's distance from the surface. It can be demonstrated that 63% of the detected I_{el} originates from a depth equal to $d = \lambda$, 32% from $d = 2\lambda$ and the remaining 5% from $d = 3\lambda$. Electrons originating from depths greater than 3λ are mostly elastically scattered, about 95% of them, and therefore do not reach the detector. To vary surface sensitivity in XPS, the mean free path λ can be modified, which is related to the electron's kinetic energy as illustrated in the following graph:

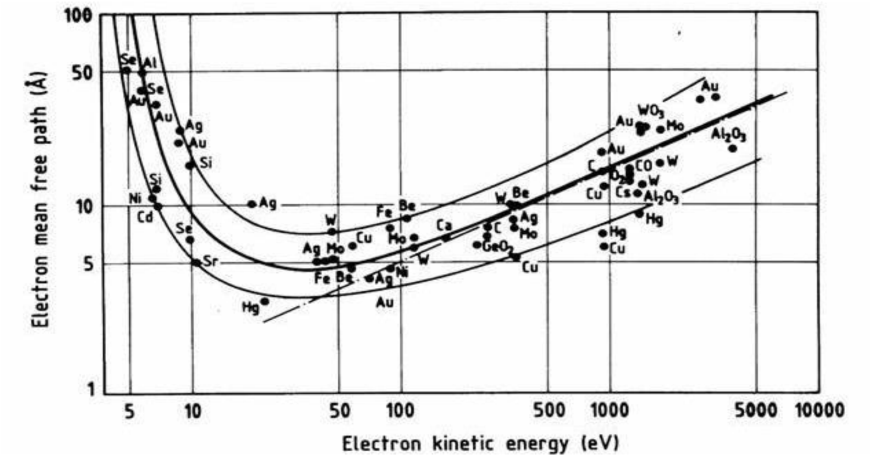

Figure 6.11 *The inelastic mean free path (λ) of electrons as a function of their kinetic energy for various elements. While λ depends strongly on the kinetic energy, it is only weakly dependent on the material: for this reason, the general trend $\lambda = \lambda\ (KE)$ is often referred to as universal curve. Image adapted from reference*[132].

In this work, X-Ray Photoelectron Spectroscopy (XPS) measurements utilized a SPECS Focus 500 monochromator and Phoibos 100 electron analyser, using Al Kα radiation at 1486.74 eV. The XPS spectra were measured in high vacuum at a 90° photoelectron take-off angle, and the angle between the X-ray source and the analyser was 54.7°. The high-resolution core level peaks were measured with a pass energy of 10 eV, in energy steps of 0.05 eV.

A typical XPS spectrum shows how the photoelectron intensity varies as a function of the kinetic energy (eV). Each element has its own XPS spectrum which serves as a distinct fingerprint, enabling an initial qualitative analysis of the sample under study. Figure 6.12 illustrates the energy levels involved in an XPS experiment. During an XPS measurement, three main steps can be identified: i) the photoemission of the electron from the core level, ii) the electron's propagation through the sample, iii) the diffusion of the photoemitted particle through the interface to reach the detector. During this travel, both the semiconductor and the instrument's work functions, φ_{S} and φ_{HEA}, respectively, come into play and influence the value of KE (and thus of BE) of the photoemitted electron.

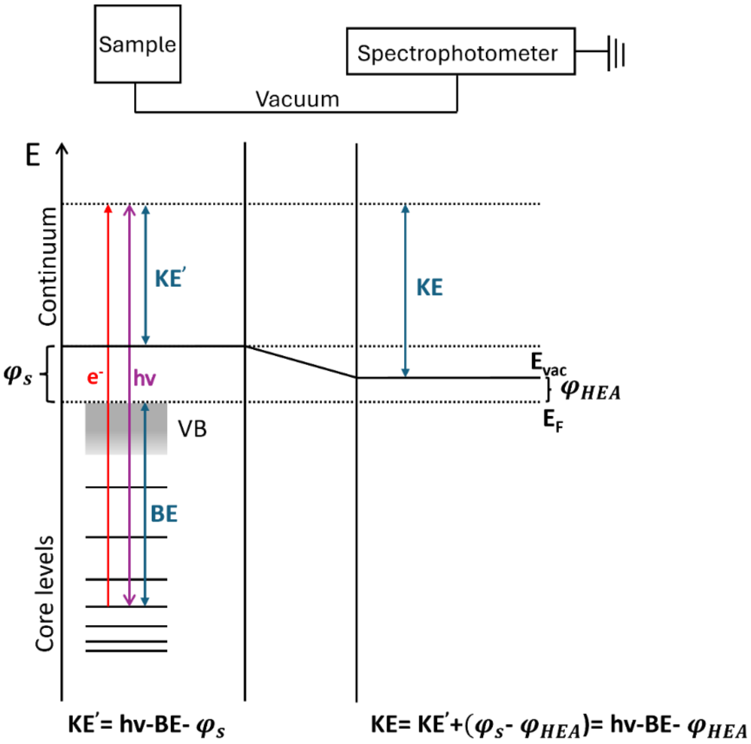

Figure 6.12 *Diagram of the energy levels involved in an XPS experiment.*

KE can be converted into binding energy (BE) by using the Einstein relation:

$$hv = BE + KE + \varphi_{HEA} \quad (6.15)$$

where hv is the energy of the incident radiation and φ_{HEA} is the work function of the instrument that is kept fixed during the experiment. BE is an intrinsic property of the material indicating the strength of the bind between the core electron and the nucleus. In semiconductors, as in the case of this study, it defines the energy difference between the Fermi level and the level occupied by the photoemitted electron (Figure 6.12). The value of BE is therefore indicative of the orbital from which the core electron is emitted and gives information about the oxidation state of the analysed element. Chemical shifts of binding energy peaks are caused by its surrounding chemical environment. When an atom bonds with a more electronegative atom, it becomes slightly positively charged, leading to an increase in the binding energy of its remaining electrons. To accurately identify the chemical environment of individual elements, detailed spectral fitting is often performed, which is essential for correctly interpreting the peaks.

The area under the peaks defines the cross section, σ, which is the probability that the core electron interacts with the incoming photon producing the photoemission from that specific orbital. σ can be determined by the Fermi Golden rule according to:

$$\sigma \propto \frac{1}{2\hbar}\left|\langle f|\hat{H}|i\rangle\right|^2 \quad (6.16)$$

where $\hbar$ is the Planck constant (6.62607015×10^{-34} J·s), $\hat{H}$ is the Hamiltonian operator representing the energy exchanged between photon and matter, $\langle f|$ and $|i\rangle$ are, respectively, the final and initial states involved in the electronic transition.

Additional valuable information can be obtained from XPS spectrum, including the semiconductor's work function, φ_S, from the secondary electron cut-off at high binding energies, and the Valance Band maximum ($\mathrm{VB_{max}}$) at low binding energies. While the conduction band minimum ($\mathrm{CB_{min}}$) cannot be directly determined from the XPS spectrum, complementary technique can be employed to identify it. By combining these methods, a comprehensive band diagram of the semiconducting material can be reconstructed.

6.6 Spectro-photometry

When an exciting monochromatic radiation reaches the sample, its intensity is modulated by the interactions with the chemical species present in it. Molecules are promoted from the ground to electronically excited states, giving rise to electronic transitions dependent on the energy of the incoming radiation and on the chemical nature of the species involved. Consequently, absorption bands arise that are specific to the sample under study.

The transmittance (T) is defined as the fraction of light coming out from the sample:

$$T = \frac{I}{I_0} \ (6.17)$$

where I is the intensity of the transmitted radiation and I_0 is the intensity of the incident light. The transmitted intensity, I, can be reduced by scattering events caused by small, suspended particles which prevent the incident light from being absorbed by the desired chemical species.

From the transmittance, the absorbance (A) is determined according to:

$$A = -log_{10}T \ \ (6.18)$$

This dimensionless quantity can also be calculated using an empirical equation named as Lambert-Beer Law:

$$A = \varepsilon bc \ (6.19)$$

where ε is the molar absorption coefficient at a specific wavelength ($M^{-1}cm^{-1}$), b is the length of the cell's optical path (cm) and c is the concentration of the chemical species (M). Gathering *Equations 6.17* and *6.18*, the Lambert Berr law can also be written as: $I = I_0e^{-\varepsilon bc}$ (6.20).

To apply the Lambert Beer law in our experimental studies, it is important to maintain linearity so that $0.1 < A < 2$. This can be done either by adjusting the sample's concentration or the length of the optical path. Additionally, both the solvent and the sample holder, i.e. the cuvette, must be transparent to the wavelength-range used for excitation. In this thesis, UV-visible absorbance spectra were recorded with a Perkin Elmer λ650 spectrophotometer, using quartz cells with a 1.0 cm path length. The estimated experimental error is 5% on the molar absorption coefficients.

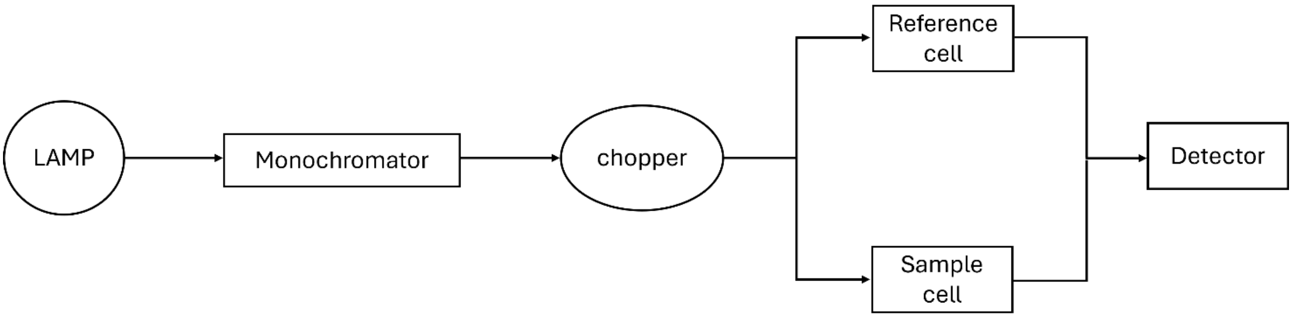

Figure 6.13 *Block diagram of a double-beam spectrophotometer.*

Figure 6.13 depicts the block diagram of a double-beam spectrophotometer. The excitation lamp is a polychromatic light source, usually composed of a deuterium arc lamp emitting light in the range of 190-320 nm and a tungsten lamp covering the range of 320-900 nm. The monochromator is a grating equipped with slits that reflects the incident light at different angles, depending on the wavelength. The advantage of this configuration over a single beam one, is that it enables to measure the radiation intensity transmitted both by the sample and by the reference cell simultaneously. This is done thanks to the presence of the chopper, a rotating mirror with alternating reflecting and transparent slices, that enables the splitting of the incident light sending it to both the sample and the reference cells. In this way, the reference cell's absorbance can be subtracted from the sample's cell absorbance, obtaining a value independent from instrumental and environmental fluctuations. In the end, the transmitted light is captured by the detector, normally a photomultiplier tube, that does the subtraction and generates the final absorption spectrum.

6.7 Spectro-fluorimetry[133]

Spectro-fluorimetry is an exceptionally sensitive and versatile technique for investigating luminescence phenomena. When a sample is excited, the chemical species can return to the ground state thermally, by realising heat, or radiatively, by emitting a photon. In the latter case, two types of luminescence can occur: fluorescence if the process is spin allowed, i.e., the excited state as the same spin multiplicity as the ground state, or phosphorescence, when the process is spin forbidden. Collecting emission or excitation spectra offers valuable insights into the nature of the chemical species and the positioning of their excited states within the energy level structure.

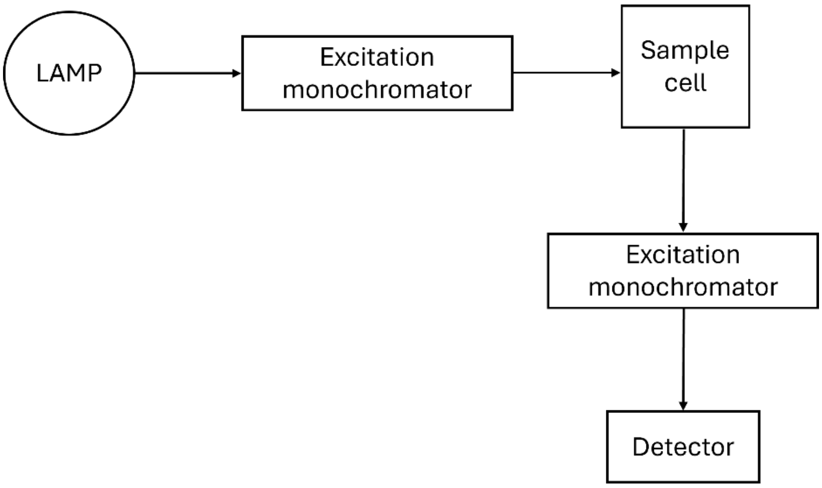

Figure 6.14 *Block diagram of a spectrofluorometer.*

The block diagram of a typical spectrofluorometer is shown in Figure 6.14. It usually includes a Xenon lamp, covering the 250-1000 nm range, an excitation and an emission monochromator, a sample holder and a detector. In this work, emission and excitation spectra were recorded using an Edinburgh FS5 spectrofluorometer equipped with a PMT980 and an InGaAs detector for the visible and near-infrared (NIR) spectral ranges, respectively.

The electrical signal from the detector is not compared to a blank and can vary significantly between instruments. To address these variations and to eliminate dependence on instrumental factors, corrections are applied by considering the lamp's emission spectrum and the instrument's geometry. Although this is done automatically by the instrument, a regular verification is essential to maintain accuracy as they can become outdated overtime.

To minimize the collection of excitation light, the detector is typically positioned at a 90° angle to the excitation beam. However, scattering from dust and molecules in the sample can still cause a small portion of excitation light to reach the detector, resulting in unwanted signals such as Rayleigh-Tyndall scattering, Raman bands, and higher-order harmonics, which need to be accounted during the acquisition of the spectra.

As anticipated, the spectrofluorometer can be used to acquire either steady-state emission or excitation spectra. For emission spectra, the excitation monochromator is fixed at a specific wavelength, λ_{exc}, determined from the absorption spectrum of the species, while the emission monochromator scans the selected range of wavelengths. The resulting emission spectrum shows how the emission intensity varies with the wavelength, when excited at λ_{exc}. For excitation spectra, the excitation monochromator scans a selected range of wavelengths where the sample absorbs, while the emission monochromator is fixed at a specific emission wavelength, λ_{em}, that is usually where the species exhibits its maximum emission intensity. If the absorbance of the species is below 0.1, across the selected excitation range, the excitation spectrum will closely resemble the absorption spectrum. Indeed, under these conditions and with appropriate corrections, the signal at each excitation wavelength will be directly proportional to the probability of populating the excited state responsible for the emission at λ_{em}.

6.8 High-Performance Liquid Chromatography (HPLC)

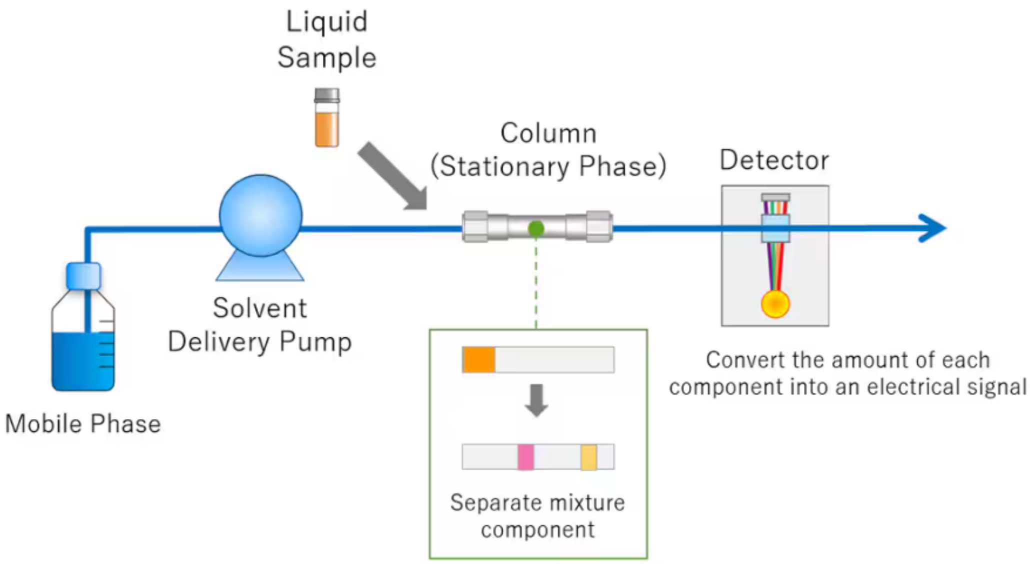

Figure 6.15 *Schematic of the functioning of an HPLC instrumentation.*

High-Performance Liquid Chromatography (HPLC) is a highly accurate analytical technique used to analyse, separate, and identify different components in a mixture. As shown in Figure 6.15, in this method a liquid mobile phase passes through a column packed with a stationary phase under high pressure. When a sample is introduced, its components interact differently with the stationary and mobile phases, resulting in their separation. These components exit the column at distinct times, referred to as retention times, which allows for their individual detection. Common detectors used in HPLC include UV-Vis spectrophotometers and mass spectrometers.

In this thesis, HPLC was utilized to identify and quantify the products obtained from PEC conversions. This was achieved by using calibration curves generated from the chromatographic peaks of standard solutions of the starting compounds and their oxidative derivatives. From the area under the chromatographic peaks, the moles of species involved in the redox process were calculated. In addition to the Faradaic Efficiency (as described in *Equation 6.1*), the relative selectivity ($S_{\%}$) or relative conversion coefficient as defined in *Chapter 9*, was calculated using the following formula:

$$S_{\%} = 100 \times \frac{nmol_i}{nmol_{tot}} \quad (6.21)$$

where $nmol_i$ refers to the moles of the product i, and nmol_{tot} results from the sum of moles of all the products.

For the HMF PEC conversion experiments, an Agilent Technologies 1100 series HPLC system equipped with a UV-Vis diode-array detector (DAD) was used, operating with isocratic elution. The mobile phase consisted of an aqueous solution of 5 mM ammonium acetate and methanol in a 7:3 ratio. Separation was achieved using a 25 cm reverse-phase Luna Omega C-18 column, with a flow rate of 0.5 mL/min. A sample volume of 2 µL, diluted 10 times in the eluent, was injected. Calibration curves were generated based on the chromatographic peaks (detected at 254 nm) using standard solutions of known concentrations (0.01 to 1 mM). The retention times were: FDCA at 4.17 min, FFCA at 5.35 min, HMF at 8.36 min, and DFF at 9.64 min.

For GOR experiments, HPLC analysis was performed using a Thermo Scientific UltiMate 3000 system. Separation was carried out using a HyperREZ XP H+ column (Thermo Scientific) with two detectors: a UV detector with variable wavelength (UltiMate 3000) and a refractive index (RI) detector (RefractoMax 520). The mobile phase was a 5 mM aqueous H_2SO_4 solution, with a flow rate of 0.5 mL/min, and the column temperature was maintained at 60°C. Details regarding the calibration method are reported in the work of Kong et al[134].

7. Preparation of photoanodic materials for solar energy conversion

7.1 $BiVO_4$ photoanodes

During my research visit at the Helmholtz Zentrum Berlin–Institute of Solar Fuels, nanoporous $BiVO_4$ photoanodes were synthesized via electrodeposition, following the method of Choi et al.[52] In summary, BiOI was first electrodeposited onto an FTO substrate using a mixed solution consisting of: i) an aqueous acidic solution containing KI and $Bi(NO_3)_3{\cdot}5H_2O$, and ii) an ethanol solution with p-benzoquinone. The BiOI was then converted to $BiVO_4$ through an annealing process, using a vanadium acetylacetonate solution in dimethyl sulfoxide (V/DMSO). The BiOI samples were placed in a furnace, with a few drops of the V/DMSO solution applied to each. Annealing was conducted at 450°C for two hours, with gradual ramping of temperature before and after the process. Finally, excess of V_2O_5 was removed by immersing the annealed sample in 1M NaOH aqueous solution.

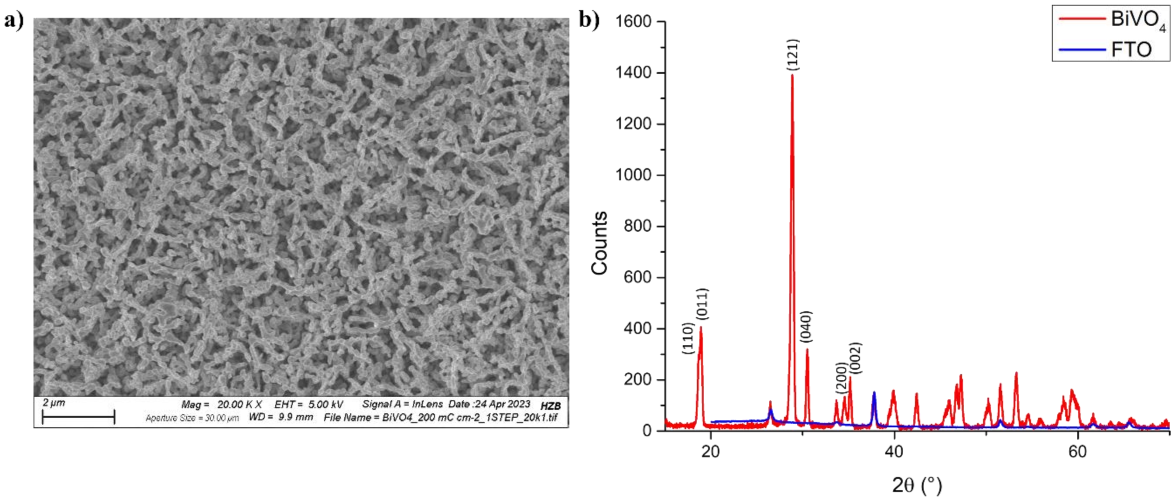

Figure 7.1 ***(a)*** *Planar image of a $BiVO_4$ photoanode morphology by SEM analysis;* ***(b)*** *XRD pattern of the BiVO4 film and FTO substrate.*

7.2 $Ti{:}Fe_2O_3$ photoanodes

The photoanodes were produced at the Department of Chemistry, University of Ferrara, as part of the H2020 project CONDOR: COmbined suN-Driven Oxidation and CO2 Reduction for Renewable Energy Storage. Their fabrication and structural characterization were achieved by adapting and integrating various previously reported synthetic approaches[135][136]. Ti(IV)-modified nanostructured hematite photoanodes ($Ti{:}Fe_2O_3$) were prepared on a fluorine doped SnO_2 (FTO) conductive glass by a hydrothermal approach. Briefly, the FTO glass was cleaned through ultrasonication in isopropanol, and then rinsed with deionized water. The fabrication of hematite nano-rod electrodes involves the deposition of a Ti(IV) modified iron oxide seed layer by dip coating (0.625 mm/s) the cleaned 2 mm thick FTO/glass slides (10 mm (wide) x 25 mm (long)) in a Fe(III) oleate precursor containing 15 mM Titanium(IV) isopropoxide in order to obtain a 10 mm x 10 mm coated area. The dip coating solution was prepared following the procedure described by D. K. Bora[136]. The Fe(III)oleate layer was converted into hematite following a 30 minute heat treatment at 500 °C. Solvothermal synthesis was carried out in a teflon-lined stainless steel autoclave by using an aqueous precursor containing 0.91 M sodium nitrate ($NaNO_3$, Carlo Erba Reagents), at a pH value of 1.5 adjusted with 6 M HCl, 0.136 M of ferric chloride ($FeCl_3 \cdot 6 H2O$, Alfa Aesar), 2.5 mM Ti_2CN (Sigma-Aldrich) and a 5 % (v/v) ethanol (Carlo Erba Reagents)[137]. The seed-layered electrodes were inserted into the autoclave, lying at an angle of ca. 45° with respect to the vertical liner walls. Heating at 95 °C was applied for 4 h. A uniform layer of yellowish colour film (FeOOH) was formed on the electrodes. The FeOOH-coated substrates were washed with deionized water to remove weakly interacting residues from the hydrothermal bath before sintering in air at 550 °C for 1 h, during which conversion of FeOOH to Fe_2O_3 occurred. Finally, the resulting hematite thin films were modified by chemical bath treatment in a 0.2 M $TiCl_4$ solution heated at 50 °C for 1 hour, followed by a final thermal annealing at 760 °C for 10 minutes affording the $Ti:Fe_2O_3$ electrodes.

Pristine $Ti:Fe_2O_3$ photoanodes display a homogeneous micro structure characterized by thin film islands with a lateral width of 2–5µm, separated by thermal stress-induced cracks in the film resulting from the fast thermal annealing process.

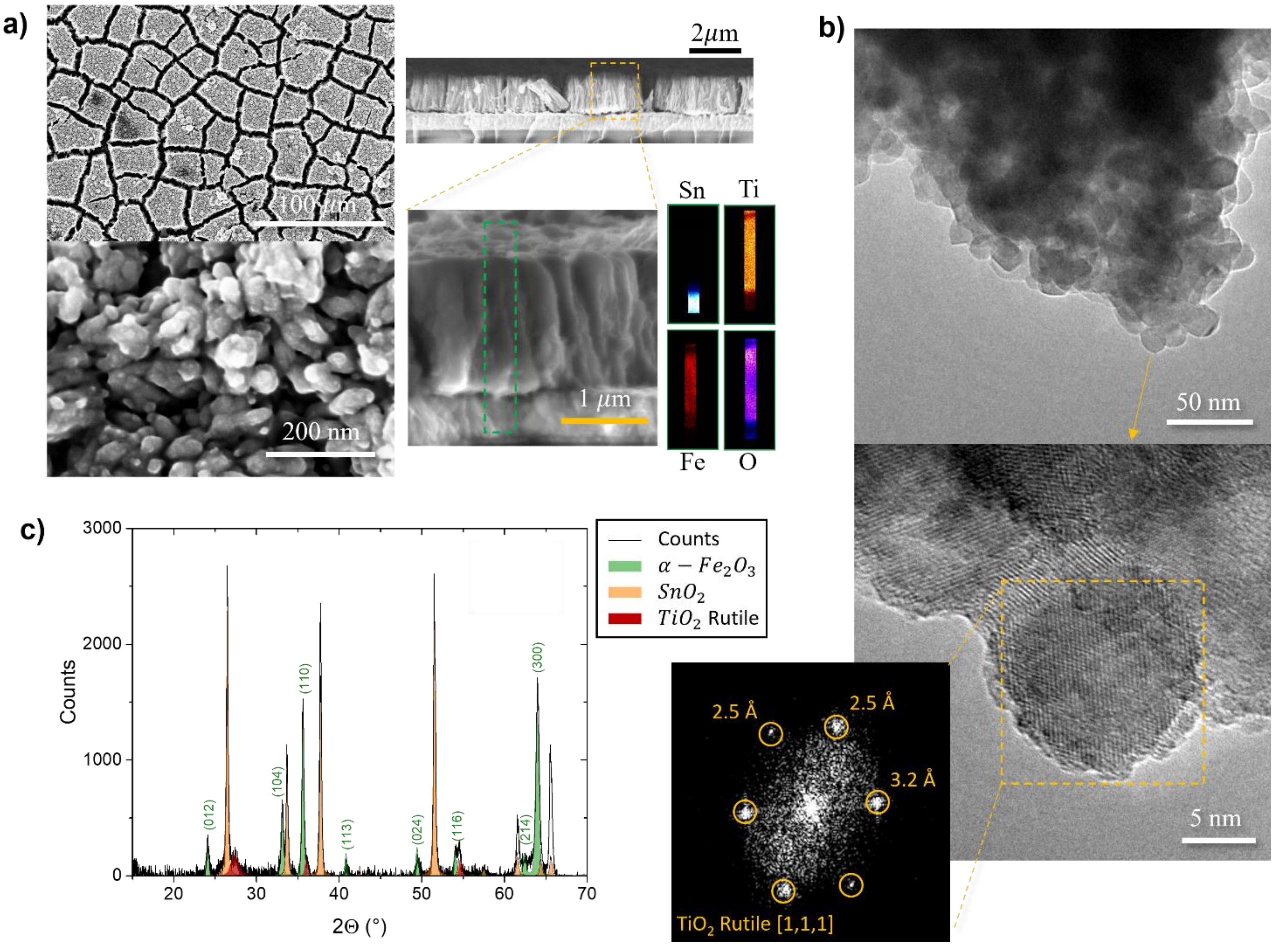

Figure 7.2 ***(a)*** *Planar (left) and cross-section (right) characterization of a Ti:Fe_2O_3 photoanode morphology and composition by SEM and EDS analysis;* ***(b)*** *HR-TEM analysis of the same photoanode and resulting FFT in the inset;* ***(c)*** *XRD analysis after background subtraction, with the corresponding hematite main indexed peaks.*

As displayed by scanning electron microscopy (SEM) analysis (Figure 7.2a), the islands are composed of sintered nanoparticles with a diameter in the 20–30nm range. The cross-sectional view of the Ti:Fe_2O_3 thin film shows columnar structures with a uniform thickness in the range 1.5–1.7μm. Energy dispersive spectrometry (EDS) analysis clearly displays the homogeneous distribution of Fe and O on the underlying tin oxide film, as well as the presence of titanium throughout the entire hematite film thickness, with an increase at the very surface of the electrode. This is compatible with a certain degree of porosity of the structure, allowing for the penetration of the Ti(IV) precursor within the hematite layer. High-temperature annealing promotes Ti(IV) diffusion into the hematite lattice and leads to the formation of cracks in the thick hematite layer, potentially enhancing the PEC activity by increasing the surface area exposed to the electrolyte.

High-resolution transmission electron microscopy (HR-TEM) analysis (Figure 7.2b) further reveals the presence of crystalline nanoparticles smaller than 10 nm, with a lattice structure consistent with rutile TiO_2. This observation is supported by X-ray diffraction (XRD) analysis (Figure 7.2c), which, in addition to identifying the Bragg reflections of hematite and FTO, shows broad peaks indicative of a rutile phase, confirming the ultrafine size of the crystallites. The presence of rutile is expected given the high Ti content (Ti/Fe = 15 at%) determined by SEM analysis (Figure 7.3a). At the nanoscale, rutile and hematite phases are finely intermixed, with local EDS analysis consistently detecting both elements across different sample regions (Figure 7.3b).

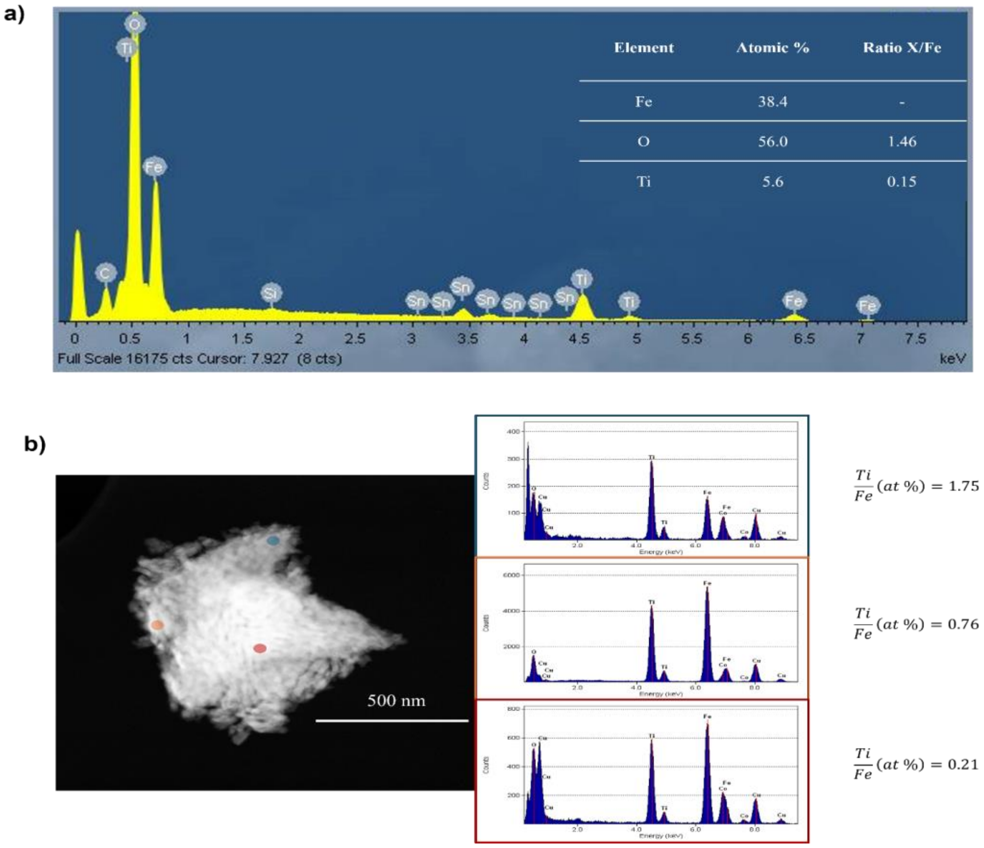

Element	Atomic %	Ratio X/Fe
Fe	38.4	-
O	56.0	1.46
Ti	5.6	0.15

Figure 7.3 (a) *Wide area EDS spectrum of a Ti:*Fe_2O_3 *photoanode.* ***(b)*** *STEM-HAADF micrograph of a Ti:*Fe_2O_3 *microparticle and EDS spectra collected in the highlighted regions of the sample.*

The near-surface regions are significantly enriched in Ti, while the inner regions have a composition closer to the average value. Given the low solubility limit of Fe in TiO_2 (1 at%), the detection of substantial Fe in the rutile-rich surface areas suggests the presence of mixed Fe-Ti oxides, possibly resembling ilmenite ($FeTiO_3$) or pseudo-brookite (Fe_2TiO_5). These phases are challenging to detect by XRD and HR-TEM due to poor crystallinity and lattice spacings close to hematite but have been reported in previous studies carried out by X-ray absorption spectroscopy, a probe sensitive to the local environment[69]. This complex structure results in a significant improvement of the photocurrent characteristics typically exhibited by pristine Fe_2O_3 photoanodes (Figure 7.4).

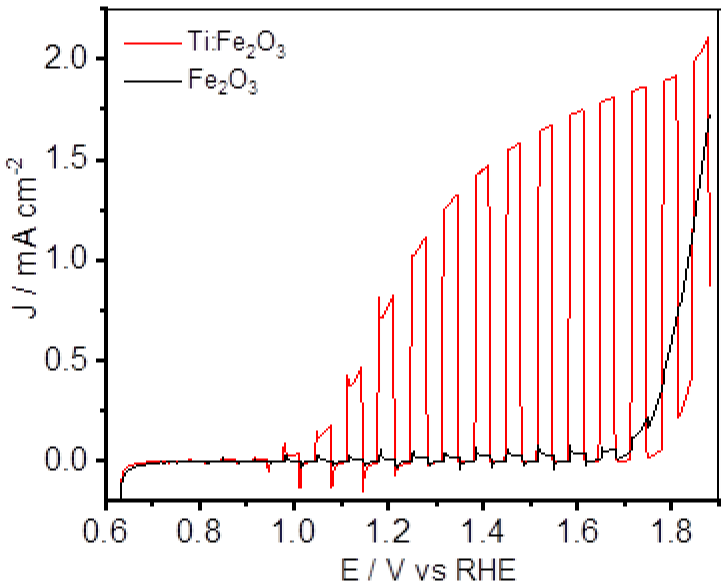

***Figure 7.4** Chopped LSVs comparison between pristine Fe_2O_3 and Ti:Fe_2O_3, acquired in a KOH (0.1 M, pH 13.3) solution.*

7.2.1. Co-catalysts modification

7.2.1.1 Cobalt-based co-catalysts

The deposition of Cobalt Phosphate (referred to as CoPi) on hematite electrodes using the electrodeposition method was according to directions from by Kanan and Nocera[138]. Briefly, deposition was performed in a three electrode cell containing a solution of 0.5 mM cobalt(II) nitrate ($Co(NO_3)_2 \cdot 6H_2O$) and potassium phosphate (0.1 M KH_2PO_4 at pH 7.0) using a SCE as reference electrode, hematite as working and a Pt foil as counter electrode. CoPi was electrodeposited applying the potential at which we recorded 0.322 mA·cm^{-2} during a dark linear sweep voltammetry. The desired current values are usually recorded at around 1.1V vs SCE. In order to obtain a thick CoPi layer over the hematite film, the potentiostatic electrolysis was carried out for ca. 30 minutes corresponding to ca. 530 mC·cm^{-2} of passed charge.

$CoFeO_x$ deposition was accomplished by adapting a previous method outlined by Liardet et al.[139]. An aqueous solution containing 1.6 mM cobalt(II) chloride ($CoCl_2 \cdot 6\ H_2O$) and 0.5 mM iron(III) sulphate ($Fe_2(SO_4)_3 \cdot 5\ H_2O$) was prepared in 0.1 M sodium acetate (CH_3COONa). The hematite substrate was immersed in the as-prepared solution and the deposition of $CoFeO_x$ was performed by 10s chronoamperometry at 600mV vs SCE, by back illuminating the hematite electrodes under AM 1.5G conditions. SCE was the reference electrode, and a Pt foil was used as the counter electrode. The total amount of charge passed during the photo-electrodeposition was about 4 mC·cm^{-2}.

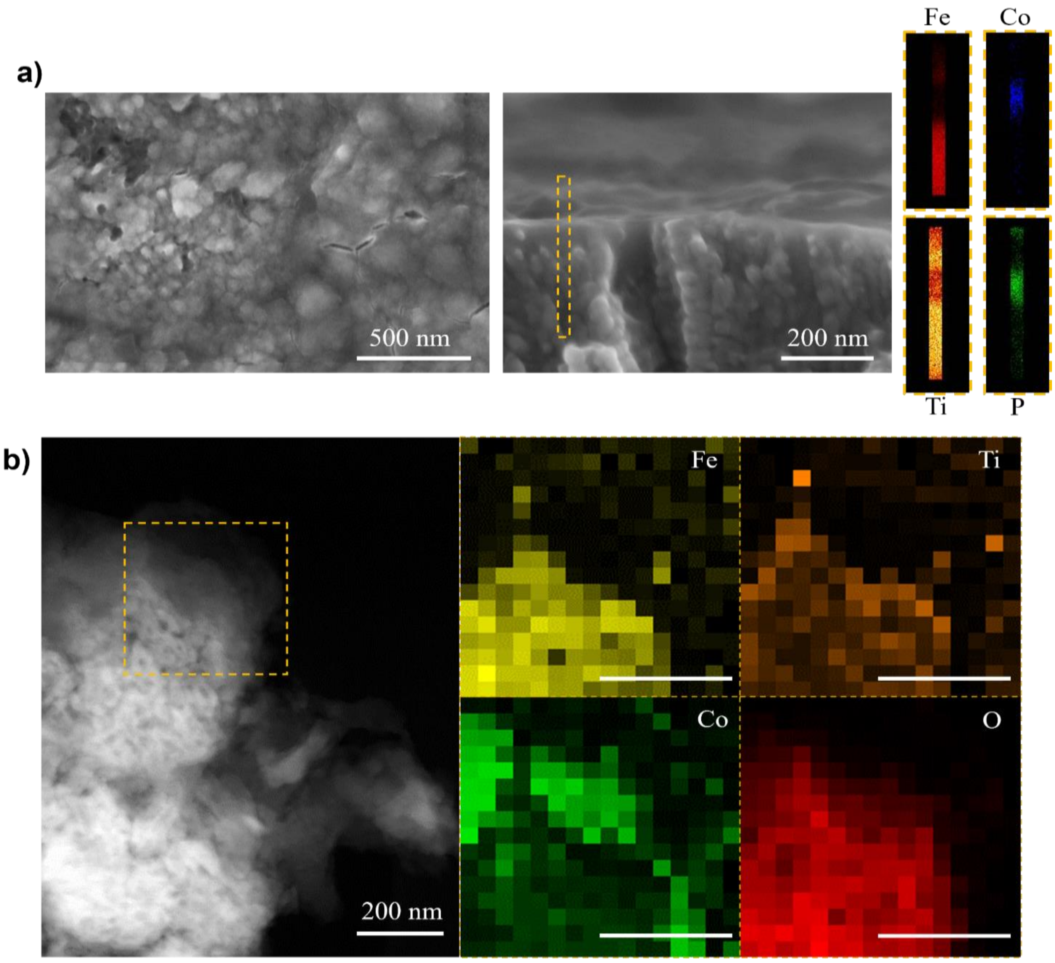

Figure 7.5 ***(a)*** *Planar (left) and cross-section (right) characterization of a Ti:Fe_2O_3-CoPi photoanode morphology and composition by SEM and EDS analysis;* ***(b)*** *STEM micrograph of a detail of the same photoanode and resulting EDS mapping of main representative elements, highlighting the localization of Co-related signal on the surface of the hematite structures.*

The light harvesting properties of the Ti:Fe_2O_3 photoanodes are only slightly affected by the overlayer deposition (Figure 7.6).

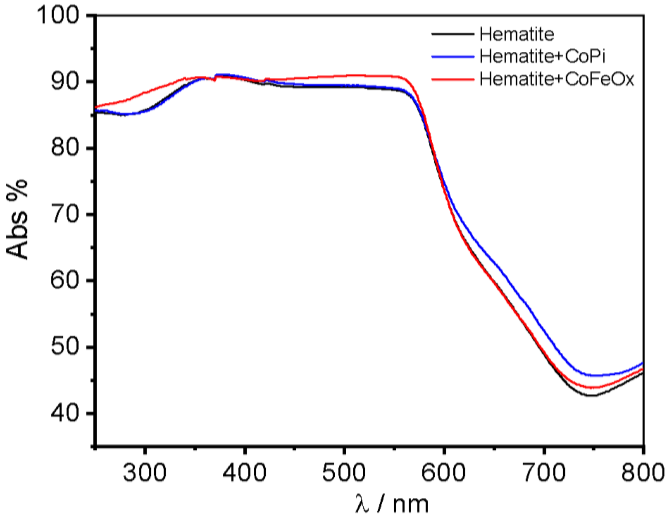

Figure 7.6 *Absorption spectrum of Ti:Fe_2O_3, Ti:Fe_2O_3-CoPi and Ti:Fe_2O_3-$CoFeO_x$.*

Pristine Ti:Fe_2O_3 samples are displaying almost unitary absorptivity at wavelength <590nm, consistent with the expected bandgap, while some apparent residual absorption is observed at longer wavelengths, presumably due to scattering from the rough, nanostructured surface. The addition of $CoFeO_x$ results in an almost negligible increase of absorptivity in the low-wavelength region, where, given the high absorbance values, large uncertainty is expected. On the other hand, the CoPi layer slightly increases the absorptivity in the sub-gap region of the spectrum, but the monotonic trend suggests that the contribution is mainly related to scattering rather than absorption.

7.2.1.2 Nickel-based co-catalysts

$Ni(OH)_2$ film was electrodeposited on Ti:Fe_2O_3 photoanode following the method described by Bender et al.[140]. The deposition was carried out in a 50 mM $Ni(NO_3)_2 \cdot 6\,H_2O$ solution, maintaining a current density of -0.25 mA/cm^2 for 12 minutes.

NiMo catalyst layer was deposited by DC magnetron sputtering using a 2 inches NiMo target (EVOCHEM ADVANCED MATERIALS) composed of 80:20 at% Ni to Mo. The sputtering process began at a chamber pressure of $5x10^{-7}$ mbar, which increased to $8x10^{-3}$ mbar upon the introduction of 10 sccm of Ar gas. Sputtering was performed for 20 minutes at 20 W, with the film thickness calibrated beforehand, resulting in an estimated thickness of 32 nm.

8. TEMPO-mediated HMF photoelectrochemical oxidation to FDCA with Ti:Fe_2O_3 photoanodes modified with Co-based co-catalysts

This section investigates the photoelectrochemical activity of Ti:Fe_2O_3 photoanodes for the TEMPO-mediated oxidation of HMF to FDCA. The conversion was carried out under mildly basic aqueous conditions (borate buffer, pH 9.2) to prevent HMF degradation. The selectivity and Faradaic efficiency of the PEC process were fine-tuned by modifying the photoelectrode surface with cobalt-based co-catalyst films, specifically CoPi and $CoFeO_x$ (more details on the preparations can be found in *Chapter 7*, *Section 7.2*). These co-catalysts were chosen to explore their different roles in competing biomass and water oxidation reactions, comparing the performance of a highly efficient OER catalyst—a thin CoFeOx layer[141]—against a less effective, thicker (~100 nm) CoPi layer, which is known to negatively affect the charge transfer properties of hematite photoanodes[142]. Charge mobility properties of Ti:Fe_2O_3 photoanodes were analysed using Intensity Modulated Photocurrent Spectroscopy (IMPS) and Electrochemical Impedance Spectroscopy (EIS) and compared to those of the co-catalyst-modified photoelectrodes. A newly developed algorithm for IMPS data analysis, based on Distribution of Relaxation Times (DRT)[127], was applied for the first time to correlate charge carrier dynamics at the semiconductor/electrolyte interface with reaction selectivity.

8.1 PEC-OER characteristics of co-catalyst-modified Ti:Fe_2O_3 photoanodes

Preliminary characterization of the photoelectrode performance was carried out in a two-compartments PEC cell to determine the activity towards OER. Chopped LSVs (Figure 8.1) showed that the addition of a co-catalyst results in a decrease of the onset photopotential. However, while the $CoFeO_x$ overlayer produces slightly increased photocurrent, CoPi gives the opposite effect. The limiting photocurrent density is decreased by ~0.4mA cm^{-2} at 1.6V vs RHE, suggesting that the thick CoPi overlayer partially reduces the photoelectrochemical OER rate.

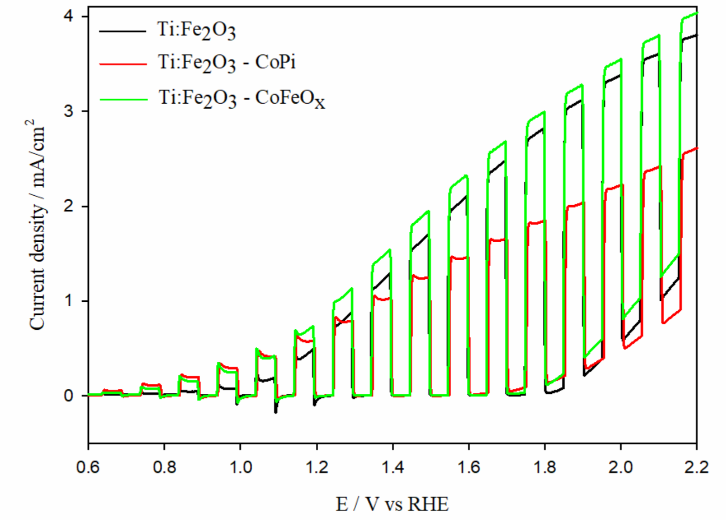

Figure 8.1 *Chopped LSVs for the three electrodes: Ti:*Fe_2O_3 *(black line), Ti:*Fe_2O_3*-CoPi (red line) and Ti:*Fe_2O_3*-CoFe*O_x *(green line).*

The stability of the photoanodes under long irradiation periods was assessed, by recording LSVs before and after pulsed chrono-coulometries of 37 hours (at 1.6V vs RHE): the current/voltage characteristics were very similar in shape and the response of the photoelectrodes was substantially preserved, so that it was possible to use these photoanodes several times, with no loss in terms of performance. The electrochemically active surface area (ECSA) was evaluated by following the previously reported approach[143], based on the determination of the anode double layer capacitance (C_{dl}) from the electrochemical impedance spectrum at E_{OCP} (Figure 8.2). C_{dl} is equal to 0.112 mF cm^{-2} for pristine Ti:Fe_2O_3 and a similar value (0.100 mF cm^{-2}) is obtained for the Ti:Fe_2O_3-CoFeO_x sample. A non-negligible drop to 0.076 mF cm^{-2} is observed for Ti:Fe_2O_3-CoPi, pointing out a partial surface passivation. This contributes explaining the lower limiting photocurrents observed when Ti:Fe_2O_3 is covered by a thick CoPi overlayer.

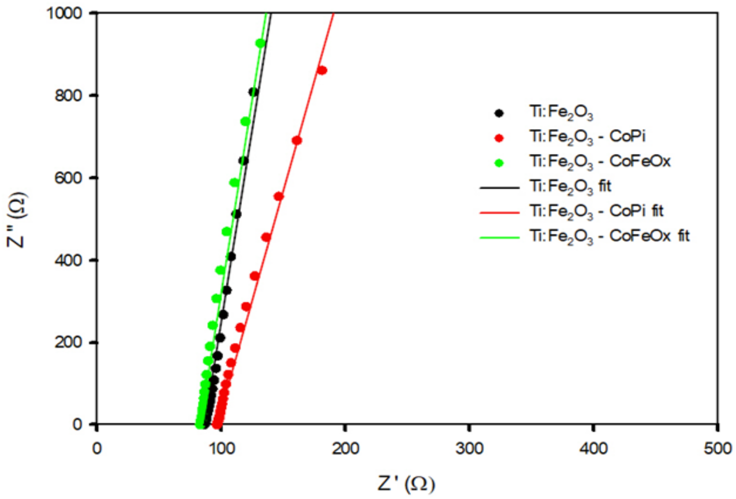

Figure 8.2 *Electrochemical Impedance Spectroscopy (EIS) in dark at* E_{OCP}*, for Ti:*Fe_2O_3*, Ti:*Fe_2O_3*-CoPi and Ti:*Fe_2O_3*-CoFe*O_x*.*

8.2 TEMPO-mediated photoelectrochemical HMF conversion

The investigation of the PEC activity towards HMF oxidation was performed using the same experimental setup, with TEMPO as electron-mediator. The HMF and TEMPO concentration were 2.5 mM and 6.5 mM, respectively.

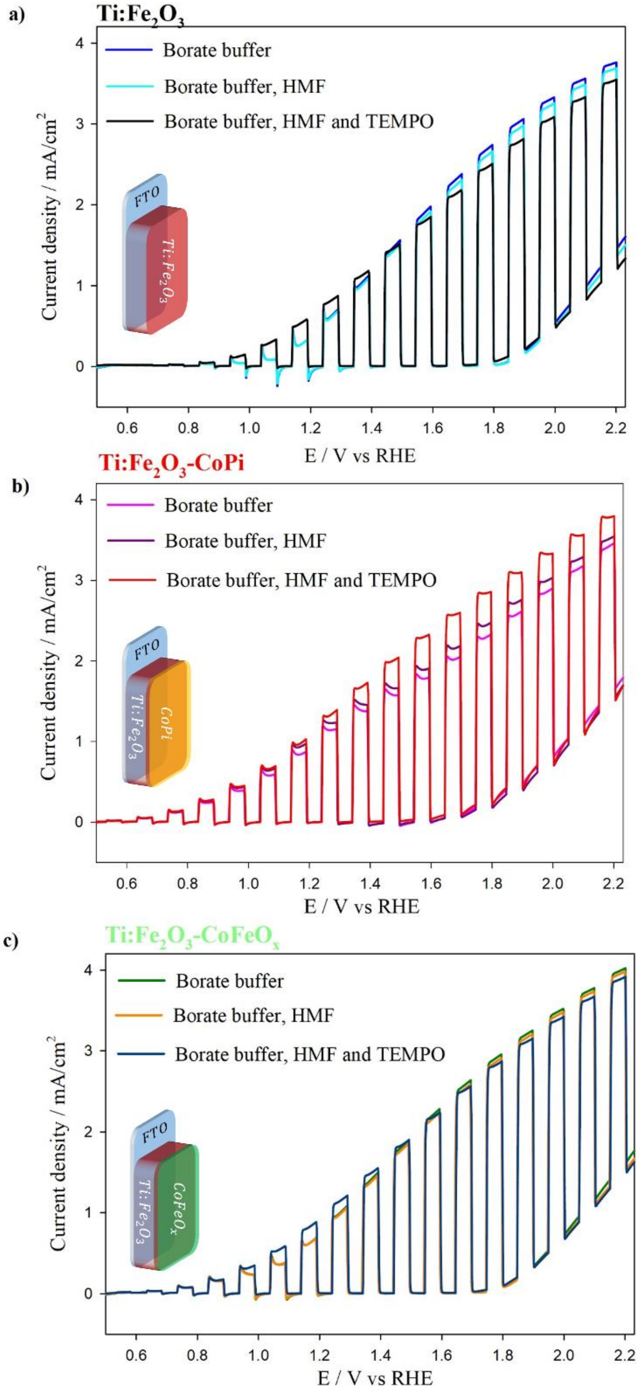

Figure 8.3 (a) *Chopped LSVs of a Ti:Fe_2O_3,* ***(b)*** *Ti:Fe_2O_3-CoPi and* ***(c)*** *Ti:Fe_2O_3-$CoFeO_x$ overlaid to those displayed upon the addition of HMF, or in the presence of both HMF and TEMPO.*

For all samples, almost no alteration of the chopped LSVs can be appreciated upon addition of HMF in the electrolyte solution. In the presence of TEMPO and HMF, the onset photopotentials for

$Ti:Fe_2O_3$ and $Ti:Fe_2O_3$-$CoFeO_x$ photoanodes are anticipated and the recombination spikes are reduced, whereas $Ti:Fe_2O_3$-CoPi is barely affected by its addition, since the photocurrent onset is already more cathodic in pure electrolyte.

The performance of each electrode in HMF photoconversion was assessed through long-term pulsed chrono-coulometry. The periodic polarization of Ti-hematite electrodes at OCP was beneficial for the stability of the electrode response, helping to regenerate the electrode surface from oxidizing intermediates, such as peroxides, upon positive polarization. To limit the reaction time, the experiment was performed at 1.6V vs RHE.

The reaction progress was monitored by collecting solution samples at specific intervals corresponding to charge accumulations representing 0%, 100%, 150%, and 200% of the theoretical HMF conversion, based on the 6-electron oxidation to FDCA (*Chapter 4*, Figure 4.4). For clarity, these charge values are referred to as $Q_{100\%}$, $Q_{150\%}$, and $Q_{200\%}$. The collected samples were then analysed using HPLC.

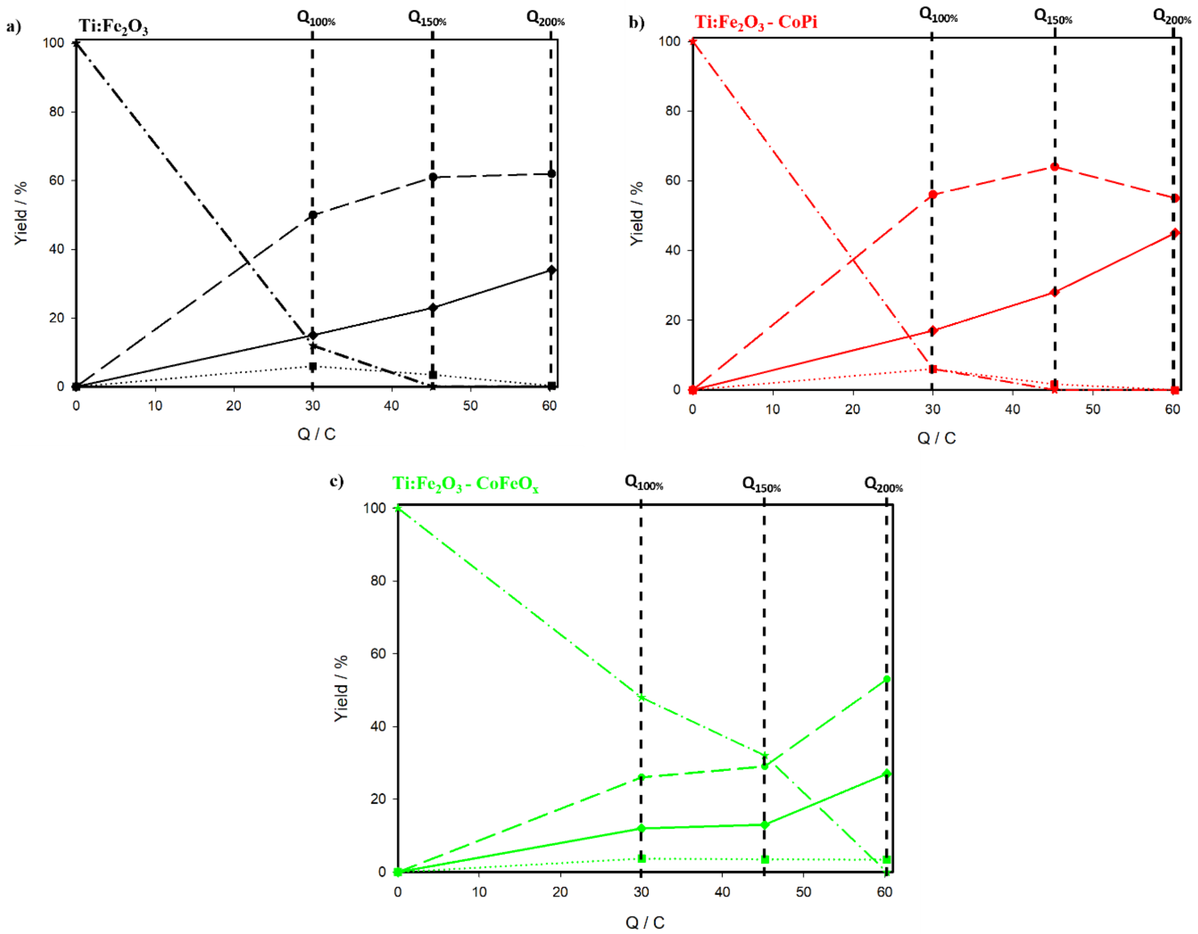

Figure 8.4 *Conversion of HMF and production of its oxidation derivatives as a function of the total charge passed in the pulsed chrono-coulometry experiments:* ***(a)*** *$Ti:Fe_2O_3$,* ***(b)*** *$Ti:Fe_2O_3$-CoPi,* ***(c)*** *$Ti:Fe_2O_3$-$CoFeO_x$. $Q_{100\%}$ represents the charge corresponding to a theoretical 6-electrons oxidation of HMF to FDCA.*

As shown in Figure 8.4, a complete consumption of HMF was achieved with all the three photoelectrodes, although with different kinetics. With the Ti:Fe_2O_3-$CoFeO_x$ photoanode (Figure 8.4c), about 50% of HMF remains at $Q_{100\%}$ and the complete disappearance of HMF is observed only at $Q_{200\%}$. The yield for the 6-electrons oxidation product, i.e., FDCA, is low (around 20%) and starts to increase only at $Q_{150\%}$. This result can be ascribed to strong competition by the OER when $CoFeO_x$ is employed as the co-catalyst. On the other hand, pristine Ti:Fe_2O_3 and Ti:Fe_2O_3-CoPi (Figure 8.4a and b) yield to an almost complete photoconversion of HMF at $Q_{100\%}$, indicating a far better selectivity toward HMF oxidation compared to OER. Accordingly, Ti:Fe_2O_3 and Ti:Fe_2O_3-CoPi photoanodes exhibit a similar increase for the formation of FFCA and FDCA up to $Q_{150\%}$ (around 45 C). Beyond $Q_{150\%}$, the FDCA content increases, and this effect is more pronounced when CoPi is present on the Ti:Fe_2O_3 surface, suggesting a relevant contribution of the co-catalyst in the last step of HMF photooxidation. Notably, for all photoanodes, the amount of DFF remained consistently low (<10%) throughout the photoconversion. This aligns with previous works and can be ascribed to the presence of TEMPO which not only enhances selectivity for HMF oxidation (as shown in the mechanism in *Chapter 4, Figure 4.5*), but also promotes the final oxidation step from FFCA to FDCA. This effect was confirmed by an experiment conducted without TEMPO, where minimal HMF conversion occurred, and mostly DFF was accumulated (Table 8.1, CA at 1.16V vs RHE in 0.5M borate buffer, charged passed equal to $Q_{100\%}$).

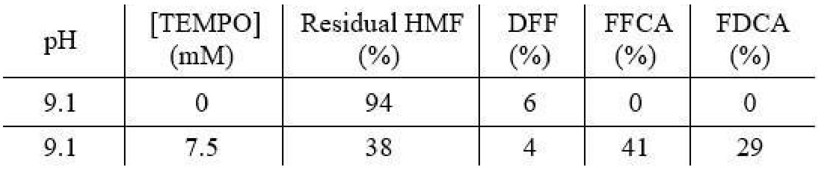

pH	[TEMPO] (mM)	Residual HMF (%)	DFF (%)	FFCA (%)	FDCA (%)
9.1	0	94	6	0	0
9.1	7.5	38	4	41	29

The Faradaic Efficiencies (FEs) for the formation of DFF, FFCA and FDCA during the HMF photoconversion experiment were calculated following *Equation 6.1* in *Chapter 6* and considering $n=2,4,6$ exchanged electrons for DFF, FFCA and FDCA, respectively. Then, the overall FE, given by the sum of FEs associated to each oxidative intermediate, was determined and the resulting trends are shown in Figure 8.5a. A large drop in FE is observed when $CoFeO_x$ is employed as co-catalyst, further confirming the inadequacy of $CoFeO_x$ in suppressing OER. On the other hand, CoPi addition increases the FE towards HMF oxidation products with respect to bare Ti:Fe_2O_3, as a result of decreased competition from OER. Remarkably, an enhanced selectivity for FDCA was achieved with Ti:Fe_2O_3-CoPi photoanode, which remains constant throughout the entire chrono-coulometry (Figure

8.5b).

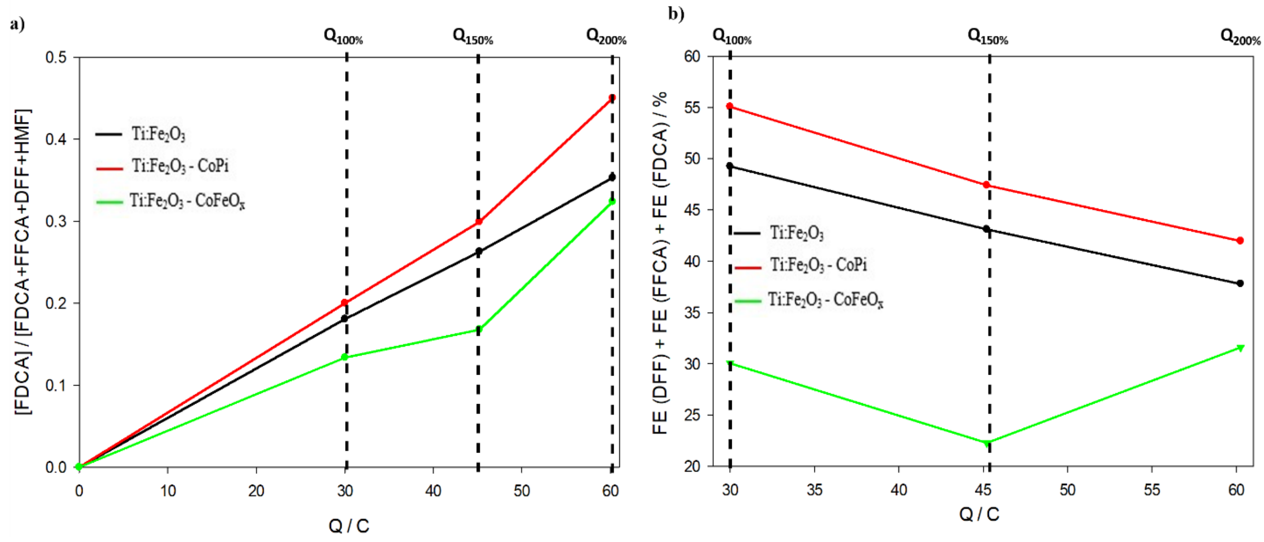

***Figure 8.5 (a)** Sum of FEs for DFF, FFCA and FDCA intermediates and **(b)** Selectivity for FDCA, as a function of the charge passed during the pulsed chrono-coulometry for Ti:Fe_2O_3 (black), Ti:Fe_2O_3-CoPi (red) and Ti:Fe_2O_3-$CoFeO_x$ (green) photoanodes. $Q_{100\%}$ represents the charge corresponding to a theoretical 6-electrons oxidation of HMF to FDCA.*

The resulting FE at $Q_{100\%}$ for pristine Ti:Fe_2O_3, Ti:Fe_2O_3-CoPi and Ti:Fe_2O_3-$CoFeO_x$ are 49%, 55% and 30%, respectively. For a valid comparison, only the FE calculated at $Q_{100\%}$ is considered, as higher conversion yields would be influenced by reactant consumption.

8.3 Optimization of FDCA production

Despite the improvements achieved by engineering the Ti:Fe_2O_3 surface with a tailored co-catalyst, the absolute FE is still far from ideal. Even with a thick layer of CoPi co-catalyst, water oxidation is still a strongly competing process, reducing the FE for HMF oxidation, especially at the low HMF concentrations used (2.5 mM). To eliminate OER competition, one possible approach would involve replacing the reaction environment with a dry organic electrolyte, previously demonstrated to be compatible with PEC valorisation reactions coupled to hydrogen evolution[144]. However, preliminary results in this direction displayed negligible HMF conversion to FDCA, with the reaction primarily yielding DFF and by-product (*Table 8.2* chronoamperometry at 0.8V vs Ag/$AgNO_3$).

Electrolyte	Q / C	Residual HMF (%)	DFF (%)	Others
ACN/$LiClO_4$ 0.1M	14	47	10	43

This outcome underscores the essential role of a basic aqueous medium in establishing the aldehyde hydration equilibrium which is crucial for the final oxidation step to carboxylic acid (*Chapter 4*,

Figure 4.5), as well as the importance of carefully optimizing experimental conditions to improve selectivity toward the desired oxidation product.

Based on the hypothesis that a limiting factor is constituted by mass transport of TEMPO to the photoanode surface (which is not a problem in the case of water, as it is the solvent), we performed experiments in saturated TEMPO (ca. 60 mM) borate buffer solution (0.25 M, pH 9.2) with Ti:Fe_2O_3 and Ti:Fe_2O_3-CoPi photoanodes. Under these experimental conditions, complete conversion of HMF to FDCA was achieved at $Q_{100\%}$ both with and without CoPi, indicating that a higher concentration of TEMPO is beneficial for a more efficient competition with the OER, although practically not sustainable, nor economically viable in the process scale-up.

To overcome the mass transport limitation, we tested a reduced-volume cell (1.8 mL vs 23 mL, Figure 8.6a) for the PEC oxidation of HMF (~6 mM) in borate buffer (0.25 M, pH 9.2) and in the presence of the standard TEMPO concentration used in this work (~6.5 mM). Such experimental apparatus ensured highly efficient stirring of the entire electrolyte volume, granting improved mass transport during the conversion experiment. Interestingly, at $Q_{100\%}$, a remarkable 86% yield for FDCA production was obtained for the CoPi-modified electrode compared to 54% in the absence of CoPi (Figure 8.6c).

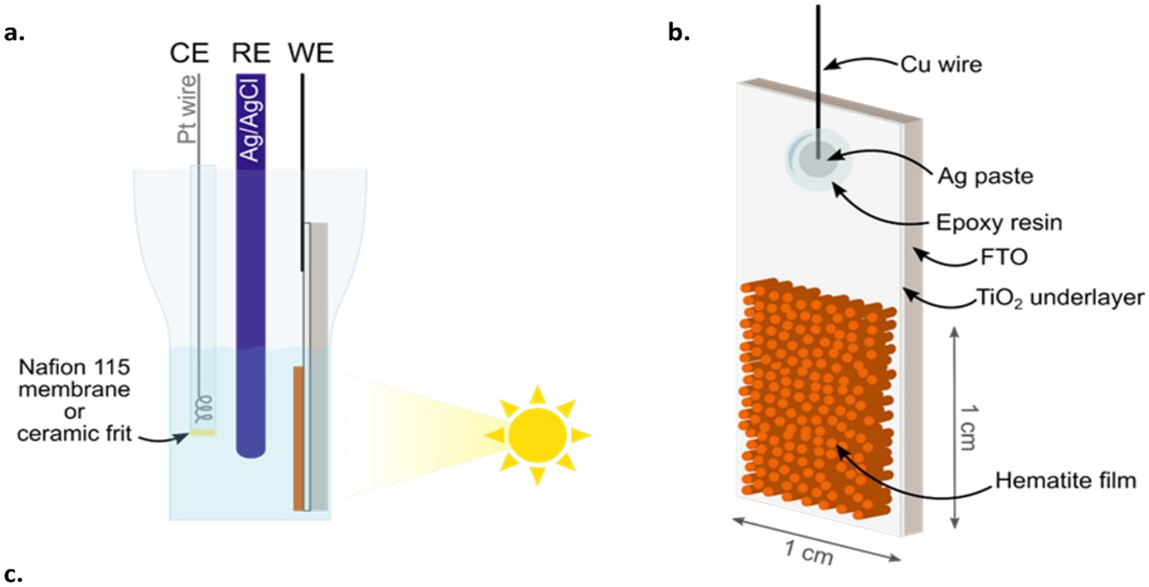

c.

Photoanode	Vol (mL)	HMF charge equivalent (%)	HMF (mM)	TEMPO (mM)	FE (%)	FDCA yield (%)
Ti:Fe_2O_3	1.8	100	6.1	6.5	49	54
Ti:Fe_2O_3-CoPi	1.8	100	6.4	6.5	79	86

Figure 8.6 ***(a)*** *Schematic representation of the reduced volume PEC cell and* ***(b)*** *details of the photoanode.* ***(c)*** *Results achieved with Ti:Fe_2O_3 and Ti:Fe_2O_3-CoPi photoanodes in the reduced-volume cell at 1.6V vs RHE.*

When compared to the available literature in the field (*Chapter 4*, *Table 4.1*), Ti:Fe_2O_3-CoPi shows results on par with state-of-the-art $BiVO_4$ photoanodes in terms of selectivity for HMF photoconversion to FDCA. Additionally, it significantly outperforms previously reported hematite-based photoanodes in mildly basic aqueous environments (pH 9.2).

8.4 Mechanistic description of charge transfer kinetics

To gain a deeper understanding of the enhanced selectivity of CoPi in promoting HMF oxidation to FDCA, we examined the behaviour of photogenerated holes in both bare Ti:Fe_2O_3 and Ti:Fe_2O_3-CoPi with Intensity Modulated Photocurrent Spectroscopy (IMPS). The kinetic study was performed under the same experimental conditions as those of the PEC conversion, thereby using a 0.25 M borate buffer solution and HMF and TEMPO at concentrations of 2.5 mM and 6.5 mM, respectively. The IMPS data were analysed with a novel technique called Lasso Distribution of Relaxation Time (L-DRT), which simplifies the identification of charge separation and recombination processes, as well as the evaluation of transfer and recombination rates at the semiconductor/electrolyte interface (more details on the technique are available in *Chapter 6, Section 6.3.2*). To explore the role of CoPi in TEMPO-mediated HMF oxidation, we began by analysing the Gartner current, J_G, which represents the photogenerated current density reaching the semiconductor/electrolyte interface. This quantity is primarily influenced by bulk phenomena and, when normalized by incident light intensity, represents the charge separation efficiency (CSE) multiplied for the light harvesting efficiency (LHE). Although for both photoanodes J_G remains relatively stable upon the addition of various species to the electrolyte, a strong variation is observed between the two samples. Unlike unmodified Ti:Fe_2O_3, the CoPi-modified one leads to a higher J_G at low applied potential (< 1.1V vs RHE) and to a slightly lower J_G at high potential, when the dark current starts increasing (Figure 8.7).

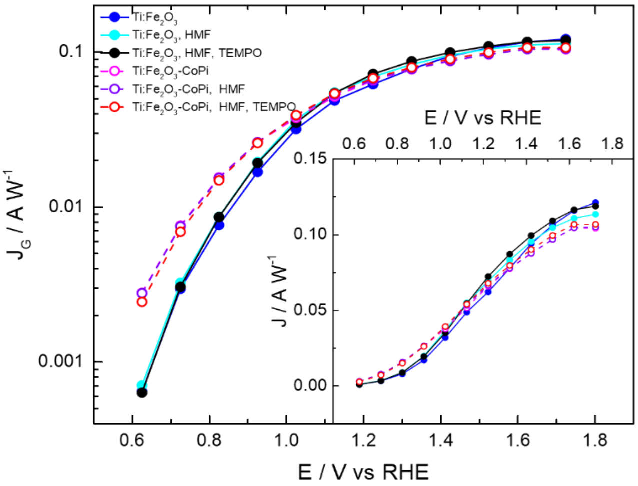

Figure 8.7 *Gartner current J_G calculated using L-DRT algorithm and normalized by the intensity of incident light for Ti:Fe_2O_3 and Ti:Fe_2O_3-CoPi.*

This measurement suggests that the accumulation of photogenerated charges at the semiconductor/electrolyte interface, which significantly enhances charge separation, is mainly promoted by CoPi at low potential. As previous studies already demonstrated the efficient extraction of photogenerated holes from hematite by CoPi co-catalyst in water splitting reaction[145][146], these findings strengthen the role of CoPi as both a hole-collecting layer and an oxygen evolution catalyst. The fact that no effects on J_G are observed upon the addition of HMF and TEMPO must be ascribed to the effect of the recombination current, J_{rec}, which is generated by bulk free electrons recombining with surface trapped holes and has opposite sign. As shown in Figure 8.8, Ti:Fe_2O_3 exhibits a higher J_{rec} compared to Ti:Fe_2O_3-CoPi, with a peak maximum around 1.2V vs RHE, which is typically attributed to surface recombination centres[147]. The addition of HMF slightly reduces the recombination peak in both bare Ti:Fe_2O_3 and Ti:Fe_2O_3-CoPi, indicating that HMF more effectively intercepts surface-trapped photogenerated holes. Notably, only with Ti:Fe_2O_3-CoPi photoanode, the addition of TEMPO leads to a twofold reduction in J_{rec} at low potentials, indicating a substantial improvement in the holes' extraction.

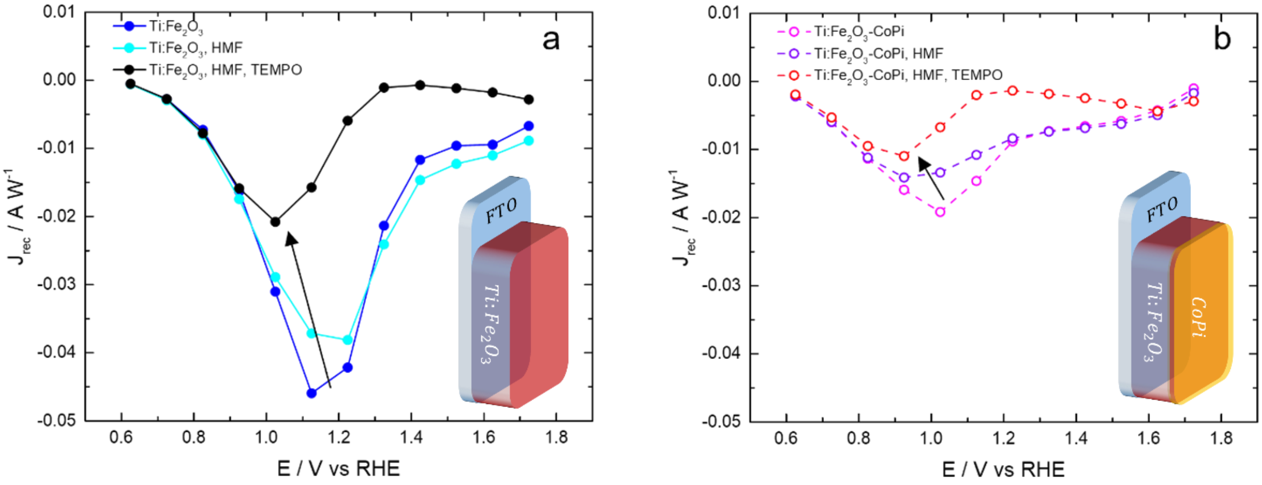

Figure 8.8 (a) *J_{rec} of Ti:Fe_2O_3 and* ***(b)*** *Ti:Fe_2O_3-CoPi as a function of the applied potential.*

According to IMPS theory[121], J_{rec} depends on the rate at which holes accumulated at the surface are transferred to the species in the electrolyte, k^{trans} , and on the rate at which they recombine with electrons from the bulk, k^{rec}. So, to explain the behaviour of J_{rec} , it is essential to examine the trends of both k^{trans} and k^{rec} rates as a function of the applied potential. These parameters can be accurately determined across the entire potential range using L-DRT analysis. For both samples a significant dependence of k^{trans} (Figure 8.9a) and k^{rec} (Figure 8.9a) on the applied potential was observed, spanning over two orders of magnitude from 0.1 to 10 s^{-1}. This behaviour is typical of bare hematite in aqueous solution (with only borate buffer) and suggests a high density of surface states, resulting in a metal-like behaviour of the surface[147][146]. With Ti:Fe_2O_3, k^{trans} increases by about one order of magnitude upon the addition of HMF, going from 0.1 to 1 s^{-1}, and another order of magnitude, from 1 to 10 s^{-1}, with TEMPO, in the potential range between 0.8 and 1.2V vs RHE (lines with full circles in Figure. 8.9a). In the same potential range, k^{rec} remains almost unaffected by the introduction of these chemicals and it decreases only above 1.2V vs RHE following the addition of TEMPO (lines with full circles in Figure. 8.9b). So, the reduction in J_{rec} observed with this photoanode after adding HMF and TEMPO (Figure 8.8a), can mostly be attributed to an increase in k^{trans}.

In contrast, for Ti:Fe_2O_3-CoPi photoanode, the dependence of k^{trans} on the applied potential is substantially lower than previous sample, regardless of the presence of HMF and TEMPO (lines with empty circles in Figure 8.9a), and k^{rec} decreases by about one order of magnitude in the whole potential range (above 0.8V vs RHE, lines with empty circles in Figure 8.9b). The addition of TEMPO decreases k^{rec} above 1.1V vs RHE, meanwhile HMF has no effect on this rate constant. According to these observations, the remarkable reduction in J_{rec} following CoPi modification (Figure 8.8b) is primarily due to a suppression of recombination processes, i.e. a decrease in k^{rec}, rather than an enhancement of charge transfer processes.

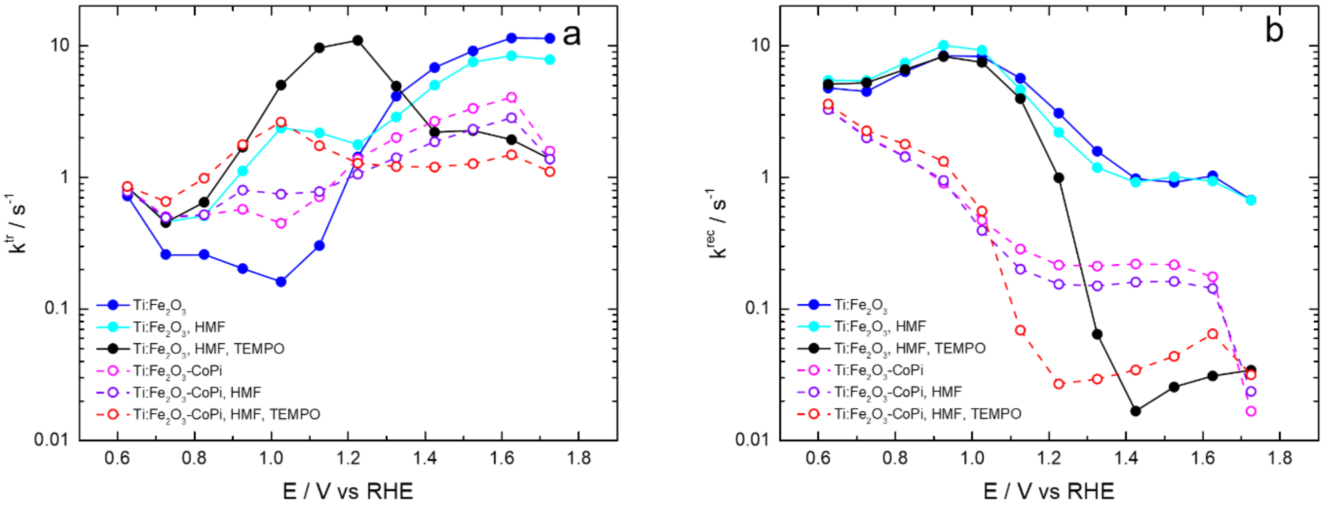

***Figure 8.9 (a)** transfer rate k^{trans}, **(b)** recombination rate k^{rec} of Ti:Fe_2O_3 and Ti:Fe_2O_3-CoPi.*

To corroborate IMPS measurements, the capacitive response at the interface was investigated by means of Electrochemical Impedance Spectroscopy (EIS) on bare Ti:Fe_2O_3 and Ti:Fe_2O_3-CoPi. The measurements were performed in 0.5 M borate buffer, either in the presence or in the absence of 6.5 mM TEMPO.

For Ti:Fe_2O_3 photoanode a simple nested RC mesh was adopted as equivalent circuit, used by various authors[148], to take into account the main dynamic processes following charge separation (Figure 8.10). Charge transfer across the semiconductor is described by the R_{ct}-C_{sc} element where C_{sc} =

Constant Phase Element is a non-ideal capacitance originated by a distribution of relaxation time constant, typical in porous interfaces of our interest. The R_{rec}-C_{ss} element represents recombination via trap states/surface states (interfacial recombination). R_s is the potential independent resistance, due to the contact and ohmic resistance of the electrolyte.

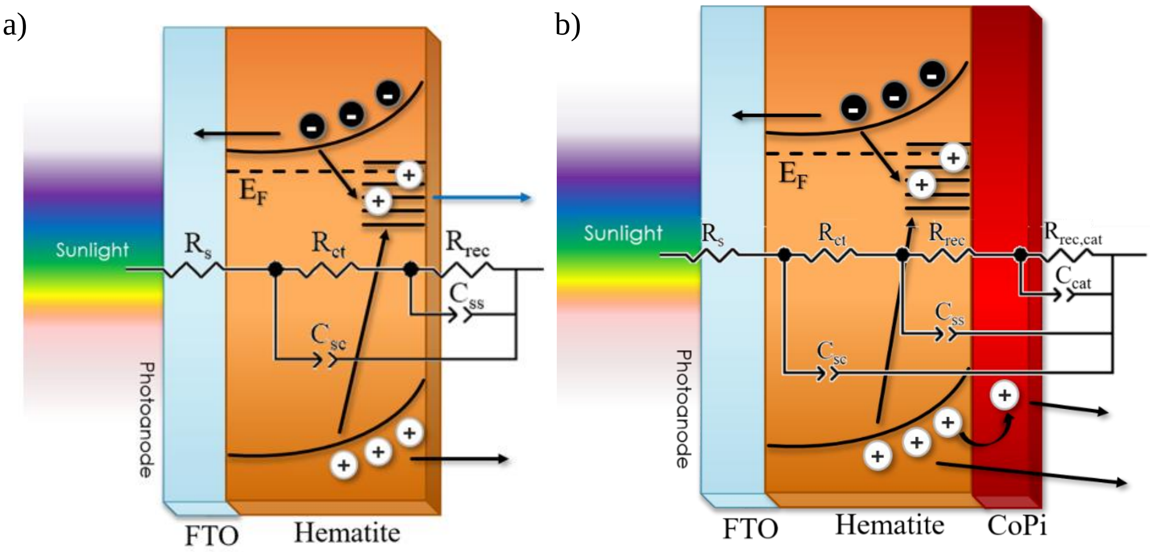

Figure 8.10 (a) *General charge transfer and recombination pathways in Ti:*Fe_2O_3 *electrodes, and equivalent circuit used for fitting the EIS response. The FTO Ohmic contact is represented by the pale blue slab. Charge transfer to the electrolytic solution can occur through trapped and valence band holes (blue and black arrows).* ***(b)*** *Ti:*Fe_2O_3*-CoPi electrode and the equivalent circuit to model the EIS response.* C_{cat} *is the constant phase element (CPE) modelling the chemical capacitance of CoPi.*

Fitting with the model above was generally successful in reproducing the J/V characteristics of the photoanode as shown by the good overlap of the computed points (blue squares in Figure 8.11a) with the reciprocal derivative of the J/V (red continuous line). We observe that the recombination resistance R_{rec} (grey squares) displays a minimum in correspondence to the chemical capacitance peak due to C_{ss} (cyan squares), which reflects the hole trapping capacitance and spans the interval between 1 and 1.3V vs RHE, corresponding to inflection point of the respective J/V characteristics. When the applied bias is strong enough, electrons are swept to the back contact, and no longer recombine with trapped holes. Thus, the chemical capacitance peak (C_{ss}) disappears and the recombination resistance (R_{rec}) increases. The EIS analysis of Ti:Fe_2O_3 in the presence of TEMPO (Figure 8.11b) outlines the same features described above with an additional resistance peak around 0.9V vs RHE, associated to the reduction of the electron mediator at the Ti:Fe_2O_3 interface. The trapped hole capacitance peak, C_{ss} peak, displays an intensity similar as the previous case but with a cathodic shift, consistent with the one observed in the J/V curves. This confirms that the presence of

TEMPO reduces the required bias to counteract recombination and directly promotes a faster hole scavenging reaction at the Ti:Fe_2O_3/electrolyte interface.

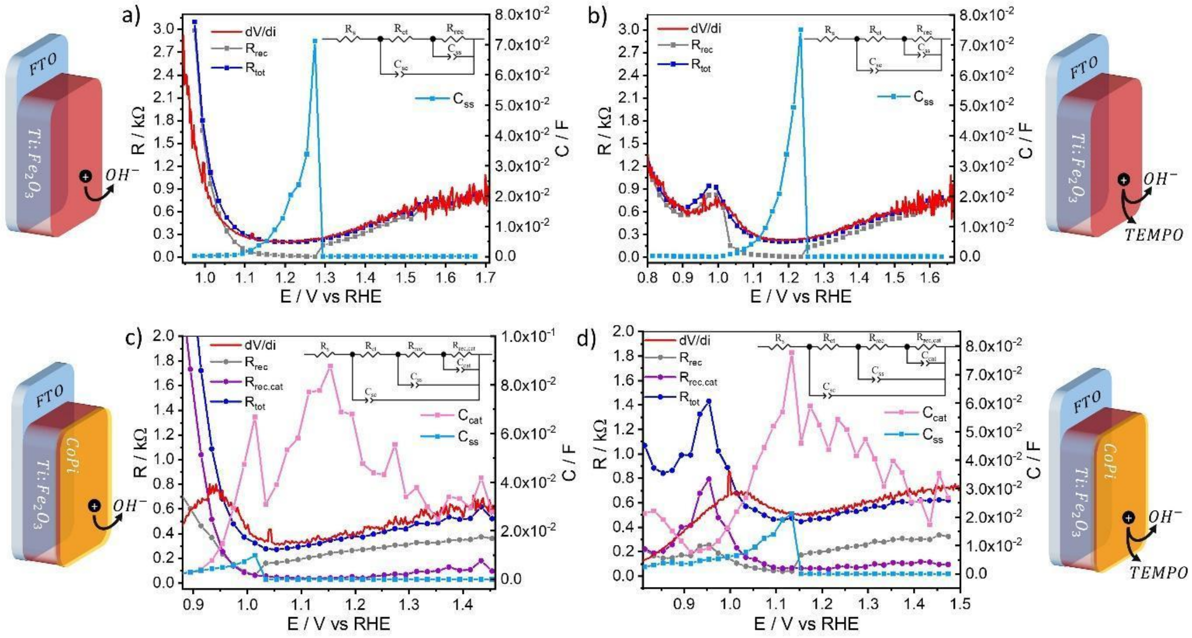

Figure 8.11 *Resistive and capacitive contribution of Ti:Fe_2O_3 in **(a)** borate buffer or **(b)** with the addition of TEMPO to the electrolyte, extracted from EIS data fitting. **(c)-(d)**: Corresponding resistive and capacitive contribution for Ti:Fe_2O_3-CoPi.*

In the presence of CoPi, an additional nested RC element ($R_{rec,cat}$-C_{cat}) was inserted to model the charge transfer across the catalyst layer (Figure 8.10b). We postulate that transfer to the electrolyte through CoPi occurs via surface states in hematite, and that recombination resistances should be added, since holes inside the CoPi layer become largely decoupled from electrons in the semiconductor. Fitting of the experimental data with such model affords the results in Figure 8.11c, which again show a good agreement between the total resistance (R_{tot}, blue dots) and the reciprocal derivative of the J/V curve (red line) above ≈ 1 V. The deviation at lower potentials is due to a dark faradaic process (visible in cyclic voltammetries, not shown here) assigned to either reduction of TEMPO or TEMPO oxidation by-products generated by the photoelectrochemical process. The plot of the capacitance reveals that the trapped hole density in Ti:Fe_2O_3 (C_{ss}) decreases by a factor of $\approx$10, becoming marginal at voltages higher than 1.05V vs RHE, whereas the CoPi associated capacitance (C_{cat}) exhibits a broader distribution spanning the entire 0.9-1.5V vs RHE interval, with an anticipated onset (ca. 0.9V vs RHE) with respect to Ti:Fe_2O_3. This means that electron/hole separation in the CoPi modified electrodes occurs at a lower bias than in Ti:Fe_2O_3, probably thanks to heterointerfacial effects that increase the depletion field inside the semiconductor. The CoPi capacitance displays a peak cantered around 1.15V vs RHE which represents the quasi-Fermi level reached by the catalyst under steady state illumination conditions. We also note that $R_{rec,cat}$ increases as the chemical capacitance of CoPi decreases, corroborating its assignment to the recombination resistance across CoPi. In the presence of TEMPO (Figure 8.11d), the EIS response is similar to Figure 8.11c in terms of resistance and chemical capacitance. Remarkably, however, the CoPi capacitance peak significantly decreases, as shown more clearly in the comparison Figure 8.12. Notably, the charge trapped in CoPi, determined by integrating the capacitance curves, decreases by half in the presence of TEMPO ($\int 2A(C_{(cat,TEMPO)}) \approx \int A(C_{cat})$), indicating that holes in CoPi are scavenged more rapidly and selectively by TEMPO. This is probably the key to understand the superior selectivity of Ti:Fe_2O_3-CoPi photoanodes in TEMPO-catalysed HMF oxidation. Indeed, the significant reduction in CoPi capacitance when TEMPO is used as an electron mediator highlights a strong selectivity for TEMPO oxidation, which can be effectively leveraged for biomass oxidation.

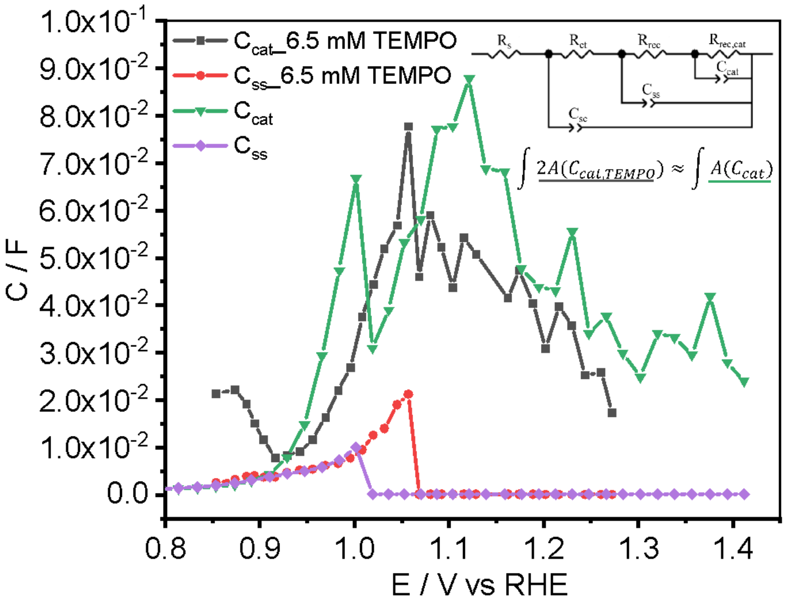

Figure 8.12 *Comparison between the capacitive contributions of the* Ti:Fe_2O_3-CoPi *in the presence and in the absence of TEMPO. In particular, the decreased chemical capacitance of CoPi (C_{cat}) in the presence of TEMPO is consistent with the efficient CoPi-mediated hole transfer to the electron mediator.*

To summarize, the addition of a $CoFeO_x$ overlayer onto Ti:Fe_2O_3 surface hinders FDCA production, due to a strong competition with the OER. In contrast, CoPi modification significantly enhances FDCA selectivity, achieving an 86% yield for FDCA production compared to the 54% yield obtained with the bare Ti-doped hematite, while also improving Faradaic efficiency. These results are particularly notable as they were achieved using earth-abundant titanium-doped hematite photoanodes at pH 9.2, which is a milder basic aqueous environment than that of previous studies (pH $\geq$ 12) where HMF stability was poor and water reduction to hydrogen was less favourable (*Chapter 4*, *Table 4.1* in *Section 4.2*). Additionally, the investigation of charge carrier dynamics through EIS and the newly introduced L-DRT algorithm for IMPS analysis highlighted the crucial role of the CoPi layer in suppressing recombination processes and enhancing hole transfer efficiency to TEMPO, thereby improving the overall catalytic performance.

Building on these findings, in the next chapter we sought to further optimize the HMF PEC oxidation by eliminating the reliance on TEMPO, which undermines the economic viability and sustainability of the PEC process.

9. Direct HMF photoelectrochemical oxidation to FDCA with Ti:Fe_2O_3 photoanodes modified with Ni-based co-catalysts

Direct electrocatalytic HMF oxidation in absence of redox mediator was previously achieved by means of electrocatalysts[149][150] based on Ni, an affordable transition metal with a low supply risk indicator[151]. Previous works showed that two possible pathways can be followed by nickel-based catalysts to electrochemically oxidise alcohols and aldehydes. In the indirect oxidation mechanism (*Scheme 9.1*), first reported by Fleischmann et al.[152,153]**,** the catalyst is oxidized by the applied potential from Ni^{2+} to Ni^{3+} (process 1), followed by the hydrogen atom transfer (HAT, process 3) from the carbon in the α position of the alcohol (or geminal diol, in the case of the aldehyde) to the Ni^{3+} site, therefore reducing the catalyst back to its initial state. This step is also considered to be the rate determining step (RDS) of the entire process. In this mechanism, both the alcoholic and the aldehydic groups are directly oxidized to the corresponding carboxylic acid and 4 electrons are involved (*Scheme 9.1*).

$$OH^- + Ni(OH)_2 \xrightleftharpoons[\text{fast}]{-\,e^-} NiOOH + H_2O \tag{1}$$

$$(RCH_2OH)_{sol} \rightleftharpoons (RCH_2OH)_{abs} \tag{2}$$

$$(RCH_2OH)_{abs} + NiOOH \xrightarrow[\text{RDS}]{\text{HAT}} R\dot{C}HOH_{abs} + Ni(OH)_2 \tag{3}$$

$$R\dot{C}HOH_{abs} + 3NiOOH + H_2O \longrightarrow RCOOH_{sol} + 3Ni(OH)_2 \tag{4}$$

Scheme 9.1 *Mechanism for the indirect oxidation of alcohols at NiOOH electrodes in alkaline media, as proposed by Fleischmann et al.*[152,153]*. For the aldehydes (RCHO instead of RCH_2OH), an initial hydration is needed to form the 1,1-geminal diol, before undergoing the equivalent oxidation mechanism*[140].

At more positive potentials, the so called potential dependent (PD) oxidation mechanism can take place (*Scheme 9.2*) [140]. In this case, the applied potential is needed not only to oxidize Ni^{2+} to Ni^{4+} (process 1), but also to drive the hydride transfer reaction (process 4), through which the alcoholic group is oxidized to aldehyde (while, for the aldehyde, the 1,1- geminal diol is oxidized to carboxylic acid).

$$2OH^- + Ni(OH)_2 \overset{-2e^-}{\longleftrightarrow} NiO_2 + 2H_2O \tag{1}$$

$$OH^- + (RCH_2OH)_{sol} \longleftrightarrow (RCH_2O^-)_{sol} + H_2O \tag{2}$$

$$(RCH_2O^-)_{sol} \longleftrightarrow (RCH_2O^-)_{abs} \tag{3}$$

$$(RCH_2O^-)_{abs} + NiO_2 \xrightarrow[\text{transfer}]{\text{hydride}} RCHO_{sol} + Ni(OH)O^- \tag{4}$$

$$Ni(OH)O^- + OH^- \xrightarrow[\text{RDS}]{-2e^-} NiO_2 + H_2O \tag{5}$$

***Scheme 9.2** Potential dependent (PD) oxidation mechanism proposed by Bender et al.*[140] *In this case, the alcohols are oxidised to aldehydes through hydride transfer. Aldehyde oxidation to carboxylic acid can occur according to the same mechanism, prior the establishment of an equilibrium with its hydrated form, i.e., the 1,1-geminal diol.*

It has been demonstrated that aldehyde groups preferentially oxidise through the indirect pathway, while alcoholic groups follow the PD one. Since HMF has both an alcoholic and aldehydic group in its structure (Figure 4.2), the dominant mechanism will depend on the experimental conditions applied to perform the oxidation[140].

For this study, Ti:Fe_2O_3 photoanodes were modified with nickel-based co-catalysts and tested for the direct PEC oxidation of HMF to FDCA at the anodic side of a two-compartments PEC cell. The deposition was performed according to different techniques: via $Ni(OH)_2$ electrodeposition, resulting in Ti:Fe_2O_3-Ni photoanode, and via NiMo sputtering, leading to Ti:Fe_2O_3-NiMo photoanode. Further details regarding the synthesis are available in *Chapter 7, Section 7.2.* While the $Ni(OH)_2$/NiOOH redox couple has been widely investigated for the electrochemical oxidation of various substrates, only few works report the use of NiMo co-catalyst for anodic reactions, mostly focusing on OER[154]. Since NiMo can also be employed to perform the reductive semi-reaction at the cathode, e.g., the hydrogen evolution reaction (HER) or CO_2 reduction[155–157], its bifunctional activity will help reducing the fabrication impact of the PEC device, using the same co-catalyst at both sides. Most importantly, with this approach an abundant energy source, such as sunlight, is exploited to promote HMF oxidation in absence of redox mediator or critical raw materials-based co-catalysts[151].

The efficiency of the conversion process in alkaline environment (0.1 M NaOH pH 13) was evaluated by combining the photoanode PEC characterization with the monitoring of the reaction evolution by HPLC, spectro-photometric and fluorometric techniques. Operando electrochemical X-ray Absorption Spectroscopy (XAS) provided deeper insights into the reaction mechanism, specifically examining the impact of HMF addition on the oxidation state of Ni across a range of selected potentials. Notably, the innovative Fixed Energy X-ray Voltammetry (FEXRAV) technique enabled element-specific voltammetric analysis, shedding light on the microscopic interactions between Ni and HMF.

9.1 PEC characterization

The synthesized Ni-modified Ti-doped hematite photoanodes, i.e., Ti:Fe_2O_3-Ni and Ti:Fe_2O_3-NiMo, were first tested photoelectrochemically for the OER and compared with the bare Ti:Fe_2O_3.

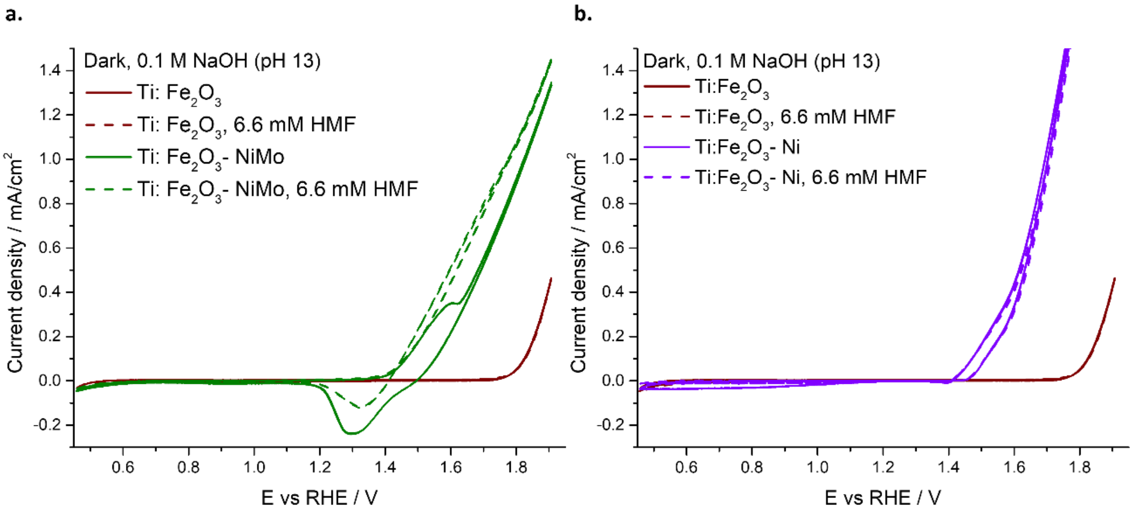

Figure 9.1 *Dark CVs before (solid line) and after (dotted line) the addition of HMF with:* ***(a)*** *Ti:Fe_2O_3-NiMo (green) and Ti:Fe_2O_3 (red);* ***(b)*** *Ti:Fe_2O_3-Ni (violet) and Ti:Fe_2O_3 (red) photoanodes.*

The dark CVs acquired for the Ni-modified photoanodes highlight a significant anticipation of the dark onset potential compared to Ti:Fe_2O_3 (Figure 9.1). In the bare electrolyte without HMF, Ti:Fe_2O_3-NiMo exhibits the oxidation/reduction waves usually attributed to the $Ni(OH)_2$/NiOOH redox couple[140] (Figure 9.1a, solid line). When HMF is introduced (Figure 9.1a, dashed line), the oxidation wave fades, indicating a rapid transfer of holes to HMF. Accordingly, the reduction wave significantly decreases, suggesting that most of the catalyst has already been reduced by the swift transfer of positive charge to HMF.

For Ti:Fe_2O_3-Ni photoanode without HMF, the oxidation/reduction peaks between 1.2V-1.4V vs RHE, typically attributed to the $Ni(OH)_2$/NiOOH redox couple[140], are barely noticeable (Figure 9.1b, solid line). Additionally, a broad feature appears in the reverse scan, extending across a wide region of cathodic potentials. Notably, this reductive wave is unique to this photoanode, as it was not observed with either Ti:Fe_2O_3 or Ti:Fe_2O_3-NiMo electrodes. Further measurements confirm that this behaviour is intrinsic to the electrodeposited $Ni(OH)_2$, as it also occurs when $Ni(OH)_2$ is deposited on FTO (Figure 9.2a). Moreover, it persists when CVs are conducted under Ar, suggesting the reductive process is not related to oxygen reduction (Figure 9.2b). Upon addition of HMF, the feature in the cathodic region disappears (Figure 9.1b, dashed line). As in the case of Ti:Fe_2O_3-NiMo, the addition of the organic substrate would produce a swift scavenging of the excess positive charge on the oxidized Ni site, preventing the cathodic process related to the co-catalyst reduction.

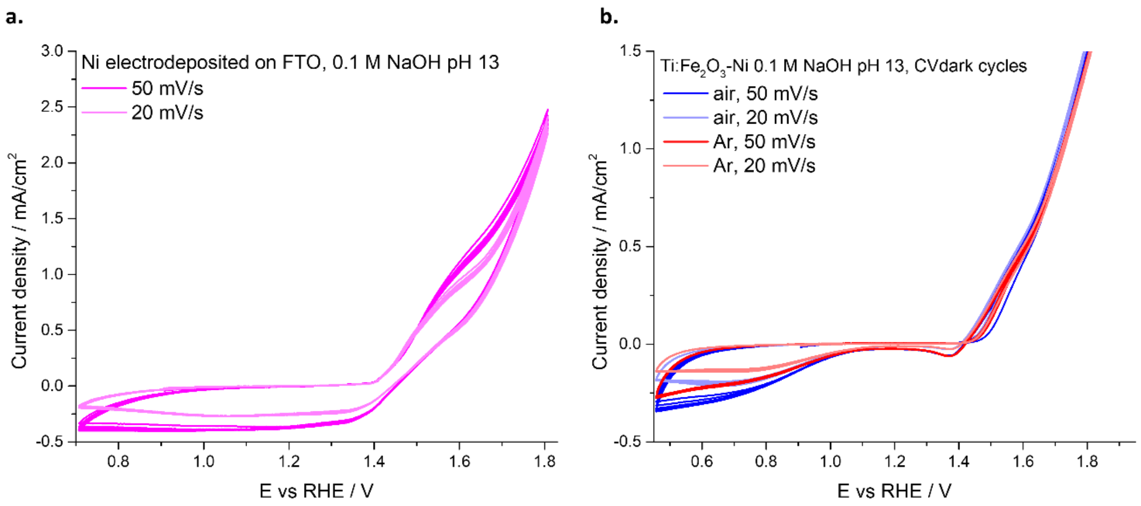

Figure 9.2 (a) *Repeated dark CVs in air with nickel- electrodeposited FTO (FTO-Ni) (pink lines);* ***(b)*** *Repeated dark CVs in air (blue lines) and in argon atmosphere (red lines) with Ti:Fe_2O_3- Ni photoanode. The brightening of the colours in both plot (a) and (b) represents the decreasing of the scan rate: from 50 mV/s to 20 mV/s.*

Chopped LSVs were collected for the three photoanodes, before (Figure 9.3, solid lines) and after (Figure 9.3, dotted lines) the addition of HMF to the electrolyte. The presence of the electrocatalysts anticipates both the dark- and the photo- onset potentials and reduces the recombination spikes observed with Ti:Fe_2O_3 photoanode. As a result, Ti:Fe_2O_3-Ni and Ti:Fe_2O_3-NiMo reach significant values of the current density earlier than water oxidation potential, with a slight increase upon the addition of HMF.

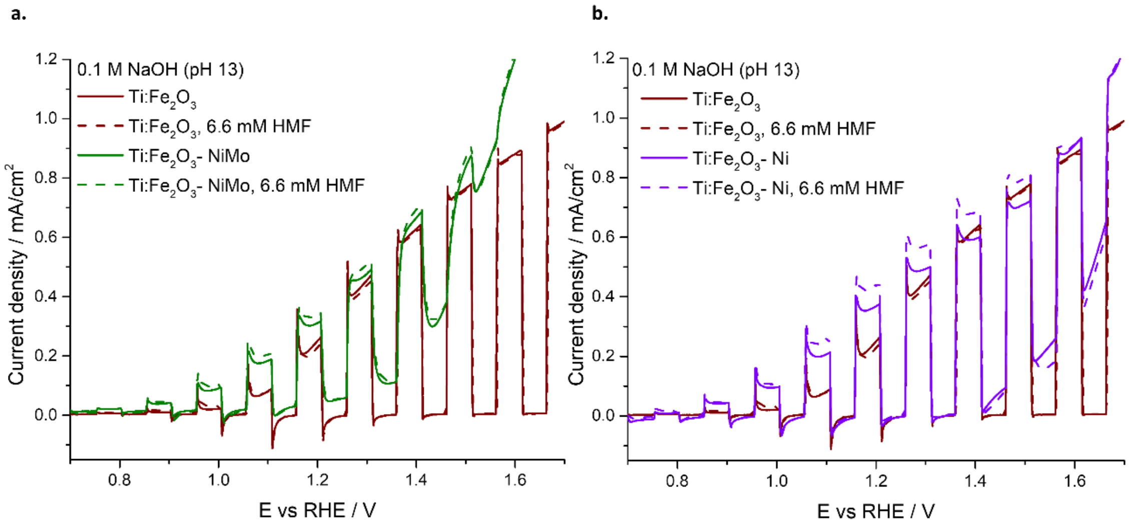

Figure 9.3 *Chopped LSVs before* ***(a)*** *and after* ***(b)*** *the addition of HMF for: Ti:Fe_2O_3 (red), Ti:Fe2O3-Ni (violet) and Ti:Fe2O3-NiMo (green) photoanodes.*

The PEC stability of the Ni-modified Ti:Fe_2O_3 photoanodes was assessed by steady state chronoamperometry at 1.4V vs RHE (Figure. 9.4). For all the samples, after an initial decrease of the current density, the values remain stable during the whole experiment. Also, no significant differences arise when HMF is added to the electrolyte, confirming the trend observed in the chopped LSVs for this potential value (Figure 9.3).

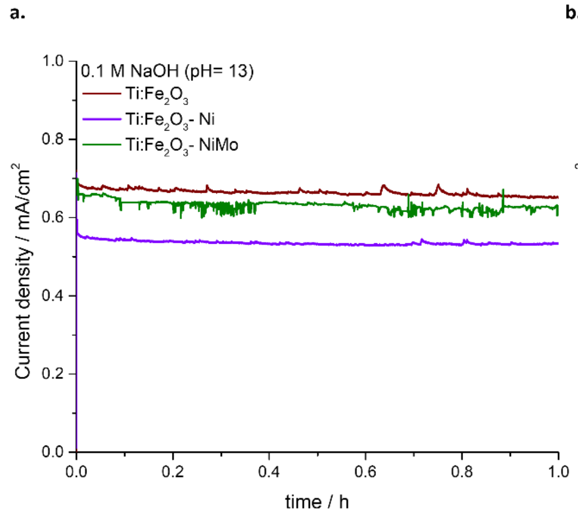

Figure 9.4 *Chronoamperometry for 1h at 1.4V vs RHE, before* ***(a)*** *and after* ***(b)*** *the addition of HMF to the electrolyte. Ti:Fe$_2$O$_3$ (red), Ti:Fe$_2$O$_3$-Ni (green) and Ti:Fe$_2$O$_3$-NiMo (violet) photoanodes.*

9.2 HMF PEC conversion

As discussed in the previous section, Ni and NiMo co-catalysts significantly influence the photoelectrochemical behaviour of Ti:Fe$_2$O$_3$ photoanode, enabling a selective hole scavenging before the onset of OER (Figure 9.3). Long-term chrono-amperometries were performed at 1.4V vs RHE (final charge of 57 C) starting with 6.6 mM HMF, the results are summarized below and details about the spectro-photometric characterization are reported in *Section 9.4.*

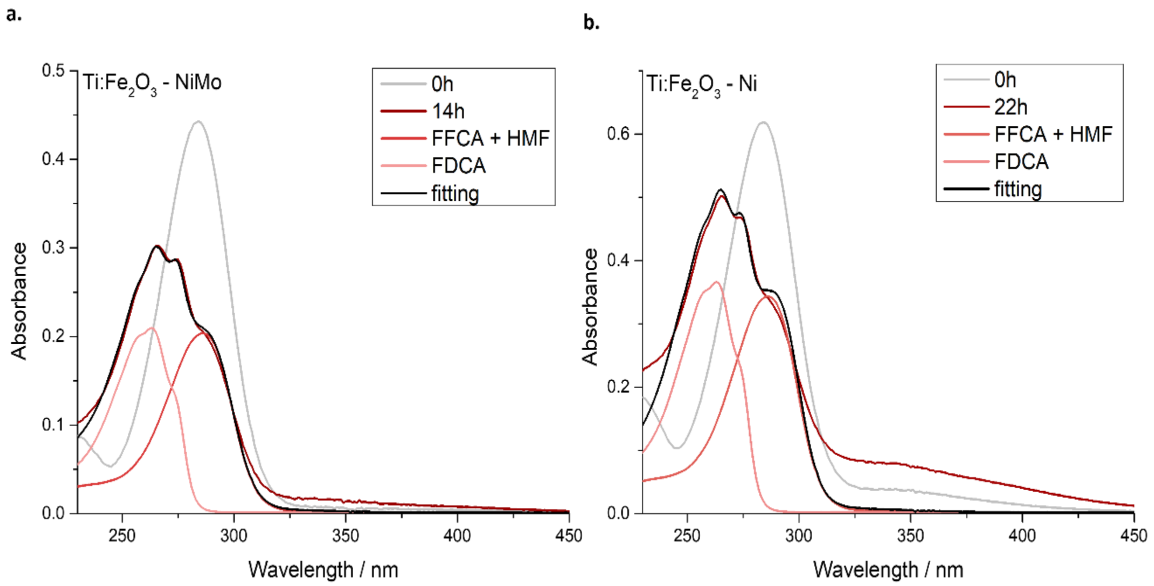

Figure 9.5 *Evolution of the absorption spectra after long-term PEC HMF conversion: the initial (0h, grey line) and final spectra (dark red line) are compared to reference FFCA or HMF (red line) and FDCA (light red line). The black line represents the best fit function.* ***(a)*** *Ti:Fe$_2$O$_3$-NiMo and* ***(b)*** *Ti:Fe2O3-Ni photoanodes.*

As shown in Figure 9.5, for both samples the initial HMF absorption spectrum (grey line) mutates to a structured spectrum (dark red lines), where a maximum around 263 nm suggests the evolution of the reaction towards the desired product FDCA given the spectral matching with reference FDCA (*Section 9.4, Figure 9.12*). It is worth noting the presence of a shoulder within 320-450 nm, which cannot be attributed to HMF oxidative intermediates, but rather to possible by-products. These species impart the yellowish hue to the solution and exhibit fluorescence when excited at λ= 350 nm (Figure 9.6). Since the colour of the solution darkened over time, the higher shoulder visible for Ti:Fe_2O_3-Ni can be ascribed to the longer time of the experiment: 22h instead of 14h to reach the same final charge as Ti:Fe_2O_3-NiMo. The black lines in Figure 9.5 represent the best fit of the final spectra by a combination of reference spectra, from which the percentage of FDCA (%) in *Table 9.1* was determined (more information about the fitting function are reported in *Section 9.4.2*).

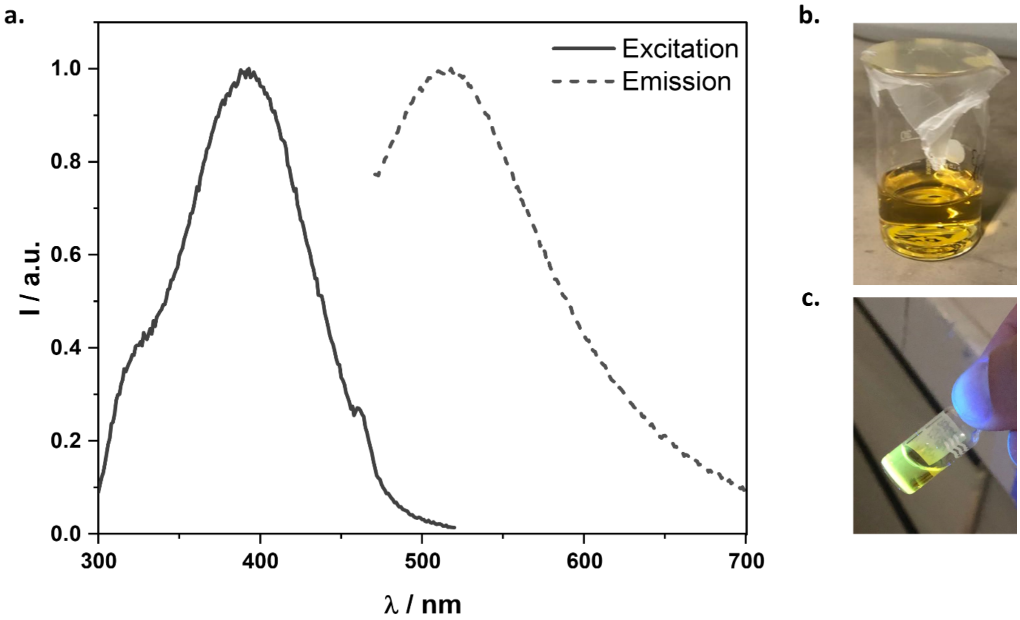

Figure 9.6 (a) *Excitation (λ_{em}= 550 nm, continuous line) and emission (λ_{exc}= 400 nm dotted line) spectra acquired after long-term PEC HMF conversion;* ***(b)*** *Colour of the anodic solution at the end of the experiment;* ***(c)*** *fluorescence of the solution.*

By means of HPLC, a more precise quantitative evaluation of the conversion percentage was carried out. As summarized in *Table 9.1* and in agreement with the spectro-photometric analysis, although the HMF to FDCA conversion was substantial, a complete conversion was not achieved, and a large quantity of by-products was generated. The occurrence of these side reactions, and the potential strategies to mitigate them, will be better addressed in the following paragraphs. HMFCA and DFF were not detected and the FDCA conversion was similar for the two photoanodes: 27% for Ti:Fe_2O_3-NiMo and 32% for Ti:Fe_2O_3-Ni. Notably, when bare Ti:Fe_2O_3 was employed, only a small amount of HMF was consumed, with the conversion predominantly following undesired pathways to by-products. This highlights the essential role of Ni-based co-catalyst in promoting a more efficient and selective HMF oxidation.

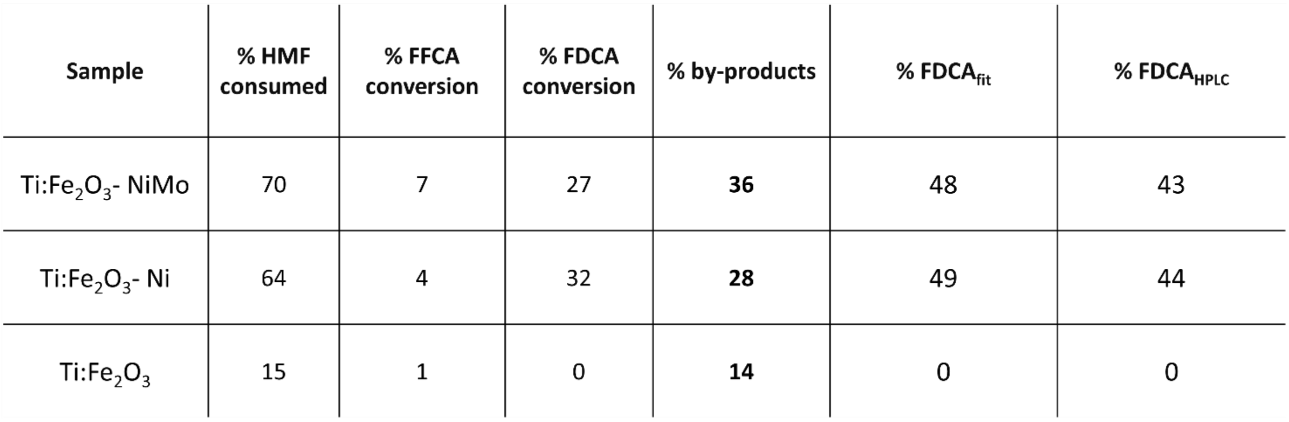

Sample	% HMF consumed	% FFCA conversion	% FDCA conversion	% by-products	% $FDCA_{fit}$	% $FDCA_{HPLC}$
$Ti:Fe_2O_3$- NiMo	70	7	27	**36**	48	43
$Ti:Fe_2O_3$- Ni	64	4	32	**28**	49	44
$Ti:Fe_2O_3$	15	1	0	**14**	0	0

Table 9.1 also shows that the relative amount of FDCA (excluding by-products), determined by fitting the optical spectra (% $FDCA_{fit}$, *Section 9.4.2*, *Equation 9.1*), aligns well with the relative conversion coefficient obtained from the HPLC results (% $FDCA_{HPLC}$, *Section 9.4.2*, *Equation 9.2*), despite a slight overestimation. This emphasizes that, while the HPLC analysis is essential for an accurate quantitative evaluation, spectro-photometry can still provide an effective marker of the produced FDCA, although it is not possible to differentiate between HMF and FFCA given the similarity of their reference spectra (*Section 9.4, Figure 9.12*). The resulting faradaic efficiency for FDCA, calculated according to *Equation 6.1* in *Chapter 6*, are 42% for $Ti:Fe_2O_3$-NiMo and 30% for $Ti:Fe_2O_3$-Ni, while it is 0 for the bare $Ti:Fe_2O_3$, again underlying the importance of Ni-based co-catalysts in tuning the selectivity of the photosynthetic process.

To investigate the nature of the by-products (*Table 9.1*) as well as to understand the role of the co-catalysts in the HMF PEC conversion, further experiments were performed.

The possible dissolution of Ni and NiMo under the applied bias was first examined, by repeating the CA without the addition of HMF to the electrolyte. In this scenario, the solution remained transparent, and no absorbing species were detected (Figure 9.7a). Via EDX analysis, the Ni/Fe and Ni/Mo ratio were determined and the results for $Ti:Fe_2O_3$-NiMo photoanode are shown in Figure 9.7b. Interestingly, while the Ni/Fe ratio was maintained, the Ni/Mo ratio increased, suggesting a significant decrease in the Mo content after the chronoamperometry, which was further confirmed by the Mo 3d XPS spectra (Figure 9.7c). The dissolution of Mo in basic aqueous environment aligns with the electrochemical behaviour of $Ti:Fe_2O_3$-NiMo photoanode, in which Mo's contribution was absent in both oxidation and reduction scans of the dark CVs (Figure 9.1a). Based on what reported in a previous work[154], the Mo dissolution from NiMo at high pH levels would not affect the co-catalyst performance but rather enhance it: a higher specific surface area develops, enriched of Ni sites which are catalytically active for HMF oxidation.

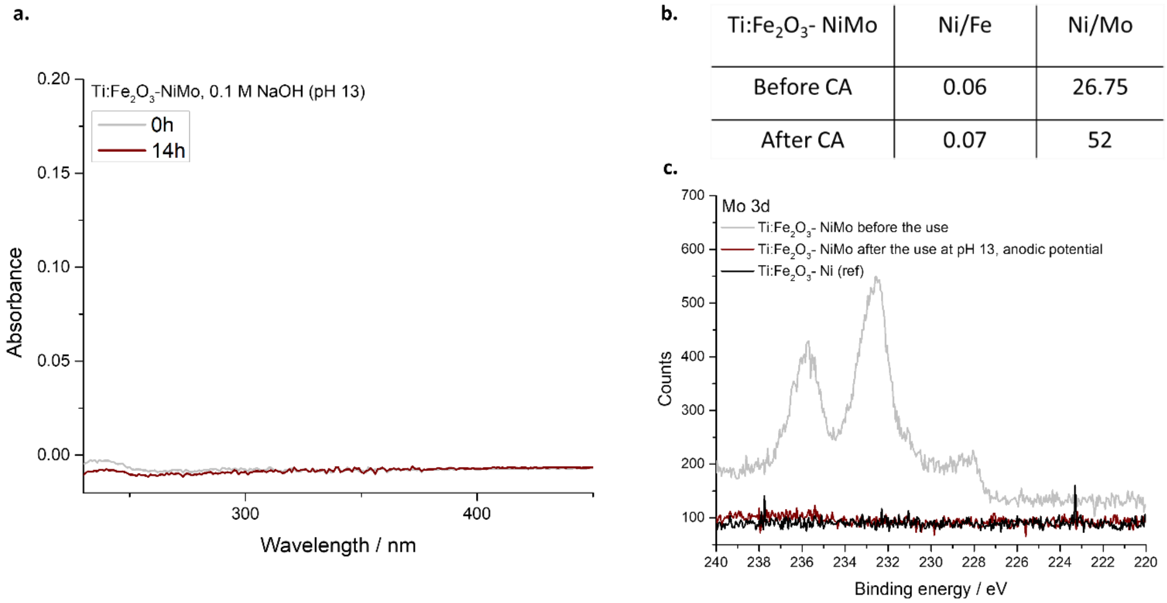

Ti:Fe$_2$O$_3$- NiMo	Ni/Fe	Ni/Mo
Before CA	0.06	26.75
After CA	0.07	52

Figure 9.7 *Ti:Fe$_2$O$_3$-NiMo in a two compartments PEC cell without HMF, pulsed chronoamperometry (CA) at 1.4V vs RHE.* ***(a)*** *absorption spectra at 0h (grey line) and at the end of the measurement (dark red line);* ***(b)*** *EDX analysis before and after the CA: Ni/Fe and Ni/Mo were calculated considering the Ni, Fe and Mo atomic percentages, by averaging them in different regions of the sample's surface;* ***(c)*** *comparison of the Mo 3d XPS spectra for three different samples: Ti:Fe$_2$O$_3$-NiMo before the CA (grey line); Ti:Fe$_2$O$_3$-NiMo after the CA (dark red line) and Ti:Fe$_2$O$_3$-Ni taken as the reference (black line).*

A significant HMF instability in highly alkaline solutions was also observed, explaining the presence of unidentified by-products during prolonged photoelectrolysis experiments (see *Section 9.4.1* for further details). However, ensuring a high concentration of OH^- in the electrolyte is essential for effective HMF PEC oxidation in the presence of Ni-based co-catalysts[150]. To corroborate this, additional HMF photoconversion experiments were performed with Ti:Fe$_2$O$_3$-NiMo and Ti:Fe$_2$O$_3$-Ni photoanodes in different electrolytes, such as 0.25M borate buffer and phosphate buffer, and at milder pHs 9 and 11.5. Pulsed CAs were conducted at potentials equal to 1.6V and 1.3V vs RHE, respectively. Samples were taken at the beginning and at the end of the measurements for a spectro-photometric product analysis. In all cases, no HMF conversion was observed, and no absorbing species were detected in the visible region of the spectra (Figure 9.8).

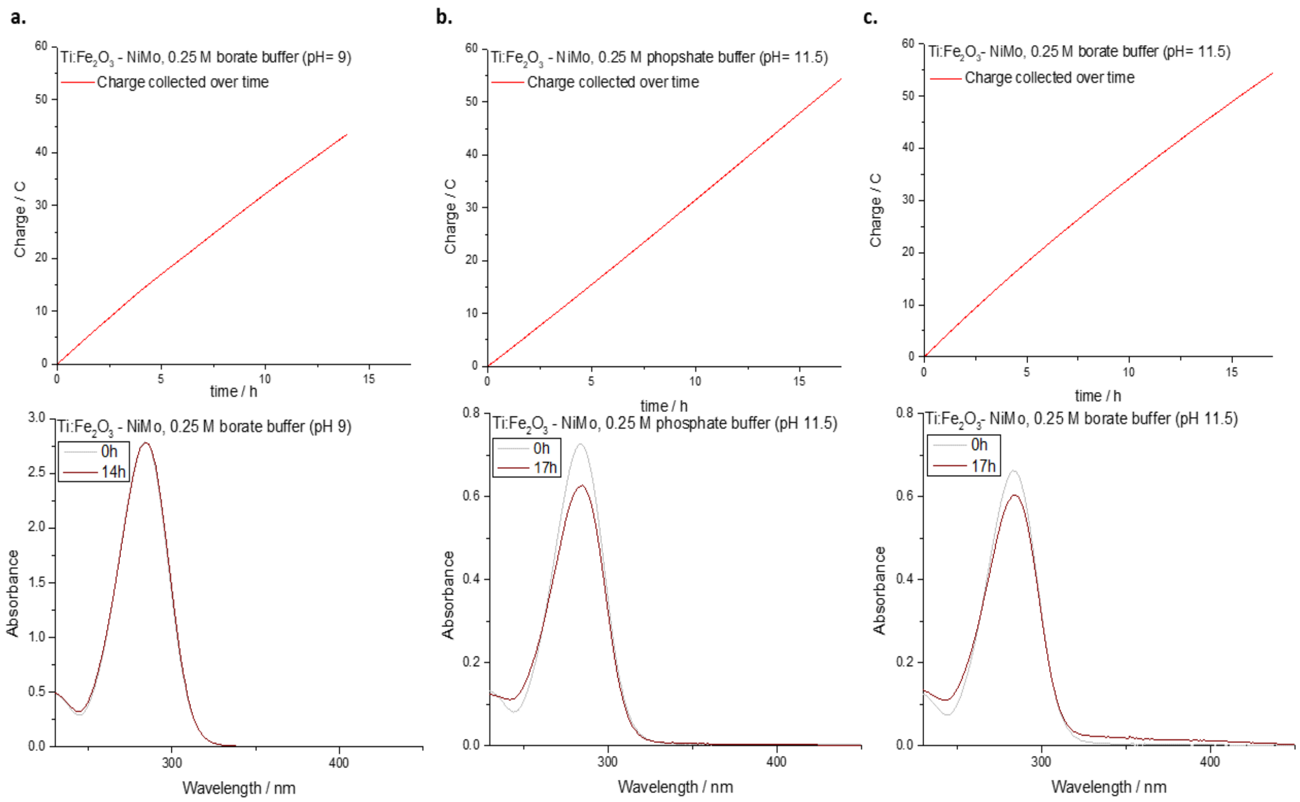

Figure 9.8 *On the top: charge collected during the pulsed CA; at the bottom: normalized absorption spectra.* ***(a)*** *CA at 1.6V vs RHE in 0.25 M borate buffer (pH 9); CA at 1.3V vs RHE in* ***(b)*** *0.25 M phosphate buffer (pH 11.5);* ***(c)*** *0.25 M borate buffer (pH 11.5).*

Overall, both Ti:Fe_2O_3-Ni and Ti:Fe_2O_3-NiMo photoanodes enabled the PEC oxidation of HMF to FDCA with good yields. However, the highly alkaline conditions employed significantly hinder full conversion to FDCA. Typically, elevated temperatures and low concentrations of base and substrate tend to favour HMF degradation into humins. If part of the starting compound undergoes this side-reaction, a reduced amount will be available to interact with nickel-based co-catalysts, reducing its conversion to FDCA in the PEC process. Of course, increasing the photocurrent could improve the efficiency of turning HMF into FDCA, but it would also imply that the degradation of HMF might happen at a similar rate. In the future, optimizing conditions like temperature, base, and substrate concentrations could steer the synthetic pathway toward Cannizzaro compounds[103,104]. Such adjustments would better leverage the HMF efficient hole scavenging on nickel-modified Ti-doped hematite photoanodes, thereby improving FDCA production.

9.3 X-ray spectro-electrochemical analysis

Fixed-energy X-ray Absorption Voltammetry (FEXRAV) experiments for Ti:Fe_2O_3-NiMo and Ti:Fe_2O_3-Ni were carried out to monitor the Ni K-edge chemical shift *operando* as a function of the applied potential (more details about the technique can be found in *Chapter 6, Section 6.4.1*). Figure 9.9 reports the variation of the normalized Ni K_α fluorescence I_{fluo} (proportional to the x-ray absorption coefficient μ) upon potential sweeping and 6.6mM HMF addition.

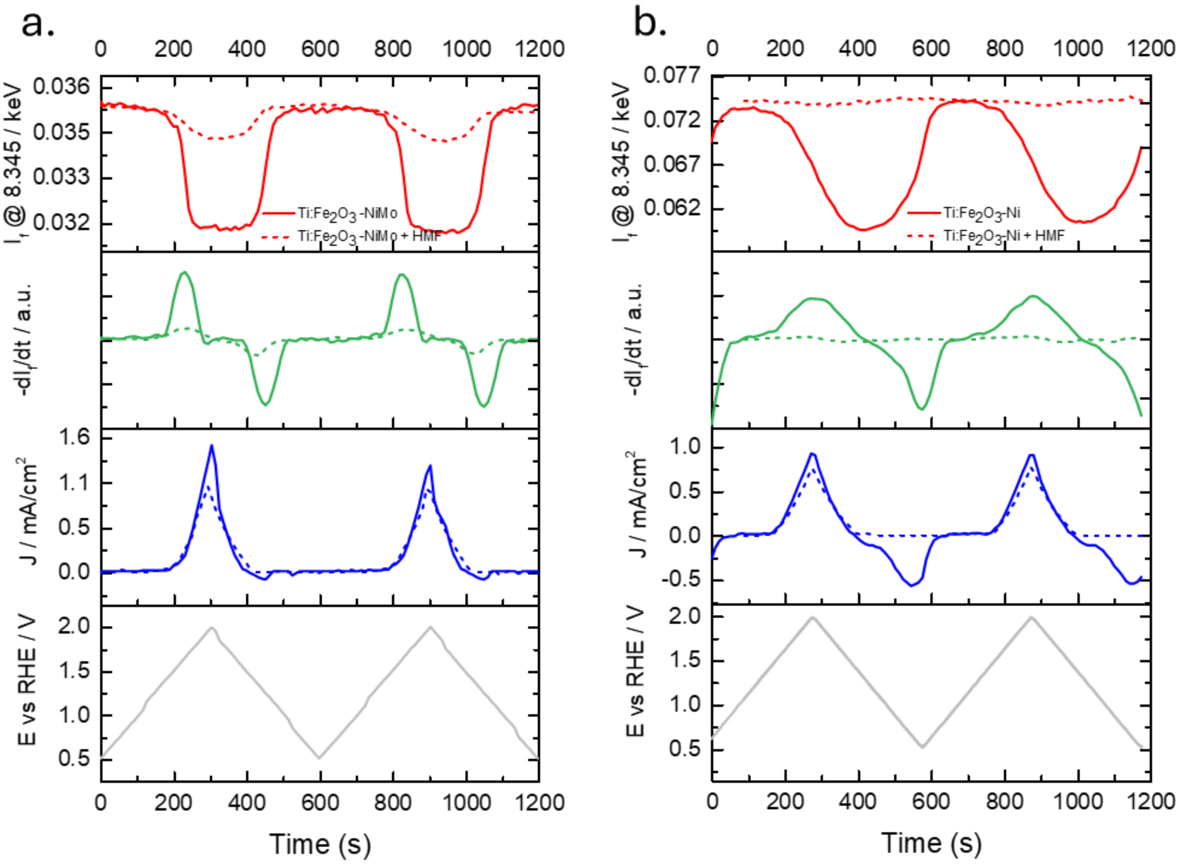

***Figure 9.9** FEXRAV signal recorded in function of time during two consecutive cyclic voltammetries for **(a)** Ti: Fe2O3-NiMo and **(b)** Ti: Fe2O3-Ni (red line). For both samples, measurements were performed with and without the addition of HMF (dashed and continuous line, respectively). The green line is the derivative of the FEXRAV signal, to be directly compared to the current recorded by the potentiostat during the voltammetries (blue line).*

The derivative -dI_{fluo}/dt as a function of the potential is reported in Figure 9.10a and b, respectively for Ti:Fe_2O_3-NiMo and Ti:Fe_2O_3-Ni.

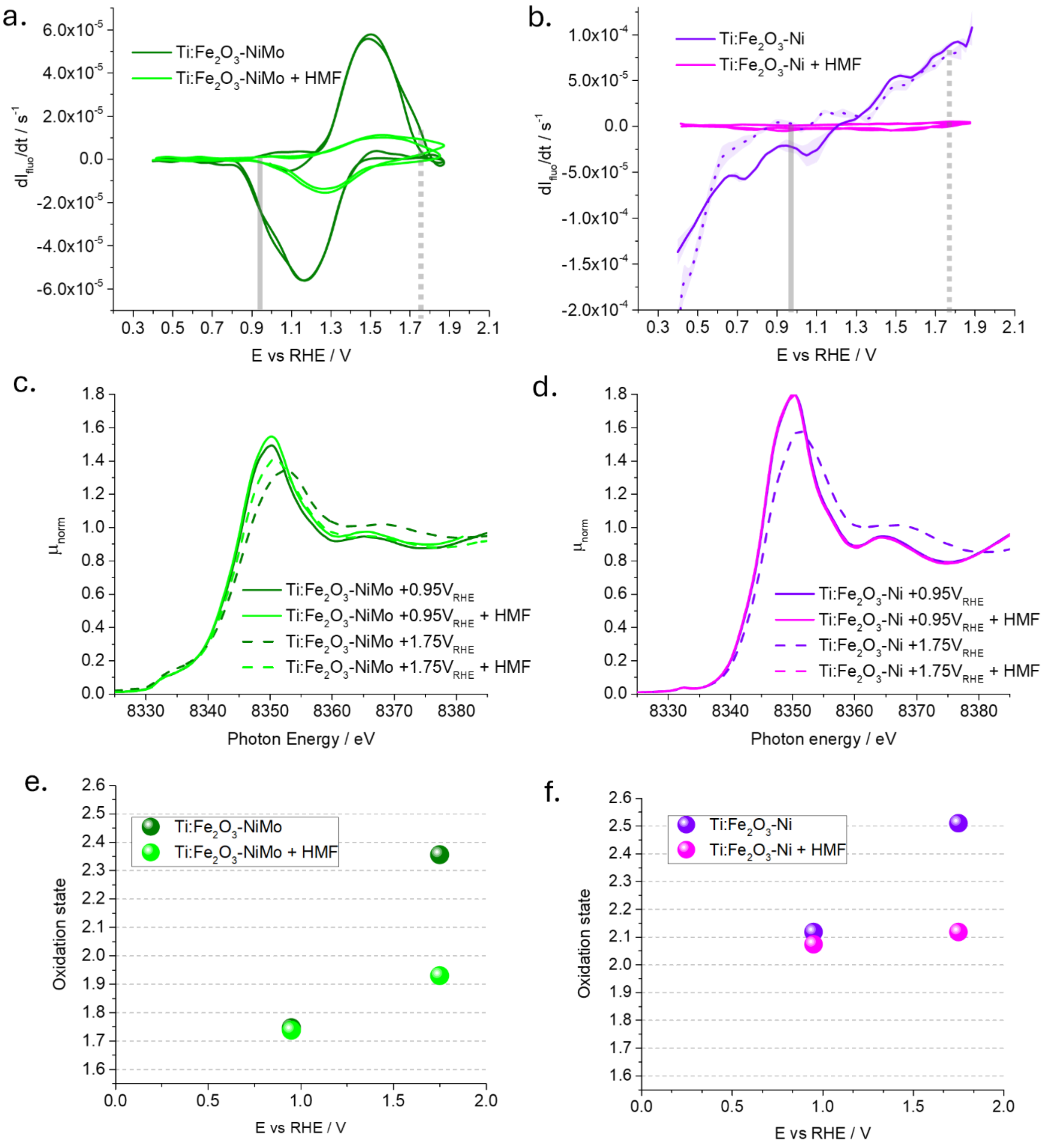

***Figure 9.10** X-ray spectro-electrochemical characterization of Ti:Fe_2O_3-NiMo (green) and Ti:Fe_2O_3-Ni (violet) photoanodes before (solid line) and after (dotted line) the addition of HMF to the electrolyte. **(a, b)** derivative of the FEXRAV signal registered at fluorescence energy equal to 8345 eV, before and after HMF addition. The anodic sweep in Fig. b is reported as a dotted line to highlight the hysteresis with the cathodic sweep. **(c, d)** XANES Ni α-edge spectra at selected potentials, highlighted in the FEXRAV analysis as solid and dashed grey markers. **(e, f)** Corresponding oxidation states obtained by calibration with standards, applying the integral method for a reliable definition of the absorption edge energy.*

By comparing the voltammetry for Ti:Fe_2O_3-NiMo in the absence of HMF and illumination (Figure 9.1a, dotted line) to the x-ray spectro-electrochemical FEXRAV plot in Figure 9.10a, we can recognize the reversible Ni^{2+}/Ni^{3+} wave, centred at E^{eq}= +1.4V vs RHE. Unlike ciclyc voltammetry, FEXRAV provides element-selective information on the potential-dependent variation of the oxidation state of the co-catalyst, complementary to the information provided by conventional voltammetry[158]. Indeed, upon addition of HMF, the wave strongly dampens in intensity, pointing out that a smaller variation of Ni oxidation state occurs in this case, due to quenching of Ni(III) states by HMF acting as an electron donor. This is to be contrasted with conventional voltammetry, where the same mechanism, i.e. electrochemical oxidation of HMF at the expense of Ni(III), leads to a catalytic amplification of the anodic current. This points out that HMF acts as a hole scavenger for the NiMo layer. A similar behaviour is observed on Ti:Fe_2O_3-Ni, despite the broadened waves and the lack of a sharp reversible wave for this photoanode.

Further, XANES spectra were measured at selected potentials of +0.95 V and +1.75V vs RHE, to confirm the chemical shift on the absorption edge: these are reported in Figure 9.10c-d for Ti:Fe_2O_3-NiMo and Ti:Fe_2O_3-Ni with and without HMF addition.

For both samples, at +0.95V vs RHE the XANES spectra are unaltered after the addition of HMF, indicating that no spontaneous process occurs in this potential region. Figure 9.10e-f display the nominal oxidation state determined from the x-ray absorption edge energy by means of the integral method and calibration curve, as explained in Figure 9.11. The oxidation state of the Ni site is $Ni^{+1.75}$ and $Ni^{+2.12}$ for NiMo and Ni electrocatalysts, respectively. Thus, Ni is oxidised when being exposed to the electrolyte, and the extent of the oxidation process is slightly lower when Ni is coupled to Mo, suggesting a partial polarisation of electron density from molybdenum to nickel. When the potential is set to +1.75V vs RHE in the Ti:Fe_2O_3-NiMo sample, the spectrum is blue-shifted due to the chemical shift induced by the electrochemical oxidation process. The corresponding oxidation state is increased to $Ni^{+2.35}$ and $Ni^{+2.52}$ for Ti:Fe_2O_3-NiMo and Ti:Fe_2O_3-Ni, respectively. Upon addition of HMF, the process is either partially or fully reversed, with the oxidation state being reduced to $Ni^{+1.92}$ and $Ni^{+2.12}$, respectively, highlighting the strong selectivity of these photoanodes towards HMF oxidation. In the steady state at +1.75V, the holes stored in the Ni co-catalyst layer are swiftly scavenged by HMF, resulting in a return of Ni to the low oxidation state. This finding corroborates the suppression of the reductive peak observed in the dark CVs for both Ti:Fe_2O_3-NiMo and Ti:Fe_2O_3-Ni photoanodes (Figure 9.1a and b). Notably, this prompt transfer of holes occurs at potentials where a strong competition with water oxidation is expected. Therefore, when Ni-based electrocatalysts are present on the photoanode’s surface, the HMF’s holes scavenging capability is maximized. This prevents the need for an electron mediator to facilitate HMF oxidation and mitigates issues associated with competition from water oxidation.

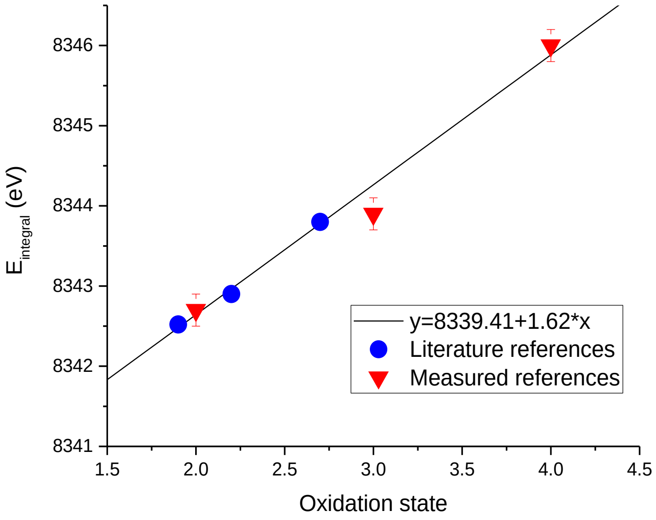

Figure 9.11 Edge position by integration of the absorption edge for selected reference samples with linear calibration 1.62 ± 0.05 eV/Ox.State + 8339.41 ± 0.18 eV (red triangles). The used references were NiO, NiOOH, and $KNiIO_6$*. Literature reference values for Ni-based electrocatalysts in operando conditions was reported for comparison.*[159].

Finally, we would like to point out that the oxidation state from XAS measurements is determined by averaging across all the Ni atoms present on the sample's surface. Therefore, this knowledge cannot be used to define the reaction mechanism in a dynamic fashion. Additionally, HPLC data were collected only at the beginning and at the end of the experiment, providing no information about intermediate products. Although the precise oxidation mechanism remains unclear, operando XAS has revealed rapid charge transfer between Ni-based catalysts and HMF, suggesting that the rate-determining step is likely unrelated to the charge transfer between the two (as instead shown in *Scheme 9.1*, process 3 and *Scheme 9.2*, processes 4-5).

In this study, titanium-doped hematite photoanodes, i.e. Ti:Fe_2O_3-NiMo and Ti:Fe_2O_3-Ni, were employed for the first time to photoelectrochemically oxidize HMF to FDCA, without the need for electron mediator. In the previous chapter, it was shown that such results were unattainable using the same Ti:Fe_2O_3 modified with cobalt-based co-catalysts (e.g., CoPi or $CoFeO_x$). Comprehensive photoelectrochemical characterization and XAS measurements highlighted the remarkable selectivity of these photoanodes for HMF oxidation over water oxidation, thanks to a strong hole scavenging effect. Because of the alkaline conditions employed, the oxidation process to FDCA was not fully completed and some by-products were generated. An in-depth investigation of these by-products formation identified key challenges in the conversion process, providing important insights for future optimization efforts. In *Section 9.4* further details about the spectro-photometric characterization are presented.

9.4 Spectro-photometric characterization during HMF PEC conversion

Besides HPLC chromatography, it was possible to follow the HMF PEC conversion by means of spectro-photometry. HMF and its oxidative intermediates, i.e., DFF, HMFCA, FFCA and FDCA, are characterised by the following absorption spectra:

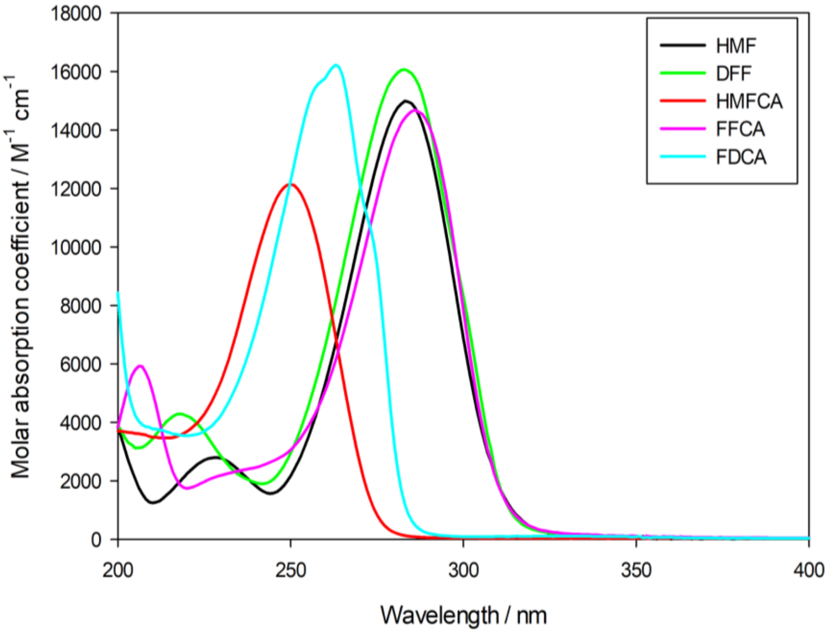

Figure 9.12 *Molar absorption coefficients (M^{-1}cm^{-1}) of standard HMF and its oxidative intermediates as a function of the wavelength (nm). The spectra were acquired in a borate buffer solution (0.25M, pH 9.2).*

As shown in Figure 9.12, FFCA and DFF absorb in a similar region as the starting compound, with absorption maxima close to that of HMF, which is located at 283 nm. In contrast, FDCA's absorption spectrum is blue shifted, with a peak around 263 nm, and characterised by a distinct shape. While this technique does not permit quantitative analysis, it provides a qualitative indication of the PEC conversion, offering an initial understanding of the trends and results (Figure 9.13).

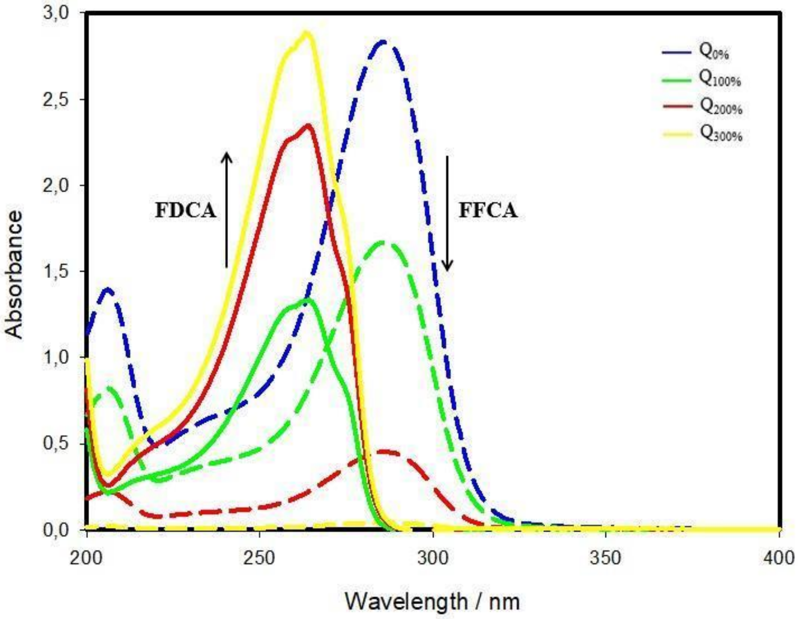

Figure 9.13 *Evolution of the absorption spectra of FFCA (dashed lines) and FDCA (solid lines) during the PEC experiment performed with Ti:*Fe_2O_3*-CoPi photoanode. The spectra for the* $Q_{0\%}$ *(blue),* $Q_{100\%}$ *(green),* $Q_{200\%}$ *(red) and* $Q_{300\%}$ *(yellow) samples, were acquired in a borate buffer solution (0.25M, pH 9.2) after a dilution of 1:36.*

9.4.1 Stability tests

With spectro-photometry it was also possible to investigate the stability of the solutions containing the biomasses. To this purpose, model samples with known concentration of HMF, DFF, FFCA or FDCA were prepared in the same conditions as the real samples (~mM in NaOH 0.1M) and stocked at 4°C. The stability of the samples in the experimental conditions was then evaluated *via* absorption spectra recorded at time intervals of 24h for 5 days. From this analysis, variation in the absorption spectra were appreciated only for HMF and DFF, whereas those of FDCA and FFCA were maintained. As widely reported in literature, these trials confirm the poor stability of HMF at high pH levels and demonstrate the durability of its oxidation product, FDCA, in basic conditions.

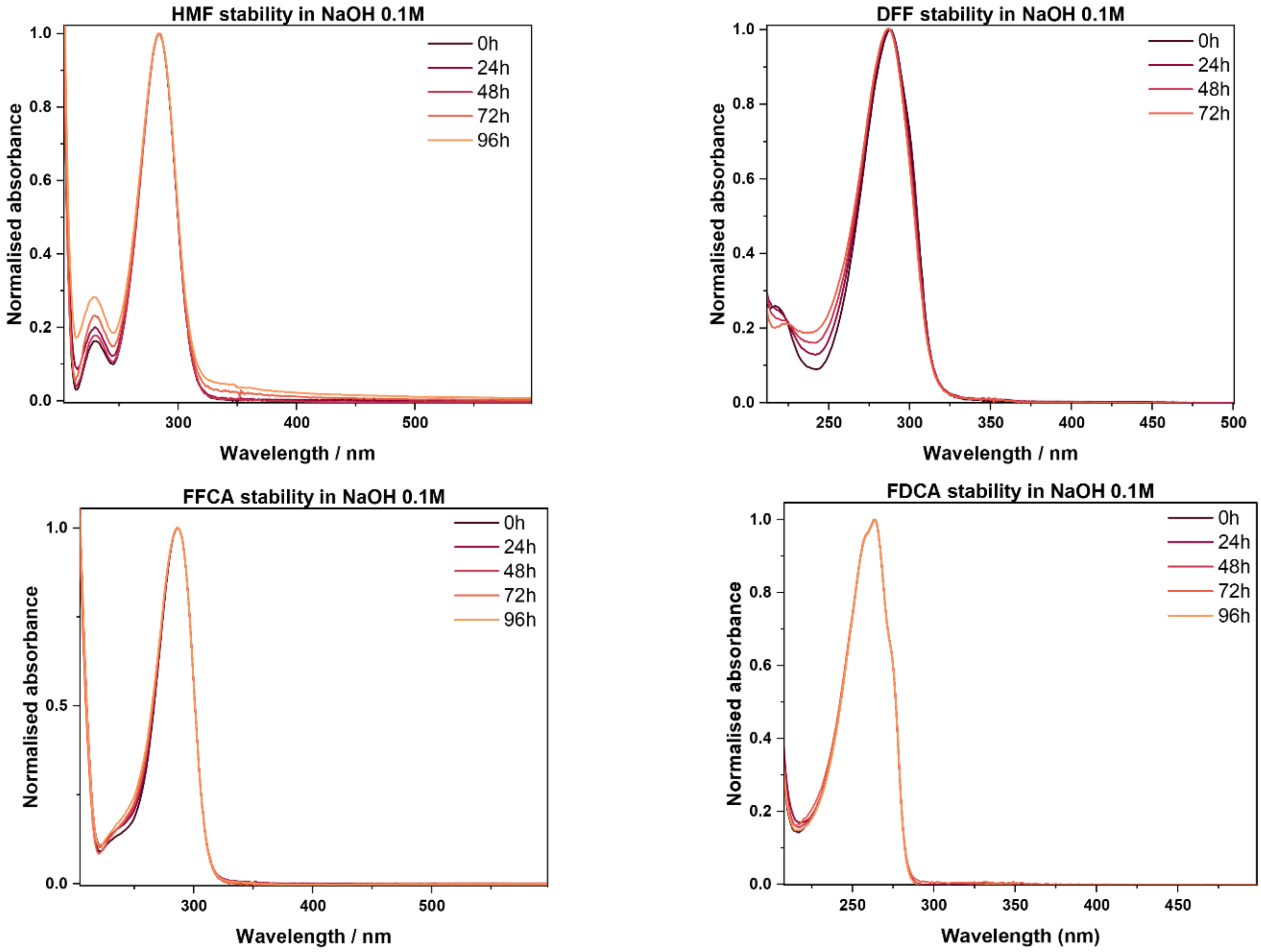

Figure 9.14 *Normalized absorbance of HMF, DFF, FFCA as a function of the wavelength. Stability tests performed in 0.1 M NaOH (pH 13), by acquiring absorption spectra at 0, 24, 48, 72 and 96 hours of the standards.*

9.4.2 Fitting equation

As explained in *Section 9.2*, Since neither DFF nor HMFCA were detected by High Performance Liquid Chromatography, the absorption spectra of the solution sampled at the start and at the end of the pulsed CA were fit by a linear combination of FFCA and FDCA reference spectra. Therefore, the fitting function was $ab = C1 \cdot a + C2 \cdot b$, where ab is the dependent variable, i.e. the final spectrum obtained out of the fitting; a, b are the independent variables, i.e. the absorption spectra of the standards considered; and $C1$, $C2$ are the contributions of each standard to ab. The coefficient $C2$ quantifies the sum of FFCA and HMF, which is still present in the reaction mixture. The relative contribution of FDCA (%) to the final absorption spectra was calculated from the best fit coefficients according to:

$$\%FDCA_{fit} = \frac{C2}{C1 + C2} \cdot 100 \quad (9.1)$$

Instead, the FDCA relative conversion coefficient (%) from the HPLC data was determined as follows:

$$\% \, FDCA_{HPLC} = \frac{FDCA \; conversion \; (\%)}{HMF \; residual + \; FDCA + FFCA \; (\%)} \cdot \; 100 \qquad (9.2)$$

where FDCA and FFCA conversion percentages (%) and HMF residual (%) are calculated from the HPLC spectra. The next chapter explores another PEC biomass valorisation process using $BiVO_4$ as the photoanode.

10. Boosting stability of nanoporous $BiVO_4$ photoanodes for PEC glycerol oxidation through current modulation

In this study, a straightforward operational approach is introduced to boost the performance and stability of $BiVO_4$ photoanode under long-term PEC conversion. Rather than modifying the semiconductor surface or composition, long-term chrono-potentiometric (CP) measurements were performed with either a fixed or modulated current over time. In the “continuous working mode", a constant current was applied during the experiment, following the traditional procedure widely employed in literature. In the “modulated” one, the same current of the previous case was maintained for 60s and then turned off for 5s: this on/off cycle was repeated until the same charge as the continuous mode experiment was reached. The effects of these CP measurements on the semiconductor’s photoelectrochemical properties and morphology were evaluated for two anodic reactions: the traditional oxygen evolution reaction (OER) and the glycerol oxidation reaction (GOR). While the OER has been extensively studied for PEC water splitting, it faces significant thermodynamic and kinetic challenges. In contrast, GOR offers a compelling alternative, producing valuable oxidative intermediates—such as dihydroxyacetone (DHA) and glyceraldehyde (GLAD)—with several applications in the cosmetic and pharmaceuticals fields (as explained in *Chapter 5*). In both cases, a 0.5M $NaNO_3$ solution (pH 2) was employed, as it was reported to be the best electrolyte for $BiVO_4$ photoanodes, in terms of stability and performance[134]. High-surface area, nanoporous $BiVO_4$ were synthesised via electrodeposition following the procedure described in *Section 7.1*. The experiments were performed in a flow PEC cell at a constant flux rate of (20mL/min) collecting the cell temperature over time. Besides the potential measured at the photoanode surface (E vs RHE, i.e. the Reference Hydrogen Electrode), the potential difference between the counter and the working electrode was also monitored over time, which will be referred to as cell voltage. This quantity indicates the voltage needed to polarise the working electrode in response to the feedback loop and can be affected by the resistance of the electrolyte and by the overpotential of a specific anodic reaction. The triggering factors for the overpotential are interface phenomena, such as mass transport, and charge transfer limitations. As we are in flow conditions, we can consider the flux rate to be sufficiently high that the thickness of the diffusion layer is minimised. Consequently, no problems of mass transport should arise, with the species to be oxidised easily reaching the holes generated at the electrode’s surface. Therefore, an eventual increase in the cell voltage should be ascribed to charge transfer limitations only, which lead to holes accumulation at the interface and thus enhance surface recombination and photo-corrosion. Interestingly, by acquiring chopped LSV before and after the long-term CPs, it could be possible to see how the working and the cell voltage variations influenced the photocurrent, as well as the overall photoelectrode performance. Additional structural and morphological analyses allowed for a comprehensive understanding of samples behaviour.

10.1 Oxygen Evolution Reaction (OER)

The first case study focused on water oxidation reaction, the long-standing bottleneck in overall PEC water splitting. Long-term CPs were conducted by maintaining a current density of 1 mA cm^{-2} for 8 hours, reaching a total charge of 28.7 $C \cdot cm^{-2}$. In Figure 10.1, the differences between the modulated and the continuous working mode are shown. While the trends of the potential at the photoanode surface are similar (Figure 10.1a and b), the cell voltage behaves differently, with the continuous experiment exhibiting a steady increase over time (Figure 10.1d). From the chopped LSV, a general increase in photocurrent is observed after the modulated mode (Figure 10.1e), whereas the continuous mode leads to a significant photocurrent decline at higher potentials, accompanied by pronounced recombination spikes at lower voltages (Figure 10.1f).

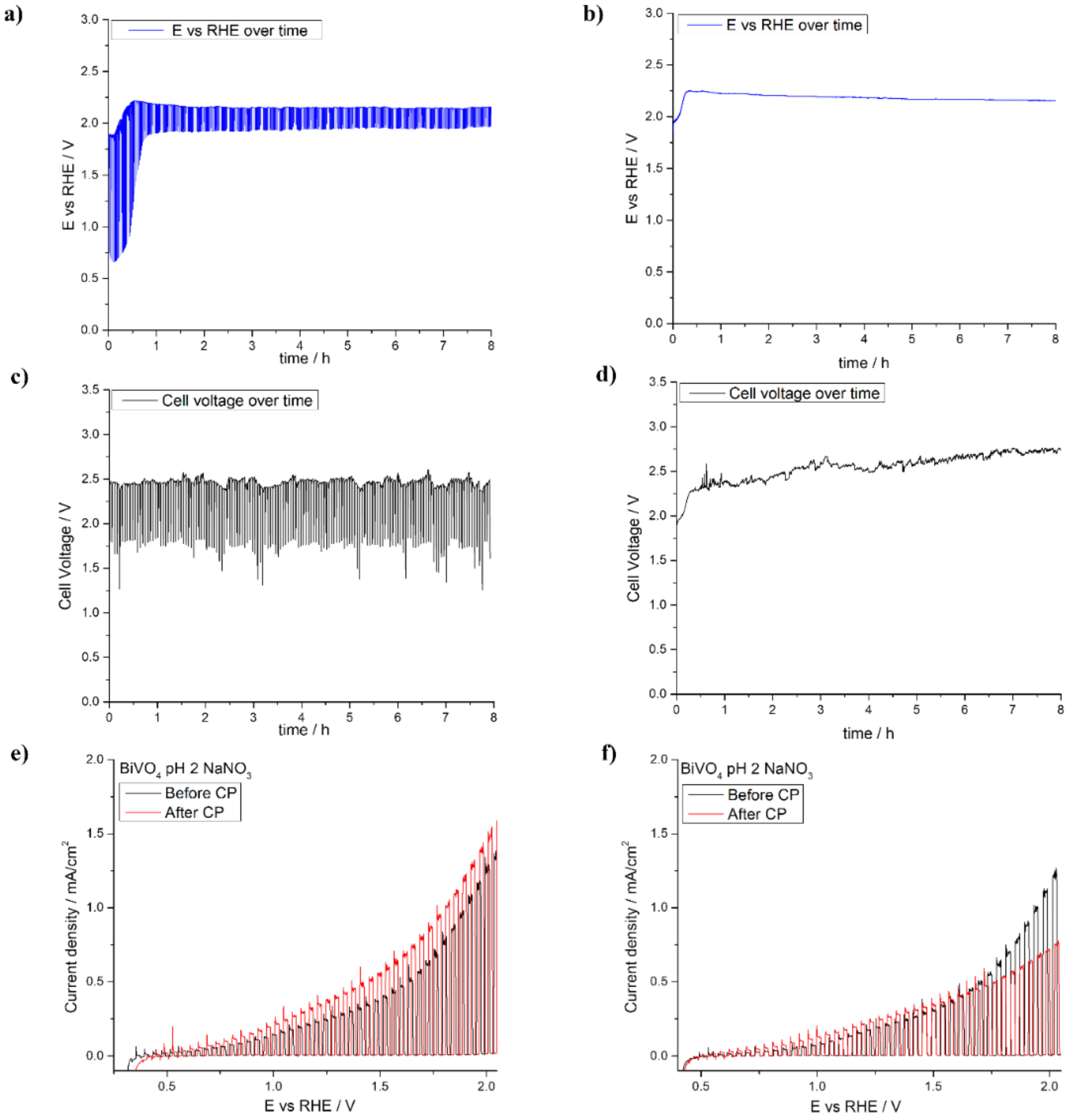

Figure 10.1 *Modulated (left) and continuous (right) chrono-potentiometry for OER at pH 2, with* $BiVO_4$ *photoanode in a flow PEC cell.* ***(a, b)*** *Voltage measured at the photoanode surface (E vs RHE) over time;* ***(c, d)*** *Cell voltage (V) over time;* ***(e, f)*** *Chopped LSVs before (black) and after (red) the chronopotentiometry.*

SEM images revealed the formation of flat zones and aggregates on the sample surface after the continuous CP (Figure 10.2a). Instead, the sample after the modulated experiment (Figure 10.2b) retains the reference morphology (reported in *Chapter 7*, Figure 7.1a), preserving its original structure.

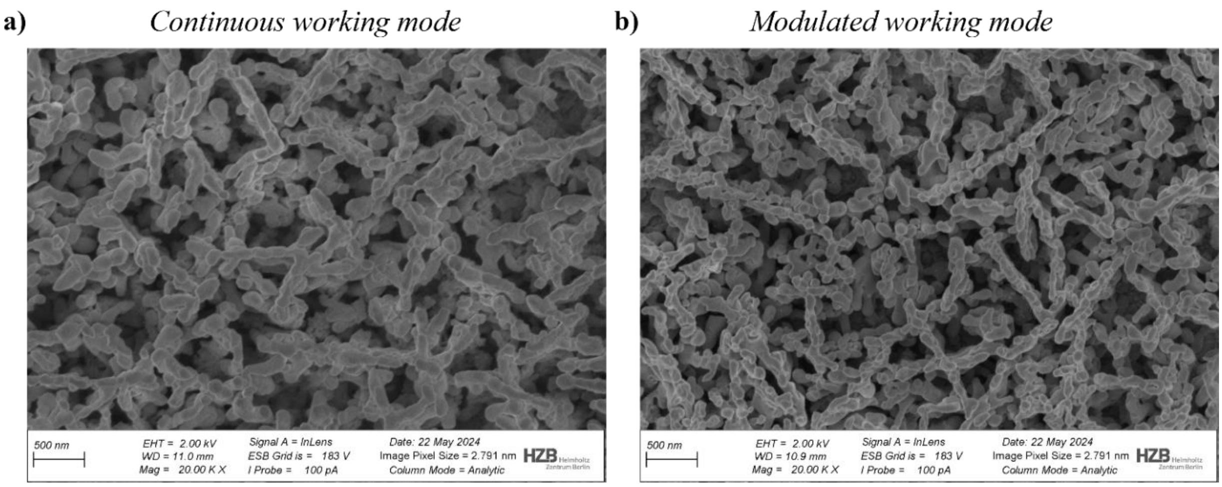

Figure 10.2 *Planar characterization of a $BiVO_4$ photoanode morphology by SEM analysis after* ***(a)*** *continuous and* ***(b)*** *modulated CP at pH 2.*

Although water is not a selective species for the $BiVO_4$ surface holes, this preliminary study reveals clear differences between the two operating modes, with the modulated one demonstrating promising results in enhancing photoanode's performance and preserving interfacial morphology. To further investigate this effect, we move to a more relevant anodic reaction, GOR, involving as reactant a well-established hole-selective contact for $BiVO_4$ photoanode.

10.2 Glycerol Oxidation Reaction (GOR)

Upon adding glycerol to the electrolyte, a significant increase in photocurrent is observed across the entire potential range, with the onset shifting toward lower potentials (Figure 10.3). This suggests that glycerol scavenges holes more selectively than water, supporting previous findings on $BiVO_4$ photoanodes under similar acidic conditions[114].

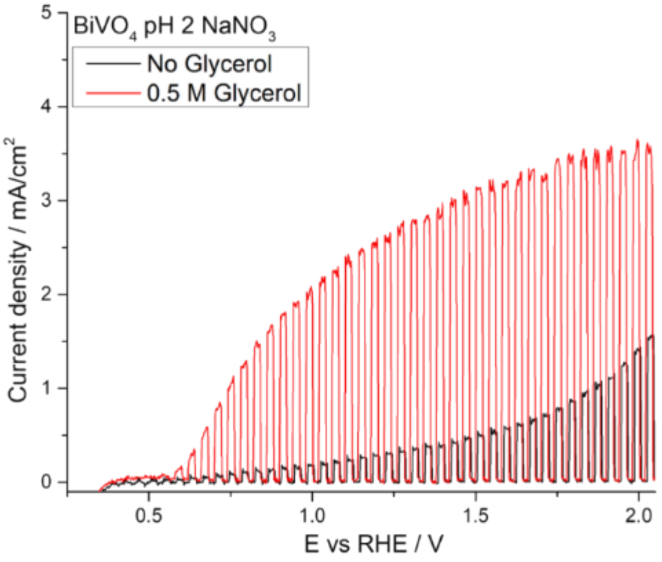

Figure 10.3 *Chopped LSVs before (black) and after (red) the addition of 0.5M glycerol to the electrolyte.*

Long-term CPs were collected by fixing a current density of 2 mA cm^{-2} for 8 hours, until a charge of 52.4 C·cm^{-2} was reached. Then, a chopped LSV was acquired, and the CPs were started again for a total time of 12 hours, attaining a final charge of 79.7 C·cm^{-2}. Samples were taken at the beginning and at the end of the experiment for HPLC analysis.

In the modulated CP, both the cell and the photoanode potential remain quite stable and, as the experiment evolves, a lower potential is needed to maintain a constant current density of 2 mA cm^{-2} (Figure 10.4a and b). From the chopped LSVs, a substantial photocurrent increase in the entire potential range is observed over time, reaching good photocurrent values already at low potentials, e.g., as illustrated in Figure 10.4c, a cathodic shift (ΔV_{ph}) of 0.13V is recorded to achieve a photocurrent density of 2 mA cm^{-2}.

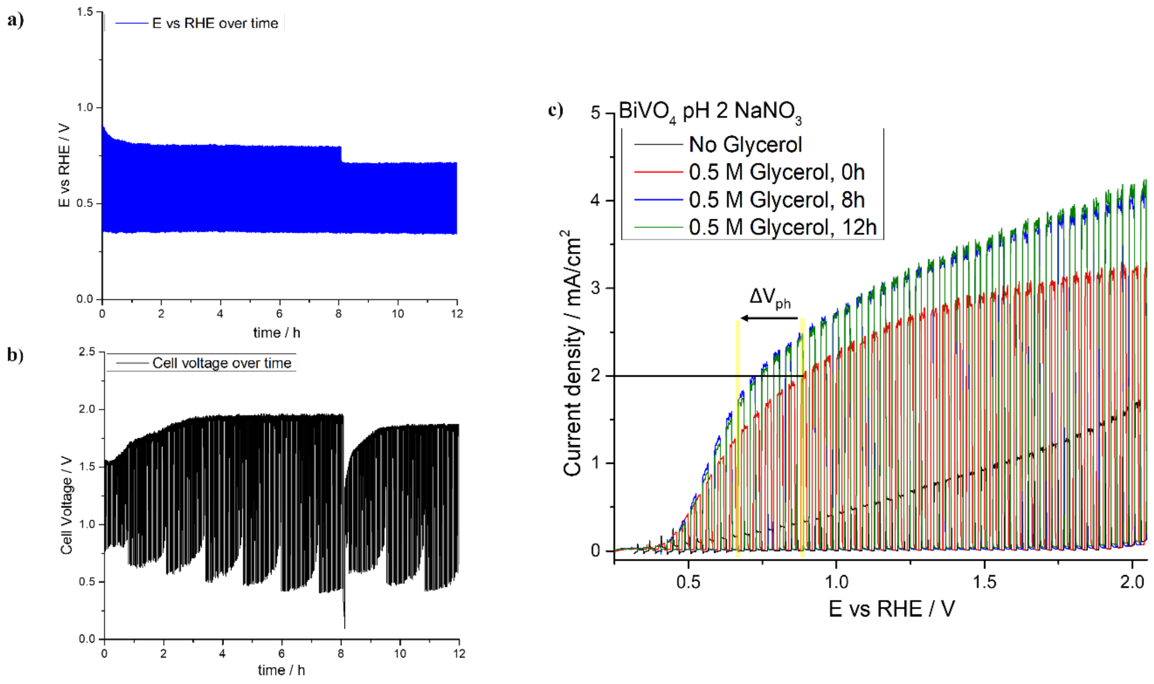

Figure 10.4 *Pulsed chrono-potentiometry at pH 2 with 0.5M glycerol, using BiVO$_4$ photoanode in a flow PEC cell.* ***(a)*** *Voltage measured at the photoanode surface (E vs RHE) over time,* ***(b)*** *Cell voltage (V) over time,* ***(c)*** *Chopped LSVs acquired over time: No glycerol (black), 0.5M glycerol 0h (red), 0.5M glycerol 8h (blue) and 0.5M glycerol 12h (green).*

On the contrary, in the continuous CP, both the photoanode surface potential and the cell voltage keep rising over time (Figure 10.5a and b), and the chopped LSVs show no improvement in photocurrent throughout the measurement (Figure 10.5c).

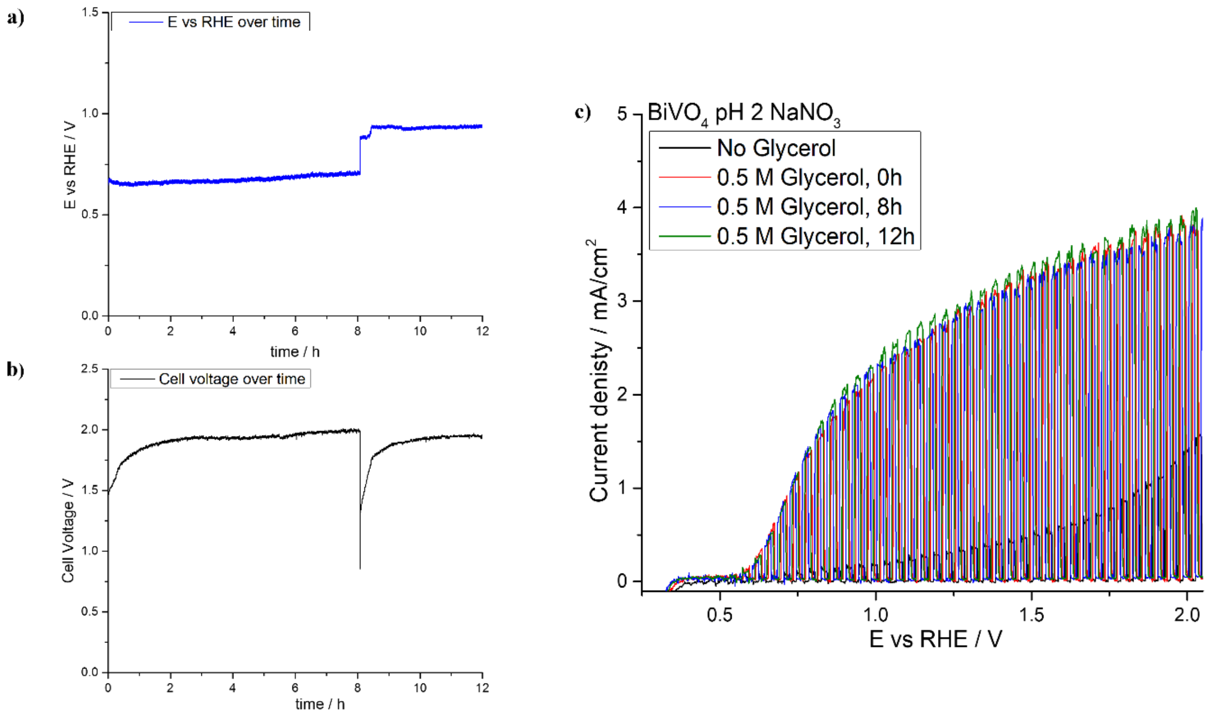

Figure 10.5 *Continuous chrono-potentiometry at pH 2 with 0.5M glycerol, using* $BiVO_4$ *photoanode in a flow PEC cell.* ***(a)*** *Voltage measured at the photoanode surface (E vs RHE) over time,* ***(b)*** *Cell voltage (V) over time,* ***(c)*** *Chopped LSVs acquired over time: No glycerol (black), 0.5M glycerol 0h (red), 0.5M glycerol 8h (blue) and 0.5M glycerol 12h (green).*

Table 10.1 summarises and compares the results obtained from the continuous and the modulated CPs for GOR.

Experiment	ΔV_{el} (V)	ΔV_{cell} (V)	ΔJ (mA/cm^2) at 1.23 vs RHE
GOR modulated	-0.09	+0.09	+0.53
GOR continuous	+0.27	+0.12	0

ΔV_{el} represents the difference between the final and initial voltage measured at the photoanode surface, ΔV_{cell} indicates the difference in cell voltage, and ΔJ reflects the variation in photocurrent density at 1.23V vs RHE throughout the measurement. Note that ΔV_{el} and ΔV_{cell} are calculated by first averaging the voltage values over the initial and final time intervals of the measurement, and then by subtracting the averaged values. While ΔV_{el} decreases in the modulated experiment and increases during continuous operation, ΔV_{cell} rises in both cases, with a more pronounced increase observed in the continuous mode experiment. Notably, under continuous operation, restarting the CP leads to a sharp rise in potential (Figure 10.5a and b), resulting in final voltage increases of ΔV_{el}= 270mV and ΔV_{cell}= 120mV (*Table 10.1*, second row). In the modulated experiment (Figure 10.4a and b), minor potential variations are also observed at the relaunching of the CP, though without significant changes in the final voltage values (*Table 10.1*, first row). Overall, the voltage stability achieved during the modulated experiment leads to a significant improvement in photocurrent, ΔJ, a benefit that is not observed under continuous operation.

The remarkable difference between the continuous and the modulated experiments, can be explained by assigning a beneficial hole scavenging effect to the modulated working mode, which further enhances the excellent hole capturing capability of glycerol. By periodically applying zero current for a few seconds, the electrode surface discharges, preventing hole accumulation over time. This reduces electron-hole recombination and, once the current is restored, it ensures a more effective utilisation of the surface-reaching holes for glycerol oxidation reaction. As a result, the photocurrent increases and lower voltage is required for the anodic reaction (Figure 10.4c and Table 10.1, first row). Without these restorative on/off cycles, as in the continuous mode, holes accumulate at the interface and are more likely to recombine with bulk electrons. As a result, fewer holes are available for the oxidising species, increasing the voltage demand for GOR and leading to stagnant photocurrent values (Figure 10.5c and Table 10.1, second row).

SEM images in Figure 10.6 show similar results as the OER experiments (Figure 10.2). Operating in continuous mode causes the photoelectrode to develop surface aggregates and flat regions on its surface (Figure 10.6a). In contrast, the sample used in modulated mode (Figure 10.6b) preserves its original morphology (*Chapter 7*, Figure 7.1 for the reference).

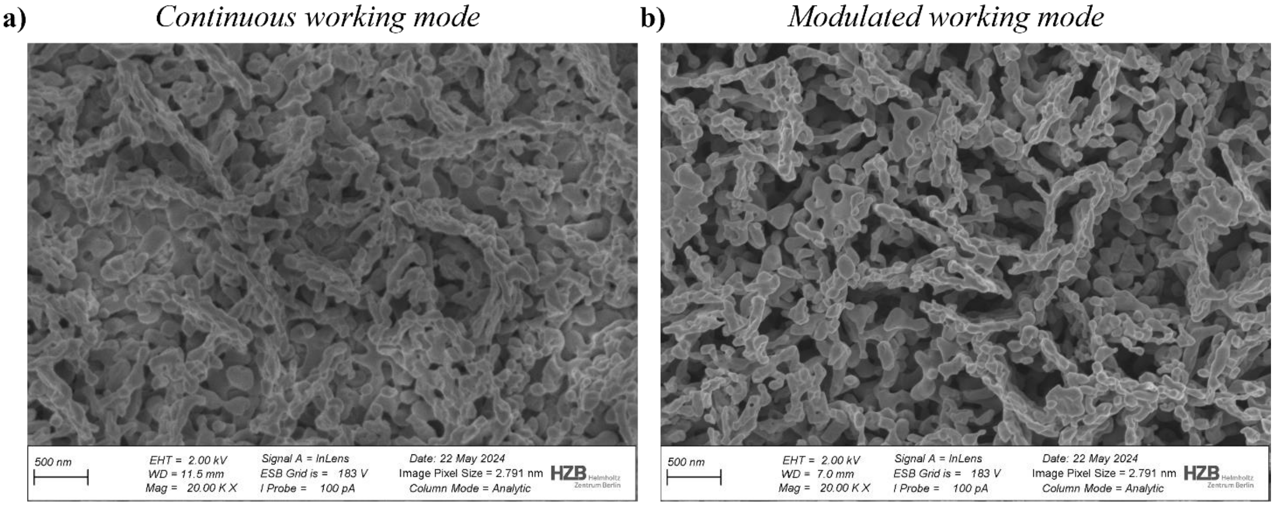

Figure 10.6 *Planar characterization of a $BiVO_4$ photoanode morphology by SEM analysis after* ***(a)*** *continuous and* ***(b)*** *modulated CP at pH 2 with 0.5M glycerol.*

XPS spectra of $BiVO_4$ photoanodes were collected following both modulated and continuous OER and GOR experiments (Figure 10.7). The integrated area ratios of the V $2p_{3/2}$ and Bi $4f_{7/2}$ peaks were then compared, to investigate whether differences in chemical composition emerged in addition to morphological changes. Notably, the ratio remains consistent between the modulated and continuous modes in both experiments (Figure 10.7d), indicating that the different operational mode did not affect the chemical composition of the $BiVO_4$ samples. The reduction in vanadium content following the GOR experiments can be attributed to the longer experiment duration (12 hours, compared to 8 hours for the OER).

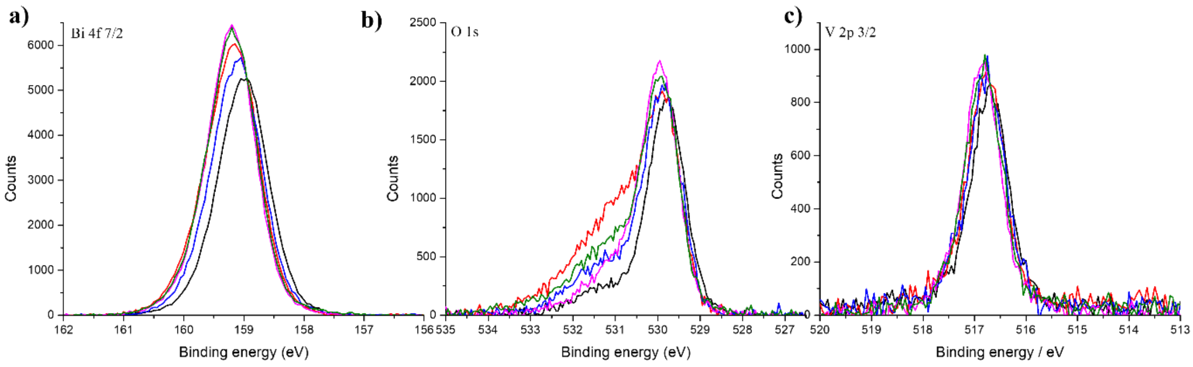

d)

Sample	A (V) / A (Bi)
BVO reference (not used)	0.17
Modulated CP (OER)	0.15
Continuous CP (OER)	0.15
Modulated CP (GOR)	0.14
Continuous CP (GOR)	0.14

Figure 10.7 *XPS spectra of* ***(a)*** *Bi 4f$_{7/2}$,* ***(b)*** *O 1s and* ***(c)*** *V 2p$_{3/2}$ core elements for $BiVO_4$ reference sample (black), after modulated CP for OER (red), after continuous CP for OER (blue), after modulated CP for GOR (pink) and after continuous CP for GOR (green).* ***(d)*** *Table showing the ratio of integrated areas between V 2p$_{3/2}$ and Bi 4f$_{7/2}$.*

The XPS spectra reveal a shift towards higher binding energies in the Bi 4f$_{7/2}$ and O 1s peaks compared to the reference (Figures 10.7a and 10.7b). This shift occurs as the core element interacts with oxidizing species, causing a slight positive charge and increasing the binding energy of remaining electrons. This effect is notably more pronounced in GOR samples, with the Bi 4f$_{7/2}$ peak shifting approximately 0.25 eV from its reference position at 158.95 eV. Consistent with prior studies[160], this finding suggests that glycerol promote electrode oxidation with a higher charge transfer kinetic than water, further highlighting $BiVO_4$ strong selectivity for glycerol oxidation over water oxidation (as also evident in the chopped LSV in Figure 10.3). Additionally, the shoulder around 531.5 eV in the O 1s peak can be attributed to -OH chemical states[160].

After the GOR experiments, HPLC analysis was performed, yielding similar results for both modulated and continuous experiments. The products included glycolaldehyde (GCAD), glyceraldehyde (GLAD), dihydroxyacetone (DHA), and Formic Acid (FA), with relative selectivity ($S_{\%}$) of 50%, 14%, 14%, and 20%, respectively.

This study presents a straightforward, practical method for using $BiVO_4$ photoanodes in long-term measurements, offering electrode regeneration and sustained stability over time. Modulating the current not only provides a stable, often enhanced, photocurrent response but also preserves the photoanode's morphology, significantly reducing photo-corrosion. While much research focuses on improving reaction selectivity in PEC glycerol oxidation with $BiVO_4$, ensuring the semiconductor durability is equally important for practical applications. Integrating this modulated operational approach with advanced methods to control product formation, will significantly enhance the performance and competitiveness of PEC devices. Moreover, as this method is particularly effective with strong hole-selective species for $BiVO_4$, it could be extended to other oxidation processes involving this photoanode.

Conclusions

This thesis investigates photoelectrochemical biomass valorisation as an oxidative semi-reaction in the anodic compartment of a PEC cell. Two biomass-derived intermediates, HMF and glycerol, were used as starting materials, and the choice of photoanode was based on its stability, photophysical properties, and photoelectrochemical performance in the reaction environment.

Ti:Fe_2O_3 photoanodes were employed for the HMF oxidation to FDCA with the conversion monitored via HPLC and spectro-photometric analysis. In the first case study, the reaction occurred in a mildly basic aqueous solution (pH 9.2) using TEMPO as a redox mediator. Ti:Fe_2O_3 photoanode was modified with $CoFeO_x$ and CoPi cocatalysts, and their performances were compared to that of the unmodified photoanode. CoPi significantly improved selectivity and Faradaic efficiency, achieving up to 86% yield of FDCA, whereas $CoFeO_x$ was less effective due to increased competition from OER. Electrochemical impedance spectroscopy (EIS) and intensity-modulated photocurrent spectroscopy (IMPS) combined with a novel Distribution of Relaxation Times (DRT) algorithm, revealed that CoPi enhances charge transfer by suppressing recombination and facilitating the transfer of photogenerated holes to TEMPO.

In the second case study, nickel-modified Ti:Fe_2O_3 photoanodes were used to directly oxidise HMF, eliminating the need for the expensive and not-sustainable TEMPO mediator. Operando X-ray absorption spectroscopy (XAS) showed that the presence of Ni-based electrocatalysts enhances the hole scavenging by HMF, reducing competition from water oxidation and streamlining the oxidation process. However, due to the highly alkaline conditions required to activate the Ni-based catalyst, issues such as low conversion efficiency and compound instability arose. Future optimization of conditions like temperature, substrate concentration, and base concentration could improve FDCA yields in this system.

The final case study focused on glycerol oxidation using a $BiVO_4$ photoanode. Glycerol is an efficient hole scavenger for $BiVO_4$, and previous studies have demonstrated high selectivity for dihydroxyacetone (DHA) as a valuable oxidation product at pH 2. This study aimed to enhance the long-term stability of the photoanode by implementing a modulated-current operational approach, which effectively stabilized the photoelectrochemical response, preserved the photoanode morphology, and significantly reduced photo-corrosion, improving the competitiveness of the process over current techniques used for GOR.

Bibliography

[1] V. Balzani, G. Bergamini, P. Ceroni, *Rend. Lincei* **2017**, *28*, 125–142.

[2] K. Fujishima, A., and Honda, *Nature* **1972**, *238*, 37–38.

[3] D. K. Dogutan, D. G. Nocera, *Acc. Chem. Res.* **2019**, 3143–3148.

[4] Y. Goto, T. Hisatomi, Q. Wang, T. Higashi, K. Ishikiriyama, T. Maeda, Y. Sakata, S. Okunaka, H. Tokudome, M. Katayama, S. Akiyama, H. Nishiyama, Y. Inoue, T. Takewaki, T. Setoyama, T. Minegishi, T. Takata, T. Yamada, K. Domen, *Joule* **2018**, *2*, 509–520.

[5] X. Guan, F. A. Chowdhury, N. Pant, L. Guo, L. Vayssieres, Z. Mi, *J. Phys. Chem. C* **2018**, *122*, 13797–13802.

[6] T. Hisatomi, K. Domen, *Nat. Catal.* **2019**, *2*, 387–399.

[7] J. Jia, L. C. Seitz, J. D. Benck, Y. Huo, Y. Chen, J. W. D. Ng, T. Bilir, J. S. Harris, T. F. Jaramillo, *Nat. Commun.* **2016**, *7*, 1–6.

[8] S. Hu, C. Xiang, S. Haussener, A. D. Berger, N. S. Lewis, *Energy Environ. Sci.* **2013**, *6*, 2984–2993.

[9] S. Zhang, L. Shen, T. Ye, K. Kong, H. Ye, H. Ding, Y. Hu, J. Hua, *Energy and Fuels* **2020**, *34*, 5016–5023.

[10] H. Döscher, J. F. Geisz, T. G. Deutsch, J. A. Turner, *Energy Environ. Sci.* **2014**, *7*, 2951–2956.

[11] Z. Wang, C. Li, K. Domen, *Chem. Soc. Rev.* **2019**, *48*, 2109–2125.

[12] K. T. Fountaine, H. J. Lewerenz, H. A. Atwater, *Nat. Commun.* **2016**, *7*, 1–9.

[13] G. E. Eperon, G. E. Eperon, T. Leijtens, K. A. Bush, R. Prasanna, T. Green, J. T. Wang, D. P. Mcmeekin, G. Volonakis, R. L. Milot, R. May, A. Palmstrom, J. Daniel, R. A. Belisle, J. B. Patel, E. S. Parrott, R. J. Sutton, W. Ma, B. Conings, A. Babayigit, H. Boyen, S. Bent, F. Giustino, M. Herz, M. B. Johnston, M. D. Mcgehee, H. J. Snaith, *Science (80-.).* **2016**, *9717*, 1–10.

[14] R. va de Krol, M. Grätzel, *Photoelectro - Chemical Hydrogen Production*, **2012**.

[15] C. R. Lhermitte, K. Sivula, *ACS Catal.* **2019**, *9*, 2007–2017.

[16] Y. Choi, R. Mehrotra, S. H. Lee, T. V. T. Nguyen, I. Lee, J. Kim, H. Y. Yang, H. Oh, H. Kim, J. W. Lee, Y. H. Kim, S. Y. Jang, J. W. Jang, J. Ryu, *Nat. Commun.* **2022**, *13*, DOI 10.1038/s41467-022-33435-1.

[17] R. Mazzaro, S. Boscolo Bibi, M. Natali, G. Bergamini, V. Morandi, P. Ceroni, A. Vomiero, *Nano Energy* **2019**, *61*, 36–46.

[18] W. Tang, L. Zhang, T. Qiu, H. Tan, Y. Wang, W. Liu, Y. Li, *Angew. Chemie Int. Ed.* **2023**, *62*, 1–8.

[19] S. Bhattacharjee, V. Andrei, C. Pornrungroj, M. Rahaman, C. M. Pichler, E. Reisner, *Adv. Funct. Mater.* **2022**, *32*, 2109313.

[20] H. Zhou, Y. Ren, Z. Li, M. Xu, Y. Wang, R. Ge, X. Kong, L. Zheng, H. Duan, *Nat. Commun.* **2021**, *12*, 1–9.

[21] T. Uekert, H. Kasap, E. Reisner, *J. Am. Chem. Soc.* **2019**, *141*, 15201–15210.

[22] T. Uekert, M. F. Kuehnel, D. W. Wakerley, E. Reisner, *Energy Environ. Sci.* **2018**, *11*, 2853–2857.

[23] H. Luo, J. Barrio, N. Sunny, A. Li, L. Steier, N. Shah, I. E. L. Stephens, M. Titirici, *Adv. Energy Mater.* **2021**, *11*, 2101180.

[24] J. A. Lin, I. Roh, P. Yang, *J. Am. Chem. Soc.* **2023**, *145*, 12987–12991.

[25] L. Fan, B. Liu, X. Liu, N. Senthilkumar, G. Wang, Z. Wen, *Energy Technol.* **2021**, *9*, 2000804.

[26] X. Yue, Y. Queneau, *ChemSusChem* **2022**, *15*, 1–13.

[27] M. G. Davidson, S. Elgie, S. Parsons, T. J. Young, *Green Chem.* **2021**, *23*, 3154–3171.

[28] A. Marshall, B. Jiang, R. M. Gauvin, C. M. Thomas, *Molecules* **2022**, *27*, 4071.

[29] Robert F. Pierret and Gerold W. Neudeck, *Intensity Modulated Photocurrent Spectroscopy of N-GaAs.*, **1987**.

[30] R. Van De Krol, Y. Liang, J. Schoonman, *J. Mater. Chem.* **2008**, *18*, 2311–2320.

[31] H. Gerischer, *Surf. Sci.* **1969**, *18*, 97–122.

[32] R. A. Marcus, *J. Chem. Phys.* **1956**, *24*, 966–978.

[33] R. a Marcus, *Annu. Rev. Phys. Chem.* **1964**, *15*, 155.

[34] T. Gatti, F. Lamberti, R. Mazzaro, I. Kriegel, D. Schlettwein, F. Enrichi, N. Lago, E. Di Maria, G. Meneghesso, A. Vomiero, S. Gross, *Adv. Energy Mater.* **2021**, *11*, 2101041.

[35] H. He, *Metal Oxide Semiconductors and Conductors*, Elsevier Inc., **2020**.

[36] Y. Yang, S. Wan, S. Li, R. Wang, M. Ou, B. Liu, Q. Zhong, *J. Mater. Chem. A* **2023**, *11*, 1756–1765.

[37] Q. Meng, B. Zhang, L. Fan, H. Liu, M. Valvo, K. Edström, M. Cuartero, R. de Marco, G. A. Crespo, L. Sun, *Angew. Chemie Int. Ed.* **2019**, *58*, 19027–19033.

[38] K. H. Ye, H. Li, D. Huang, S. Xiao, W. Qiu, M. Li, Y. Hu, W. Mai, H. Ji, S. Yang, *Nat. Commun.* **2019**, *10*, 1–9.

[39] S. J. Hong, S. Lee, J. S. Jang, J. S. Lee, *Energy Environ. Sci.* **2011**, *4*, 1781.

[40] T. M. and N. I. Wendusu, Taihei Honda, *RSC Adv.* **2013**, *3*, 24941–24945.

[41] A. Kudo, K. Omori, H. Kato, *J. Am. Chem. Soc.* **1999**, *121*, 11459–11467.

[42] S. Tokunaga, H. Kato, A. Kudo, *Chem. Mater.* **2001**, *13*, 4624–4628.

[43] A. Kudo, K. Ueda, H. Kato, I. Mikami, *Catal. Lettes* **1998**, *53*, 229–230.

[44] I. Grigioni, K. G. Stamplecoskie, E. Selli, P. V. Kamat, *J. Phys. Chem. C* **2015**, *119*, 20792–20800.

[45] I. Grigioni, K. G. Stamplecoskie, D. H. Jara, M. V. Dozzi, A. Oriana, G. Cerullo, P. V. Kamat, E. Selli, *ACS Energy Lett.* **2017**, *2,* 1362–1367.

[46] I. Grigioni, L. Ganzer, F. V. A. Camargo, B. Bozzini, G. Cerullo, E. Selli, *ACS Energy Lett.* **2019**, *4*, 2213–2219.

[47] P. Chatchai, Y. Murakami, S. ya Kishioka, A. Y. Nosaka, Y. Nosaka, *Electrochim. Acta* **2009**, *54*, 1147–1152.

[48] S. Grau, S. Berardi, A. Moya, R. Matheu, V. Cristino, J. J. Vilatela, C. A. Bignozzi, S. Caramori, C. Gimbert-Suriñach, A. Llobet, *Sustain. Energy Fuels* **2018**, *2,* 1979–1985.

[49] P. M. Rao, L. Cai, C. Liu, I. S. Cho, C. H. Lee, J. M. Weisse, P. Yang, X. Zheng, *Nano Lett.* **2014**, *14,* 1099–1105.

[50] X. Shi, I. Herraiz-Cardona, L. Bertoluzzi, P. Lopez-Varo, J. Bisquert, J. H. Park, S. Gimenez, *Phys. Chem. Chem. Phys.* **2016**, *18,* 9255–9261.

[51] S. R. Sitaaraman, A. N. Grace, J. Zhu, R. Sellappan, *Nanoscale Adv.* **2024**, *6*, 2407–2418.

[52] T. W. Kim, K.-S. Choi, *Science (80-.).* **2014**, *343*, 990–994.

[53] S. Wang, G. Liu, L. Wang, *Chem. Rev.* **2019**, *119*, 5192–5247.

[54] J. Lee, H. Yoon, K. S. Choi, S. Kim, S. Seo, J. Song, B. Choi, J. Ryu, S. Ryu, J. Oh, C. Jeon, S. Lee, *Small* **2020**, *16*, 1–11.

[55] H. S. Han, S. Shin, D. H. Kim, I. J. Park, J. S. Kim, P. Huang, J. Lee, I. S. Cho, X. Zheng, *Energy Environ. Sci.* **2018**, *11*, 1299–1306.

[56] P. Li, X. Chen, H. He, X. Zhou, Y. Zhou, Z. Zou, *Adv. Mater.* **2018**, *30*, 4–8.

[57] S. Wang, X. Wang, B. Liu, Z. Guo, K. (Ken) Ostrikov, L. Wang, W. Huang, *Nanoscale* **2021**, *13*, 17989–18009.

[58] R. Gao, L. Wang, *Angew. Chemie Int. Ed.* **2020**, *59*, 23094–23099.

[59] F. M. Toma, J. K. Cooper, V. Kunzelmann, M. T. McDowell, J. Yu, D. M. Larson, N. J. Borys, C. Abelyan, J. W. Beeman, K. M. Yu, J. Yang, L. Chen, M. R. Shaner, J. Spurgeon, F. A. Houle, K. A. Persson, I. D. Sharp, *Nat. Commun.* **2016**, *7,* 12012.

[60] R. T. Gao, D. He, L. Wu, K. Hu, X. Liu, Y. Su, L. Wang, *Angew. Chemie - Int. Ed.* **2020**, *59,* 6213–6218.

[61] X. Hu, Y. Li, X. Wei, L. Wang, H. She, J. Huang, Q. Wang, *Adv. Powder Mater.* **2022**, *1*, 100024.

[62] R. Gao, D. Yan, *Adv. Energy Mater.* **2020**, *10,* 1–19.

[63] Y. Kuang, Q. Jia, H. Nishiyama, T. Yamada, A. Kudo, K. Domen, *Adv. Energy Mater.* **2016**,

6, 2–8.

[64] D. Wang, R. Li, J. Zhu, J. Shi, J. Han, X. Zong, C. Li, *J. Phys. Chem. C* **2012**, *116*, 5082–5089.

[65] J. H. Kim, Y. Jo, J. H. Kim, J. W. Jang, H. J. Kang, Y. H. Lee, D. S. Kim, Y. Jun, J. S. Lee, *ACS Nano* **2015**, *9*, 11820–11829.

[66] Y. Kuang, Q. Jia, G. Ma, T. Hisatomi, T. Minegishi, H. Nishiyama, M. Nakabayashi, N. Shibata, T. Yamada, A. Kudo, K. Domen, *Nat. Energy* **2016**, *2*, 16191.

[67] Y. Piekner, D. S. Ellis, D. A. Grave, A. Tsyganok, A. Rothschild, *Energy Environ. Sci.* **2021**, *14*, 4584–4598.

[68] J. Li, D. Chu, *Energy Band Engineering of Metal Oxide for Enhanced Visible Light Absorption*, Elsevier Ltd., **2018**.

[69] S. Berardi, J. Kopula Kesavan, L. Amidani, E. M. Meloni, M. Marelli, F. Boscherini, S. Caramori, L. Pasquini, *ACS Appl. Mater. Interfaces* **2020**, *12*, 47435–47446.

[70] S. Lima, M. M. Antunes, M. Pillinger, A. A. Valente, *ChemCatChem* **2011**, *3*, 1686–1706.

[71] M. E. Zakrzewska, E. Bogel-Lukasik, R. Bogel-Lukasik, *ChemInform* **2011**, *42*, 397–417.

[72] N. Mosier, C. Wyman, B. Dale, R. Elander, Y. Y. Lee, M. Holtzapple, M. Ladisch, *Bioresour. Technol.* **2005**, *96*, 673–686.

[73] R. H. Y. Chang, J. Jang, K. C. W. Wu, *Green Chem.* **2011**, *13*, 2844–2850.

[74] R. Rinaldi, F. Schüth, *ChemSusChem* **2009**, *2*, 1096–1107.

[75] D. M. Alonso, S. G. Wettstein, M. A. Mellmer, E. I. Gurbuz, J. A. Dumesic, *Energy Environ. Sci.* **2013**, *6*, 76–80.

[76] S. Jia, X. He, Z. Xu, *RSC Adv.* **2017**, *7*, 39221–39227.

[77] J. P. Lange, E. Van Der Heide, J. Van Buijtenen, R. Price, *ChemSusChem* **2012**, *5*, 150–166.

[78] A. S. Mamman, J. M. Lee, Y. C. Kim, I. T. Hwang, N. J. Park, Y. K. Hwang, J. S. Chang, J. S. Hwang, *Biofuels, Bioprod. Biorefining* **2008**, *2*, 438–454.

[79] J. Zakzeski, P. C. A. Bruijnincx, A. L. Jongerius, B. M. Weckhuysen, *Chem. Rev.* **2010**, *110*, 3552–3599.

[80] A. Corma Canos, S. Iborra, A. Velty, *Chem. Rev.* **2007**, *107*, 2411–2502.

[81] M. Ko, L. T. M. Pham, Y. J. Sa, J. Woo, T. V. T. Nguyen, J. H. Kim, D. Oh, P. Sharma, J. Ryu, T. J. Shin, S. H. Joo, Y. H. Kim, J. W. Jang, *Nat. Commun.* **2019**, *10*, 1–10.

[82] A. T. Wasie, M. G. Tadesse, A. S. Wotango, R. K. Bachheti, I. N. Ahmed, *Discov. Appl. Sci.* **2024**, *6*, 37.

[83] T. Wang, M. W. Nolte, B. H. Shanks, *Green Chem.* **2014**, *16*, 548–572.

[84] A. P. Thallada Bhaskar, *Recent Advances in Thermochemical Conversion of Biomass*, Elsevier, **2015**.

[85] J. Esteban, M. Ladero, *Int. J. Food Sci. Technol.* **2018**, *53*, 1095–1108.

[86] A. Rezayan, Y. Zhang, B. Li, C. C. Xu, *ChemCatChem* **2023**, *15*, 1–25.

[87] F. Menegazzo, E. Ghedini, M. Signoretto, *Molecules* **2018**, *23*, 1–18.

[88] D. M. Sajid, *Acad. Lett.* **2022**, 1–13.

[89] G. Totaro, L. Sisti, P. Marchese, M. Colonna, A. Romano, C. Gioia, M. Vannini, A. Celli, *ChemSusChem* **2022**, *15*, 1–13.

[90] F. Yang, J. Liu, B. Li, H. Li, Z. Jiang, *Biotechnol. Biofuels Bioprod.* **2023**, *16*, 1–13.

[91] R. O. Rajesh, T. K. Godan, A. K. Rai, D. Sahoo, A. Pandey, P. Binod, *Bioresour. Technol.* **2022**, *351*, 126995.

[92] Z. Ma, L. Wang, G. Li, T. Song, *Catalysts* **2024**, *14*, 157.

[93] X. H. Chadderdon, D. J. Chadderdon, T. Pfennig, B. H. Shanks, W. Li, *Green Chem.* **2019**, *21*, 6210–6219.

[94] Y. Yang, T. Mu, *Green Chem.* **2021**, *23*, 4228–4254.

[95] H. G. Cha, K. S. Choi, *Nat. Chem.* **2015**, *7*, 328–333.

[96] D. J. Chadderdon, L. P. Wu, Z. A. McGraw, M. Panthani, W. Li, *ChemElectroChem* **2019**, *6*, 3387–3392.

[97] A. Kawde, M. Sayed, Q. Shi, J. Uhlig, T. Pullerits, R. Hatti-Kaul, *Catalysts* **2021**, *11*, 1–12.

[98] K. R. Vuyyuru, P. Strasser, *Catal. Today* **2012**, *195*, 144–154.

[99] H. A. Beejapur, Q. Zhang, K. Hu, L. Zhu, J. Wang, Z. Ye, *ACS Catal.* **2019**, *9*, 2777–2830.

[100] C. R. Lhermitte, N. Plainpan, P. Canjura, F. Boudoire, K. Sivula, *RSC Adv.* **2020**, *11*, 198–202.

[101] L. Özcan, P. Yalçın, O. Alagöz, S. Yurdakal, *Catal. Today* **2017**, *281*, 205–213.

[102] P. Galletti, M. Pori, F. Funiciello, R. Soldati, A. Ballardini, D. Giacomini, *ChemSusChem* **2014**, *7*, 2684–2689.

[103] M. L. Krebs, A. Bodach, C. Wang, F. Schüth, *Green Chem.* **2023**, *25*, 1797–1802.

[104] G. Fu, X. Kang, Y. Zhang, Y. Guo, Z. Li, J. Liu, L. Wang, J. Zhang, X.-Z. Fu, J.-L. Luo, *Nat. Commun.* **2023**, *14*, 8395.

[105] U. S. D. of E. (DOE), “Biodiesel Production and Distribution,” can be found under https://afdc.energy.gov/fuels/biodiesel-production, **n.d.**

[106] L. Bournay, D. Casanave, B. Delfort, G. Hillion, J. A. Chodorge, *Catal. Today* **2005**, *106*, 190–192.

[107] F. Omota, A. C. Dimian, A. Bliek, *Chem. Eng. Sci.* **2003**, *58*, 3159–3174.

[108] F. Omota, A. C. Dimian, A. Bliek, *Chem. Eng. Sci.* **2003**, *58*, 3175–3185.

[109] Y. Liu, B. Zhang, D. Yan, X. Xiang, *Green Chem.* **2024**, *26*, 2505–2524.

[110] G. Zhao, G. Wu, Y. Liu, Y. He, J. Feng, D. Li, *Catal. Sci. Technol.* **2020**, *10*, 6223–6234.

[111] J. Turner, D. A. O'Loughlin, P. Green, T. O. McDonald, K. J. Hamill, *J. Cosmet. Dermatol.* **2023**, *22*, 79–88.

[112] L. Bricotte, K. Chougrani, V. Alard, V. Ladmiral, S. Caillol, *Molecules* **2023**, *28*, 2724.

[113] T. Li, D. A. Harrington, *ChemSusChem* **2021**, *14*, 1472–1495.

[114] D. Liu, J.-C. Liu, W. Cai, J. Ma, H. Bin Yang, H. Xiao, J. Li, Y. Xiong, Y. Huang, B. Liu, *Nat. Commun.* **2019**, *10*, 1779.

[115] C. Lin, C. Dong, S. Kim, Y. Lu, Y. Wang, Z. Yu, Y. Gu, Z. Gu, D. K. Lee, K. Zhang, J. H. Park, *Adv. Mater.* **2023**, *35*, 2209955.

[116] Y. Xiao, M. Wang, D. Liu, J. Gao, J. Ding, H. Wang, H. Bin Yang, F. Li, M. Chen, Y. Xu, D. Xu, Y. Zhang, S. Fang, X. Ao, J. Wang, C. Su, B. Liu, *Angew. Chem. Int. Ed. Engl.* **2024**, *63*, 1–7.

[117] D. K. Bora, M. Nadjafi, *Energy Adv.* **2022**, *1*, 715–728.

[118] M. Molera, M. Sarret, C. Fàbrega, T. Andreu, *J. Electrochem. Soc.* **2024**, *171*, 086503.

[119] Y. Lu, B. G. Lee, C. Lin, T.-K. Liu, Z. Wang, J. Miao, S. H. Oh, K. C. Kim, K. Zhang, J. H. Park, *Nat. Commun.* **2024**, *15*, 5475.

[120] A. C. Lazanas, M. I. Prodromidis, *ACS Meas. Sci. Au* **2023**, *3*, 162–193.

[121] E. A. Ponomarev, L. M. Peter, *J. Electroanal. Chem.* **1995**, *396*, 219–226.

[122] L. M. Peter, *Chem. Rev.* **1990**, *90*, 753–769.

[123] L. M. Peter, *J. Solid State Electrochem.* **2013**, *17*, 315–326.

[124] D. Klotz, D. A. Grave, H. Dotan, A. Rothschild, *J. Phys. Chem. Lett.* **2018**, *9*, 1466–1472.

[125] I. Rodriguez-Gutierrez, J. B. Souza Junior, E. R. Leite, L. Vayssieres, F. L. Souza, *Appl. Phys. Lett.* **2021**, *119*, 071602.

[126] I. Rodríguez-Gutiérrez, E. Djatoubai, J. Su, A. Vega-Poot, G. Rodríguez-Gattorno, F. L. Souza, G. Oskam, *Sol. Energy Mater. Sol. Cells* **2020**, *208*, 110378.

[127] A. Piccioni, P. Vecchi, L. Vecchi, S. Grandi, S. Caramori, R. Mazzaro, L. Pasquini, *J. Phys. Chem. C* **2023**, *127*, 7957–7964.

[128] W. W. Gärtner, *Phys. Rev.* **1959**, *116*, 84–87.

[129] F. E. Bedoya-Lora, M. E. Valencia-García, A. Hankin, D. Klotz, J. A. Calderón, *Electrochim. Acta* **2022**, *402*, 139559.

[130] T Jo, *X-Ray Absorption Spectroscopy*, **2005**.

[131] A. Minguzzi, O. Lugaresi, C. Locatelli, S. Rondinini, F. D'Acapito, E. Achilli, P. Ghigna, *Anal. Chem.* **2013**, *85*, 7009–7013.

[132] F. Allegretti, *Electron Spectrosc. Surfaces* **2011**, 1–22.

[133] M. Montalti, A. Credi, L. Prodi, M. T. Gandolfi, *Handbook of Photochemistry*, CRC Press, **2006**.

[134] H. Kong, S. Gupta, A. F. Pérez-Torres, C. Höhn, P. Bogdanoff, M. T. Mayer, R. van de Krol, M. Favaro, F. F. Abdi, *Chem. Sci.* **2024**, *15*, 10425–10435.

[135] J. Deng, J. Zhong, A. Pu, D. Zhang, M. Li, X. Sun, S.-T. Lee, *J. Appl. Phys.* **2012**, *112*, 084312.

[136] D. K. Bora, *Mater. Sci. Semicond. Process.* **2015**, *31*, 728–738.

[137] Y. Ling, G. Wang, D. A. Wheeler, J. Z. Zhang, Y. Li, *Nano Lett.* **2011**, *11*, 2119–2125.

[138] M. W. Kanan, D. G. Nocera, *Science* **2008**, *321*, 1072–1075.

[139] L. Liardet, J. E. Katz, J. Luo, M. Grätzel, X. Hu, *J. Mater. Chem. A* **2019**, *7*, 6012–6020.

[140] M. T. Bender, K. Choi, *ChemSusChem* **2022**, *15*, 1–14.

[141] J. Zhang, R. Garcí A-Rodrí Guez, P. Cameron, S. Eslava, *2972 | Energy Environ. Sci* **2018**, *11*, 2972.

[142] D. K. Zhong, D. R. Gamelin, *J. Am. Chem. Soc.* **2010**, *132*, 4202–4207.

[143] C. C. L. McCrory, S. Jung, J. C. Peters, T. F. Jaramillo, *J. Am. Chem. Soc.* **2013**, *135*, 16977–16987.

[144] R. Mazzaro, S. Boscolo Bibi, M. Natali, G. Bergamini, V. Morandi, P. Ceroni, A. Vomiero, *Nano Energy* **2019**, *61*, 36–46.

[145] M. R. Nellist, F. A. L. Laskowski, J. Qiu, H. Hajibabaei, K. Sivula, T. W. Hamann, S. W. Boettcher, *Nat. Energy* **2018**, *3*, 46–52.

[146] B. Klahr, S. Gimenez, F. Fabregat-Santiago, J. Bisquert, T. W. Hamann, *Energy Environ. Sci.* **2012**, *5*, 7626–7636.

[147] L. M. Peter, K. G. U. Wijayantha, A. A. Tahir, *Faraday Discuss.* **2012**, *155*, 309–322.

[148] P. Dias, L. Andrade, A. Mendes, *Nano Energy* **2017**, *38*, 218–231.

[149] Y. Yang, T. Mu, *Green Chem.* **2021**, *23*, 4228–4254.

[150] X. Jiang, W. Li, Y. Liu, L. Zhao, Z. Chen, L. Zhang, Y. Zhang, S. Yun, *SusMat* **2023**, *3*, 21–43.

[151] EC, *Critical Raw Materials Resilience: Charting a Path towards Greater Security and Sustainability*, **2020**.

[152] M. Fleischmann, K. Korinek, D. Pletcher, *J. Electroanal. Chem. Interfacial Electrochem.* **1971**, *31*, 39–49.

[153] M. Fleischmann, K. Korinek, D. Pletcher, *J. Chem. Soc. Perkin Trans. 2* **1972**, *2*, 1396.

[154] R. N. Dürr, P. Maltoni, H. Tian, B. Jousselme, L. Hammarström, T. Edvinsson, *ACS Nano* **2021**, *15*, 13504–13515.

[155] L. Peng, J. Min, A. Bendavid, D. Chu, X. Lu, R. Amal, Z. Han, *ACS Appl. Mater. Interfaces*

2022, *14*, 40822–40833.

[156] M. Luo, J. Yang, X. Li, M. Eguchi, Y. Yamauchi, Z. L. Wang, *Chem. Sci.* **2023**, *14*, 3400–3414.

[157] J. A. Bau, H. Haspel, S. Ould-Chikh, A. Aguilar-Tapia, J. L. Hazemann, H. Idriss, K. Takanabe, *J. Mater. Chem. A* **2019**, *7*, 15031–15035.

[158] R. D. L. Smith, C. Pasquini, S. Loos, P. Chernev, K. Klingan, P. Kubella, M. R. Mohammadi, D. Gonzalez-Flores, H. Dau, *Nat. Commun.* **2017**, *8*, 2022.

[159] D. González-Flores, K. Klingan, P. Chernev, S. Loos, M. R. Mohammadi, C. Pasquini, P. Kubella, I. Zaharieva, R. D. L. Smith, H. Dau, *Sustain. Energy Fuels* **2018**, *2*, 1986–1994.

[160] D. K. Bora, M. Nadjafi, A. Armutlulu, D. Hosseini, P. Castro-Fernández, R. Toth, *Energy Adv.* **2022**, *1*, 715–728.

Acknowledgements

This PhD research activity was supported by H2020 project CONDOR: COmbined suN-Driven Oxidation and CO2 Reduction for Renewable Energy Storage. I would like to express my gratitude to my supervisors and co-supervisors for their invaluable guidance and support, which played a pivotal role in the successful completion of this work. I also wish to extend my sincere thanks to the N-REX research group (Nanomaterials for Renewable Energy Conversion and Storage) at the Department of Physics and Astronomy "Augusto Righi," University of Bologna, for their generosity in providing laboratory access, instruments, scientific knowledge, consultation, and assistance with both conceptual development and scientific writing.

Additionally, I would like to thank Professor Stefano Caramori (University of Ferrara, Italy) for supplying the Ti-doped hematite photoanodes and conducting the EIS measurements, as well as Professor Paola Ceroni (University of Bologna, Italy) for her contributions to the spectro-photometric and HPLC analyses. My gratitude also extends to Prof. Dr. Roel van de Krol (Institute for Solar Fuels, Helmholtz Zentrum Berlin, Germany) and Dr. Marco Favaro for their mentorship during my time abroad and for their enthusiastic support of my research.